ELECTRONIC INTERPRETATIONS OF NOBLE AND NON-NOBLE METAL BASED ELECTROCATALYSTS

WONG HON HO

PhD

The Hong Kong Polytechnic University

2025

The Hong Kong Polytechnic University

Department of Applied Biology and Chemical Technology

Electronic Interpretations of Noble and Non-Noble Metal based Electrocatalysts

WONG Hon Ho

A thesis submitted in partial fulfilment of the requirements
for the degree of Doctor of Philosophy

Aug 2025

Certificate of Originality

I hereby declare that this thesis is my own work and that, to the best of my knowledge and belief, it reproduces no material previously published or written, nor material that has been accepted for the award of any other degree or diploma, except where due acknowledgement has been made in the text.

__________________________(Signed)

WONG Hon Ho____________(Name of student)

Abstract

As energy demand and climate change grow, there is an essential need for sustainable energy solutions. Electrocatalysis has demonstrated an irreplaceable role in sustainable development by enabling efficient energy conversion and storage. In particular, the electrocatalytic recycling of CO_2 using renewable energy sources has provided an ideal approach for reducing the carbon footprint. Based on this, hydrocarbons and other energy-rich fuels can be produced via CO_2 reduction reaction (CO_2RR), which converts CO_2 into different value-added chemicals. Researchers have focused on designing and developing electrocatalytic materials and reaction systems for the efficient CO_2RR. Atomic catalysts (ACs) are considered to be a novel, efficient catalyst with excellent efficiency in atom utilisation, as well as unique electronic structures, which enable ACs to display remarkable activity and selectivity toward various catalysis reactions. To stabilize isolated atoms on ACs, specific materials, including porous materials, have been commonly employed as the support of ACs. For example, carbon materials such as Graphdiyne (GDY) have been reported to be a promising support for constructing ACs for electrocatalysis. Moreover, the neighbouring interaction on ACs also demonstrated a special role in the CO_2RR process. Also, the electronic structure of the active metal centre can be modified via neighbouring effects; in particular, neighbouring sites can serve as a second assisted site that participates in the electrocatalysis.

A significant challenge in electrochemical CO_2RR is achieving high selectivity toward multi-carbon products, which is attributed to the sluggish carbon–carbon bond

formation on the C_{2+} pathways. Among all electrocatalytic materials, the copper-based electrocatalysts have been widely used in multi-carbon products in electrochemical CO_2RR. In general, dimerization of two adsorbed *CO intermediates is the critical step on multi-carbon pathways. In particular, alkali metal cations (AM^+) play a crucial role in the C–C coupling process. Existing research has shown that cation species can facilitate C–C bond formation between intermediates via an electric field and the local pH at the electrode-electrolyte interface. In addition, the intrinsic effects of cations have rarely been discussed. Based on this, we employed density functional theory (DFT) calculations to investigate the direct cation effect on CO dimerization on Cu and Pt surfaces. The DFT calculation revealed that the *OCCO intermediate formation can be promoted by the AM^+ on Cu and Pt surfaces due to the stabilization effects induced by direct cation coordination. Moreover, we have revealed the strong linear correlation between the reaction energy of *OCCO formation and cation–dimer stabilization. Further electronic investigations also revealed that the stabilization effects from cation-dimer coordination are related to improved charge transfer from the metal sites to the adsorbed intermediate, as well as the modifications of the electronic structure.

Recent studies also show that the water structure near the electrocatalyst surface can affect CO_2RR performance. For example, variations in cation size in the electrolytes significantly tune the hydrogen-bonding network. Besides, it is believed that solvation will influence cation stabilization. Based on this, MD and DFT were used to study the solvation properties of AM^+, and the radial distribution function (RDF) analysis revealed the coordination number (CN) of AM^+ in aqueous solution. Furthermore, the structure of the solvated cations was determined by DFT calculation with an implicit solvation model, in which the charge distribution analysis showed the trend of reactivity of the cation centre in the solvated ion.

Keywords: Noble Metal, Electrocatalyst, Carbon Dioxide Reduction Reaction, Cation Effect, Alkali Metal Cations, C–C coupling, Stabilization Effect, Density Functional Theory

Acknowledgements

First and foremost, I would like to express my sincere gratitude to my supervisor, Prof. Bolong Huang (Years 1-4, Semester 1), for providing me with invaluable guidance, encouragement, and expertise throughout my research journey. He has been a beacon of wisdom and support, steering me through the complexities of my academic endeavors with remarkable patience and insight. Although my performance did not always meet expectations, Prof. Huang still allowed me to grow, learn, and contribute under his guidance. Without his patient guidance, I would be unable to complete my dissertation. I would also like to express my sincere gratitude to my current supervisor, Prof. Wing-yiu Yu, for his tremendous support and encouragement. It is my fortune to have the opportunity to work with both of them.

In addition, I would like to thank my research groupmates, whose invaluable assistance, thoughtful advice, and collaborative spirit have enriched my journey beyond measure. In particular, a special note of appreciation goes to our senior group member, Dr. Mingzi Sun, whose dedication and expertise have left an indelible mark on my work. Dr. Sun generously carved out time from her busy schedule to offer constructive suggestions and meticulous feedback while I wrote my research paper.

Additionally, I am deeply thankful for the ongoing support and assistance of the Department of Applied Biology and Chemical Technology. I am also profoundly grateful to my friends for their enduring support. Those irreplaceable memories we have created together have become a cherished part of my life that continually motivates me

to strive for my dream and saves me from depression. Finally, yet importantly, I would like to express my gratitude to my family. My greatest fortune is having their unwavering love, encouragement, and support. Their constant belief in me has been a constant source of motivation to overcome the challenges in my life.

Table of Contents

List of Abbreviations

AC	Atomic catalyst
AM^+	Alkali metal cation
BFGS	Broyden–Fletcher–Goldfarb–Shanno
CO_2RR	Carbon dioxide reduction reaction
CN	Coordination number
COSMO	Conductor-like screening model
DFT	Density functional theory
DSPP	DFT Semi-core Pseudopods
DNP	Double numerical plus polarization
DOS	Density of state
E_F	Fermi level
FE	Faraday efficiency
GGA	Generalized gradient approximation
GDY	Graphdiyne
HER	Hydrogen evolution reaction
LDA	Local density approximation
HOMO	Highest occupied molecular orbital

LUMO	Lowest unoccupied molecular orbital
MD	Molecular dynamics
NM	Noble metal
NRR	Nitrogen reduction reaction
ORR	Oxygen reduction reaction
OER	Oxygen evolution reaction
OHP	Outer Helmholtz plane
PBE	Perdew, Burke, and Ernzerhof
PDOS	Partial density of states
RHE	Reversible hydrogen electrode
RDF	Radial distribution function
SAC	Single-atom catalyst
SHE	Standard hydrogen electrode
SCF	Self-consistent field
TM	Transition metal
TDOS	Total density of state

List of Figures

Chapter 1. Introduction

1.1 Catalysts for Energy Conversion

1.1.1 CO_2 Reduction Reaction

Modern human activities have been sustained by a relentless stream of energy generated primarily through the burning of fossil fuels. However, fossil fuels are non-renewable, and limited resources will eventually be depleted by 2060. Hence, there is an urgent need to search for alternative energy sources to replace fossil fuel resources. Additionally, technological breakthroughs and innovations are also reshaping industries and the energy landscape.

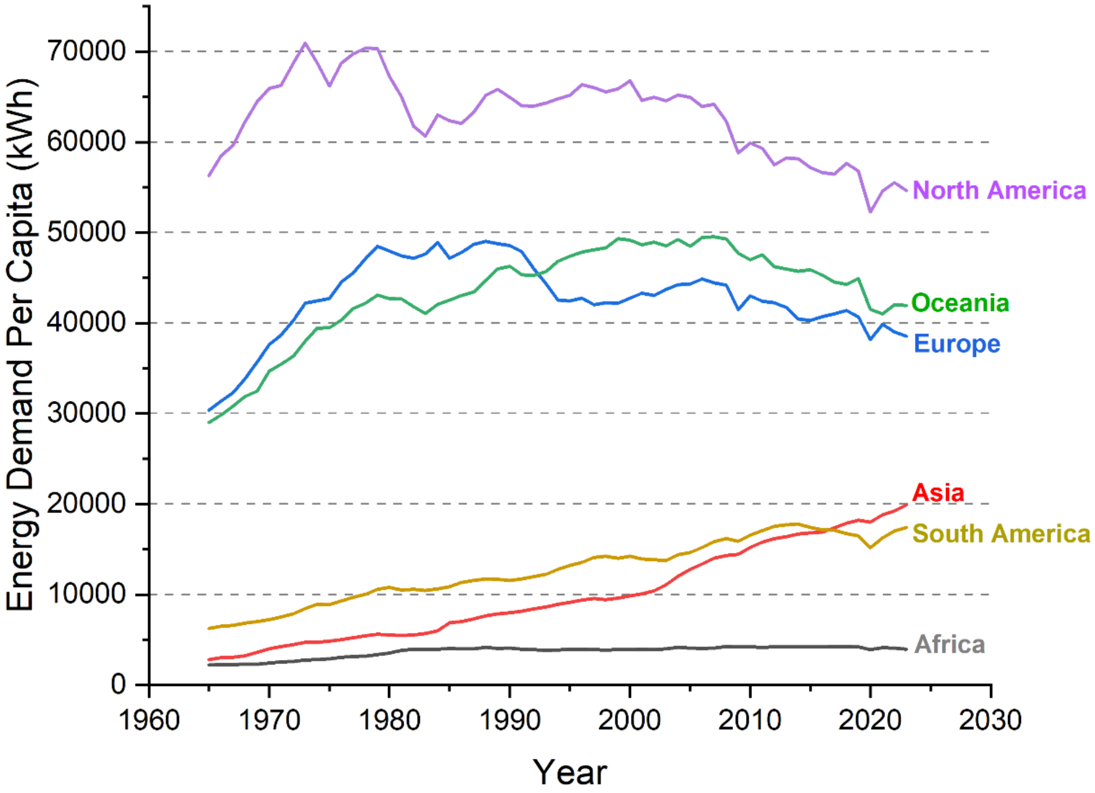

Figure 1.1.1 Energy consumption per capita (1965-2023) of the selected regions (Africa, the North/South Americas, Asia, Europe, and Oceania). Data adapted from U.S. Energy Information Administration (2023) and other sources.

The energy consumption per capita for high-development regions (North America, Oceania, and Europe) has generally decreased since 2000, primarily due to improved energy efficiency and the adoption of renewable energy sources (**Figure 1.1.1**). Notably, energy demand per person in Asia and South America has increased significantly in recent decades due to structural shifts in the global economy, driven by the relocation of energy-intensive industries, leading to higher demand in these regions (e.g. Southeast Asia and China).

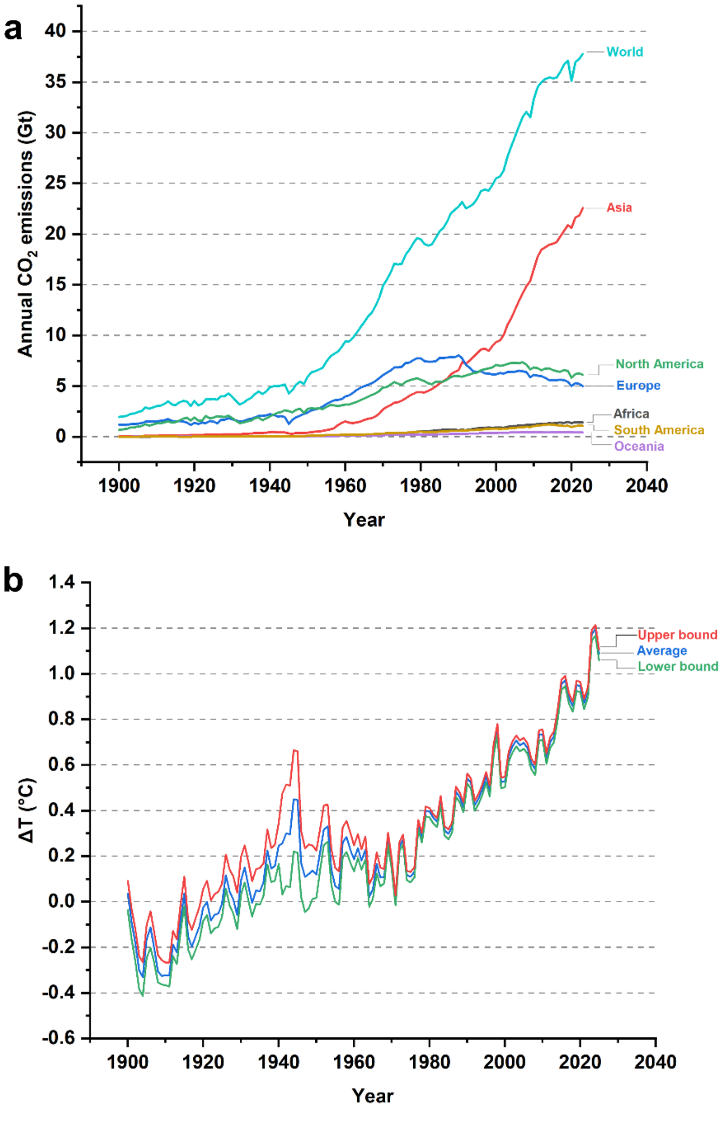

Figure 1.1.2 (a) Cumulative CO_2 emissions (in gigatons) produced from the burning of fossil fuels. Adapted from Global Carbon Budget (2024) (b) The difference of sea surface temperatures (in °C) compared to the mean from 1861-1890. Data adapted from Hadley Centre's Sea Surface Temperature (2025).

On the other hand, the reliance on fossil fuels also led to serious environmental concerns. Global carbon emissions have increased significantly since 1900. Over the past century, industrial activities have led to a significant increase in CO_2 emissions, with the majority of these emissions attributed to the combustion of fossil fuels.[1] In 2024, global CO_2 emissions associated with industrial activity exceeded 35 gigatons, contributing to record atmospheric CO_2 levels and surface temperature changes over the past half-century (**Figure 1.1.2**). Climate change associated with CO_2 emissions poses a significant threat to humanity and all other organisms on Earth. In order to alleviate carbon emissions and reduce our reliance on fossil fuels, the development of better energy conversion technologies that enable efficient utilization of fossil fuels and renewable energy sources has become the central focus in the energy field. Among all energy-related technologies, catalysis emerges as a key technology for addressing energy challenges. The catalyst can assist in chemical reactions by offering alternative reaction pathways with lower energy barriers. In contrast, the catalyst will not be consumed during the reaction process. Modern society heavily relies on catalysis, which is widely used in the production of polymers, pharmaceuticals, specialty chemicals, and fuels. Homogeneous catalysts exist in the same phase as the reactants, which contribute approximately 17%–30% of the total synthesis in industrial processes.[2] The homogeneous catalysts are primarily applied to synthesize complex organic compounds via (asymmetric) reactions.[3-4] Conversely, heterogeneous catalysts exist in a different phase, which is the core of the modern industries since it contributes about 80–90% of chemical synthesis due to its excellent recyclability and durability.[5] One of the significant applications of solid heterogeneous catalysis is driving electrochemical reactions, which including hydrogen evolution reaction (HER),[6-7] oxygen evolution reaction (OER),[8-9] oxygen reduction reaction (ORR),[10-11] nitrogen reduction reaction (NRR)[12-13] and carbon dioxide reduction reaction (CO_2RR).[14-15] Electrocatalysts catalyzed these key electrochemical reactions to generate alternative fuels and neutralize carbon. Moreover, all these reactions required advanced eletrocatalysts for practical applications.

Although the CO_2 emission can be reduced by using alternative clean renewable energy and nuclear energy, fossil fuels are still the dominant global energy generation, mainly due to the low reliability and relatively high costs of clean renewable energy, as well as the potential dangers associated with nuclear energy, which make it challenging to replace traditional fossil fuels. On the other hand, recycling the emitted CO_2 to produce useful substances will be a significant step toward tackling rising atmospheric CO_2 levels. The CO_2 has two equivalent C=O bonds with a bond length of 1.12 Å.[16-17] The C=O bonds has a high bonding energy of about 750 kJ mol^{-1}, which is much higher than C–C (~ 340 kJ mol^{-1}), C–O (~ 330 kJ mol^{-1}), and C–H (~ 410 kJ mol^{-1}), and hence the decomposition of CO_2 required high temperatures.[18] Although converting emitted CO_2 into valuable chemicals or fuels poses significant challenges, it has attracted considerable attention for its potential to address climate change and produce value-added products.

The CO_2RR can convert CO_2 into valuable products at an electrocatalyst surface. The CO_2RR process is a reverse fuel combustion process that offers a feasible approach to reducing greenhouse gas concentrations. The CO_2RR can convert the CO_2 into valuable hydrocarbons and alcohol, using electrical power. Additionally, the generation of renewable sources (e.g solar energy) varies over time, and the generation mismatches the energy demand. In this regard, the excess renewable electrical energy can be stored as fuels (chemical energy) via CO_2RR (**Figure 1.1.3a**). Hence, designing a more efficient CO_2RR electrocatalyst is key to such energy conversion. In addition, storing electrical energy as chemical fuels also has the benefit of being low-cost and easy to store and transport. The current research progress on CO_2RR involves investigating the CO_2 reduction mechanism on catalyst surfaces, as well as descriptors for activity and selectivity in CO_2 reduction over H_2 formation, and selectivity between C_1 and C_2 production. Various types of electrocatalysts, including bimetallic core-shell structure alloys, ionic compounds, and SACs, have been proposed for efficient CO_2RR electrocatalysis. In this chapter, the mechanism and the main challenges of CO_2RR will be introduced. We will also discuss cutting-edge design strategies for CO_2RR electrocatalysts.

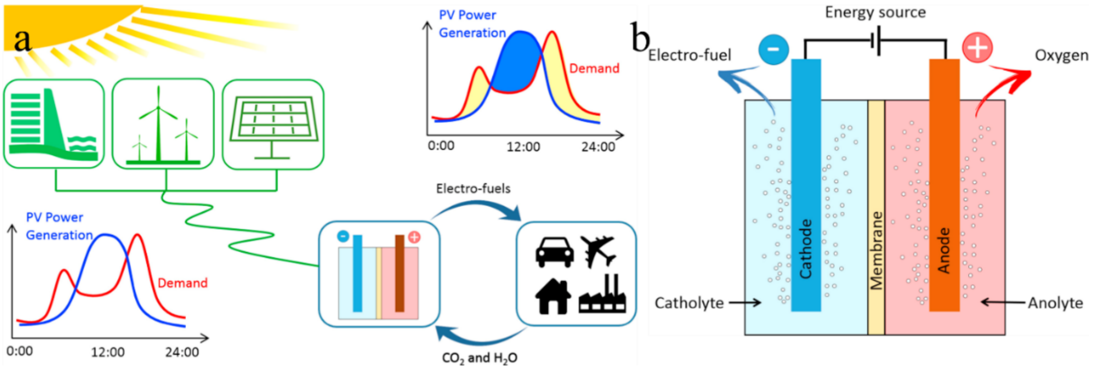

Figure 1.1.3 (a) Schematic diagram of alleviating the renewable energy generation and demand mismatch via electro-fuel conversion. (b) A typical CO_2 electrolyser for electrochemical CO_2RR.[19]

1.1.2 Challenges of CO_2 Reduction

As CO_2 cannot be further oxidized due to its high thermodynamic stability, transforming it into reduced hydrocarbons and alcohols is challenging because of the slow kinetics of CO_2RR. However, compared to the thermochemical[20] and photochemical[18] methods, which require high temperatures or suffer from light-harvesting issues (i.e., no suitable bandgap energy or structure to harvest solar light), the CO_2RR is the most feasible approach. Electrochemical CO_2RR can occur at ambient conditions with the reaction rate easily controlled by the applied potential. A typical CO_2 electrolyser is shown in **Figure 1.1.3b,** where the cathode and anode are separated by an ion-conducting membrane. The anodic reaction is an OER, in which water is oxidized to oxygen molecules. The CO_2RR is a cathodic reaction, and the overall CO_2RR is generally expressed as:

$$x\mathrm{CO_2} + n\mathrm{H^+}\ n\mathrm{e^-} \rightarrow \text{product} + y\mathrm{H_2O}$$

The reduction of CO_2 is a thermodynamically uphill process; therefore, an external bias is needed to drive the reaction. CO, HCOOH, HCHO, CH_3OH and CH_4 are the C_1 products, whereas C_2 products, including C_2H_4, CH_3CHO, C_2H_5OH and CH_3COOH, can be formed via CO_2RR, whereas the products with three or more C atoms are rarely reported. At present, however, the FE of CO_2RR is limited by the competing HER due to their similar reduction potential. The electrode potentials of CO_2 to various C_1 products and the HER reduction potential at pH = 7 are shown in **Table 1.1.1**.

Table 1.1.1 Standard reduction potentials of CO_2 in aqueous solutions (pH = 7.0, 1.0 M electrolyte) under standard conditions (1 atmosphere gas pressure, 25°C).

Half-Reactions	**Reduction potentials (V vs. SHE)**
$CO_2 + 2H^+ + 2e^- \rightarrow HCOOH$	–0.61
$CO_2 + 2H^+ + 2e^- \rightarrow CO + H_2O$	–0.53
$CO_2 + 4H^+ + 4e^- \rightarrow C + 2H_2O$	–0.20
$CO_2 + 4H^+ + 4e^- \rightarrow HCHO + H_2O$	–0.48
$CO_2 + 6H^+ + 8e^- \rightarrow CH_3OH + H_2O$	–0.38
$CO_2 + 8H^+ + 8e^- \rightarrow CH_4 + 2H_2O$	–0.24
$2H^+ + 2e^- \rightarrow H_2$	–0.42

Notably, the direct single-electron reduction of CO_2 required a thermodynamic potential of –1.90 V vs. SHE, making the reaction highly challenging. Therefore, a suitable CO_2RR electrocatalyst should be able to stabilize the radical intermediate and lead to a less negative reduction potential, in which this single electron-transfer activation commonly occurs in molecular electrocatalysis (e.g. cobalt-(proto) porphyrin catalyst), in which the $CO_2^{\cdot -}$ radical intermediate is formed in the metal centre.[21] In contrast, a more thermodynamically favorable pathway in solid-phase electrocatalysts is via proton-assisted electron transfer.[19]

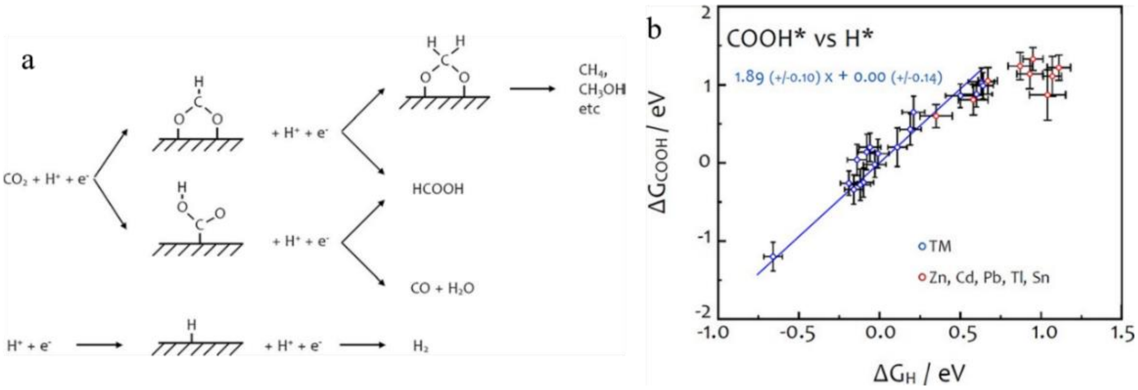

Figure. 1.1.4 (a) Reduction of CO_2 to C_1 products, and the competing HER. (b) The scaling relationship of free energies (COOH* vs H*) on TM and non-TM surfaces.[22]

The theoretical study demonstrated that proton-assisted electron transfer to CO_2 on the metal surface resulted in HCOO* or COOH* intermediates (**Figure 1.1.4**). By transferring the second proton-electron pair, the HCOOH can be formed via the reduction of HCOO* and COOH* intermediates. However, the CO is only produced from the COOH* intermediate, whereas the HCOO* can reduce to H_2COO*, which competes with the HCOOH formation.[22] The H_2COO* is the intermediate for forming CH_4 and CH_3OH, etc. DFT calculations also revealed the scaling relationship (COOH* vs H*) on various transition metals (TMs), while the scaling relation between HCOO* and H* is found to be extremely weak. This indicated that the competing HER side reaction is challenging to address if CO_2 reduction on the TM surface occurs via a COOH* intermediate, because the adsorption strengths of COOH* and H* are strongly linearly correlated. Therefore, finding or designing a metal surface that strongly adsorbs COOH* but not H* would be difficult. On the other hand, the weak scaling between HCOO* and H* offers a promising opportunity to overcome HER competition by identifying a metal surface that strongly adsorbs HCOO* but not H*.

1.1.3 Multi-carbon Products Formation

C–C bond formation is the key step of forming multi-carbon products during CO_2RR. To stabilize the adsorbed intermediate and enhance the formation of C1 products, strong CO_2 binding is preferred, with weak binding of these C1 products needed to prevent further dimerization. The C_2 products usually result from the strong adsorption of particular C_1 species, such as CO*, which allows further dimerization and proton-electron pair transfer.[23] Studies have suggested that the formation of the CO dimer intermediate is the key species in the C_2 pathway.[24] To form the multi-carbon products, the intermediate coupling is required on the electrocatalyst surface. Therefore, it is highly thermodynamically unfavourable. Among all TMs, Cu-based materials are known as ideal electrocatalysts for CO_2 electroreduction. Notably, Cu-based catalysts can convert CO_2 into various hydrocarbons, including C_2 products, with reasonably high efficiency.[25-27] Based on that, the studies of Cu-based CO_2RR electrocatalysts are mainly focused on corresponding catalytic mechanisms for the formation of C_2 products.

Table 1.1.2 Reduction potentials for CO_2 reduction to various C_{2+} products.[14]

Reduction Reaction of CO_2	E^0 [V vs. RHE]
$2CO_2 + 8H^+ + 8e^- \rightarrow CH_3COOH_{(aq)} + 2H_2O$	0.11
$2CO_2 + 10H^+ + 10e^- \rightarrow CH_3CHO_{(aq)} + 3H_2O$	0.06
$2CO_2 + 12H^+ + 12e^- \rightarrow C_2H_5OH_{(aq)} + 3H_2O$	0.09
$2CO_2 + 12H^+ + 12e^- \rightarrow C_2H_{4(g)} + 4H_2O$	0.08
$2CO_2 + 14H^+ + 14e^- \rightarrow C_2H_{6(g)} + H_2O$	0.14
$3CO_2 + 18H^+ + 18e^- \rightarrow C_3H_7OH_{(g)} + 2H_2O$	0.10

Numerous efforts have been made to investigate the formation of C_2 products on Cu-based material surfaces, aiming to identify the intermediates along the reaction pathways.[28] Theoretical studies based on ab initio calculations have proven an effective approach for rationalizing the activity of various Cu-based catalysts. The metallic Cu(100) facet is particularly selective for C_2 product formation at low overpotential, while the Cu(111) surface generates C_2 products at high overpotential via the methane pathway.[29] Studies also claimed that the C_2 products are formed via a selectivity-determining intermediate, which arises from common intermediates on Cu(100).[30] Cu alloys, such as CuZn and CuAg, can form C_2 products through an insertion-type mechanism (CO inserting into Cu–CH_2 species).[31] Other catalysts such as NiGa,[32] PdAu,[33] and N-doped carbon[34] also show the ability to convert CO_2 into C_2 products via CO_2RR, but not with the same efficiency as Cu-based materials. Besides, the C_{3+} products are highly thermodynamically unfavourable and rarely formed during CO_2RR. A possible mechanism for forming C_{3+} products is polymerization of -CH_x- or CO insertion, which can yield FE up to 20% even with suitable Cu-based catalysts.[35-36] NiP inorganic compound emerged as a promising candidate for producing C_{3+} products with excellent FE up to 70% via electroreduction of CO_2.[37]

1.2 Advanced Catalytic Materials

1.2.1 Atom Catalysts

Unlike conventional heterogeneous catalysts, which utilize surface atoms only during catalysis, ACs can achieve maximum atom utilization and outstanding activity.[38-40] The ACs need to stabilize isolated atoms with suppression of aggregations. Hence, an ideal supporting substrate that can strongly bind single atoms is required, and carbon-based materials are widely employed as supports in SAC owing to their interesting properties. **Table 1.2.1** summarizes the performance of ACs with various supporting materials for CO_2RR.

Table 1.2.1 The performance of ACs with various supports for CO_2RR.

Catalysts	Main product	FE	Voltage	Electrolyte
Ni-N-Gr[41]	CO	>90%	-0.7 to -0.9 V	0.1 M $KHCO_3$
CoPc-CN/CNT[42]	CO	96%	-0.52 V	0.1 M $KHCO_3$
Ni-doped g-C_3N_4[43]	CO	99%	-0.81 V	0.5 M $KHCO_3$
NiN-GS[44]	CO	93.2%	-0.7 V	0.1 M $KHCO_3$

Ni SAs/N-C[45]	CO	71.9%	-0.9 V	0.5 M $KHCO_3$
Co-N_2[46]	CO	94%	-0.52 V	0.5 M $KHCO_3$
Co-N_5/HNPCS[47]	CO	99.4%	-0.79 V	0.2 M $NaHCO_3$
Fe/NG[48]	CO	80%	-0.6 V	0.1 M $KHCO_3$
Fe-N-C[49]	CO	93%	-0.47 V	0.1 M $KHCO_3$
Co-N-C[49]	CO	45%	-0.48 V	0.1 M $KHCO_3$
Ni-NG[50]	CO	90%	-0.87 V	0.5 M $KHCO_3$
C-Zn_1Ni_4 ZIF-8[51]	CO	97.8%	-0.63 V	1 M $KHCO_3$
ZnN_x/C[52]	CO	95%	-0.43 V	0.5 M $KHCO_3$
Cu-CeO_2[53]	CH_4	58	- 1.8 V	0.1 M $KHCO_3$
NiPor-CTF[54]	CO	97%	-0.9 V	0.5 M $KHCO_3$
Ni-N-C[55]	CO	85%	-0.7 V	0.1 M $KHCO_3$
CuSAs/TCNFs[56]	MeOH	44%	-0.9 V	0.1 M $KHCO_3$
Ni SAs/NCNTs[57]	CO	97%	-0.9 V	0.5 M $KHCO_3$
Ni–N–MEGO[58]	CO	92.1%	-0.7 V	0.5 M $KHCO_3$
$Sn^{\delta+}$/NG[59]	$HCOO^-$	74.3%	-1.6 V (vs SCE)	0.25 M $KHCO_3$
CoP/CNT[60]	MeOH	44%	-0.94 V	0.1 M $KHCO_3$
$Cu_{0.5}$NC[61]	EtOH	55%	-1.2 V	0.1 M $CsHCO_3$
$Cu_{0.4wt\%}$/C[62]	EtOH	91%	-0.7 V	0.1 M $KHCO_3$
SA-Zn/MNC[63]	CH_4	85%	-1.8 V (vs SCE)	1 M $KHCO_3$
CTF-Cu[64]	C_2H_4 CH_4	30.6% for C_2H_4 72.0% for CH_4	~ -1.5 V (vs SCE)	0.3 M KCl
Cu-SA/NPC[65]	acetone	36.7%	-0.96 V	0.1 M $KHCO_3$

N-C-CoPc[66]	CO	90%	-0.58 to -0.78 V	0.5 M $KHCO_3$
Cu-CD[67]	CH_4	78%	-1.44 V	0.5 M $KHCO_3$
Pyr-GDY-Cu[68]	HCOOH	45%	- 1.1 V	0.1 M $KHCO_3$
Ag/GDY/CC[69]	CO	92.1%	-1.3 V	0.1 M $KHCO_3$
CoPc/GDY/G[70]	CO	96%	-0.9 V	0.1 M $KHCO_3$

1.2.2 GDY-Supported Transition Metal Atomic Catalysts[1]

GDY, an allotrope of carbon, has drawn tremendous attention due to its broad applications in energy storage and conversion (**Figure 1.2.2**). The GDY is a type of graphyne comprising benzene moieties and butadiyne linkers, forming a two-dimensional plane framework. Li and co-workers reported a methodology for synthesizing large-area GDY films under mild conditions in 2010.[71] The literature also summarizes the strategies for modifying the electronic structure of the GDY framework.[72] Approaches such as heteroatom doping, metal atom anchoring, external strain, and stacking configuration play a significant role in tuning GDY-based ACs. Among these methods, heteroatom doping is the most popular way to synthesize various GDY derivatives with different electrochemical properties.[73] The doping methods can modify the electronic structure because of the electronegativity difference (carbon vs dopant), which induces charge redistribution that modifies the band structure.

---

[1] **H. H. Wong**, M. Sun and B. Huang, 2D Mater. 2021, 8 (4), 044009.

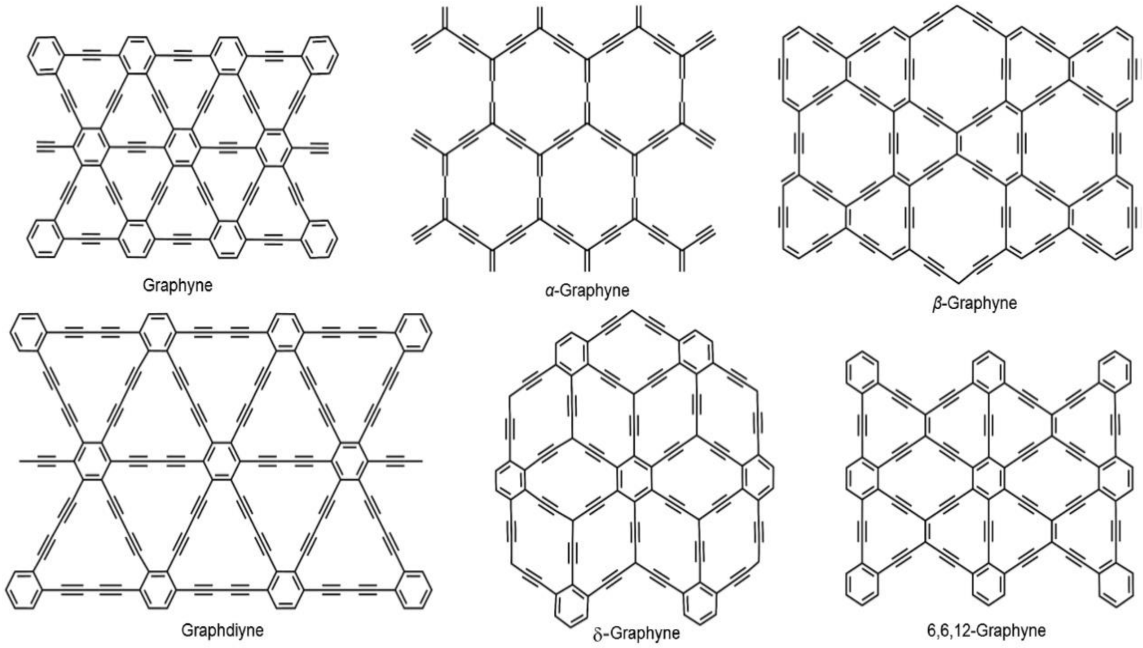

Figure 1.2.2 Chemical structure of various Graphynes.

For instance, N atoms are the most used dopant to replace C atoms on the framework of carbon materials because of their greater electronegativity (3.04) compared with the C atom (2.55).[74] The stronger electron-withdrawing ability of the N atom draws electrons from the neighboring C atom, creating a positively charged C atom that favors the adsorption of negatively charged intermediates.[75] Based on this, doping N atoms on the GDY endows it with potential as a metal-free electrocatalyst for various reactions.[76-78] The N-doping of GDY can be achieved via heat treatment under high-purity NH_3, in which some of the carbon atoms will be replaced by N atoms in a uniform distribution, forming the N-doped GDY with pyridinic N, imine N and graphitic N (**Figure 1.2.3**).[79] The N-doped GDY exhibits improved catalytic performance due to increased electronic conductivity and the presence of defects. For example, Dai and coworkers reported that replacing the sp^2 carbon of the acetylene bond enabled the N-doped GDY to exhibit metallic properties, significantly facilitating electron transfer for electrocatalytic reactions.[80] Similar to introducing N atoms, introducing F atoms into the GDY framework can also effectively modulate GDY electronic properties due to the significant electronegativity difference. The doping of F atoms on GDY can often induce larger charge polarization due to the higher electronegativity of F compared to that of the N atom. In the F-doped GDY, the charge localization on the electroactive C2 sites in the acetylene chain was greatly enhanced due to the strong C−F bonding formation, which can induce p-electronic orbital redistribution. As a result, the electron transfer is significantly enhanced on the F-doped GDY. The F-doped GDY can be used as a bifunctional metal-free electrocatalyst for HER, OER, and overall water splitting with outstanding catalytic activity.[81]

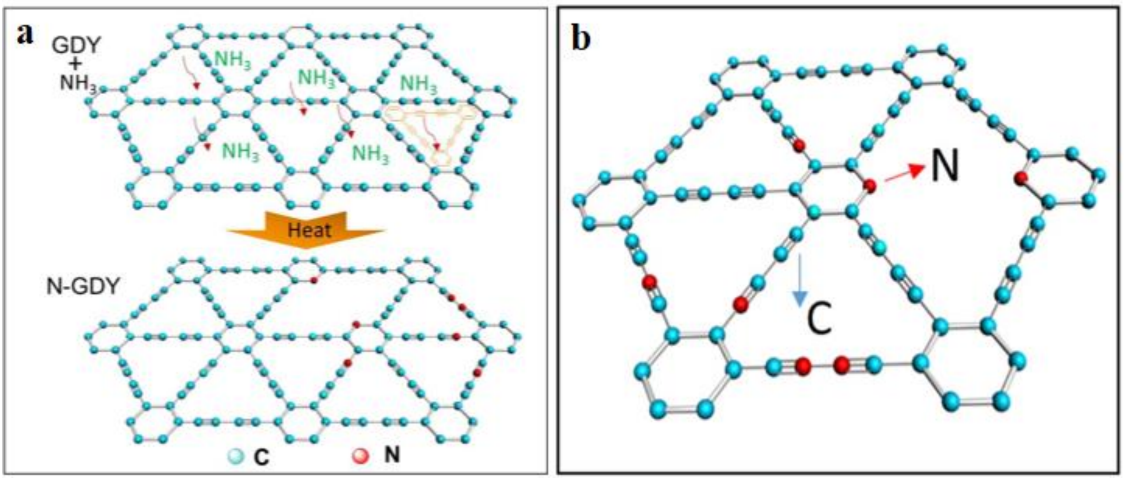

Figure 1.2.3 (a) Schematic representation of the formation of N-doped GDY. (b) The possible N-doping positions on the GDY framework.[79]

Heteroatoms with lower electronegativity are also used as dopants for functionalizing GDY. The S atom can also be used as a dopant to improve the electronic properties of GDY. For example, the introduction of S atoms significantly improved electrical conductivity. S-GDY preparation is readily easy by annealing the GDY and octasulfur (S_8) mixture at 350°C, in which the uniform pores offer excellent adsorption sites for entrapping polysulfides via the C−C triple bond.[82] The S-anchored GDY exhibits excellent electrochemical performance, with remarkable potential for energy storage applications, including Li–S and Mg–S batteries.[83-84] Also, theoretical studies indicated that the S atom tends to replace the sp-C rather than the sp^2-C in the GDY framework for substitutional doping.[85-86] The as-prepared S-doped GDY has displayed excellent electrocatalytic performances due to the enhancement of positive charge on the active sites, particularly when co-doped with another heteroatom such as N.[87-88]

On the other hand, the electron-deficient nature of the B atom has led to a distinct electronic modulation in carbon materials. The substitutional doping of B at the sp^2-C site in the GDY framework is favoured, as the sp^2-C atom provides higher coordination and thus increases structural stability.[89] The B-doped GDY framework can be synthesized via a bottom-up approach on copper foil, and the resulting B-doped GDY exhibits outstanding electrical conductivity for sodium-ion storage applications.[90] Also, the B atom substitution in GDY enhances catalytic performance in several ways, based on the unique features of the B atom. An obvious benefit from B-doping is the existence of empty p-orbitals on B atoms, which can react readily with a Lewis base during catalytic reaction. As a result, GDYs doped with B have been used as NRR electrocatalysts with outstanding performance.[91-92] Notably, B atom co-doping with other heteroatoms such as N or TMs atom also endows GDY with the ability to catalyse a diverse type of electrochemical reaction, including ORR,[93] and CO_2RR.[94-95] These enhancements of catalytic activity on heteroatom co-doped GDY can be attributed to the neighbouring effects (**Chapter 1.2.3**).

GDY is characterized by the abundance of sp-C and sp^2-C, and the high density of uniform triangular nanopores. These features have provided an ideal environment for anchoring various TM atoms, forming TM-GDY ACs with excellent stability and catalytic activity.[96] Studies have revealed that GDY can strongly bind with TM atoms via the acetylene carbon chain on GDY, which most TM atoms favor anchoring in the 18C alkyne hexagonal ring site. Similar to non-metal heteroatom doping, embedding TM atoms activates catalytic activity through charge transfer and redistribution. The research has also shown that the electron transfer differs among different anchoring TMs on GDY. Moreover, a critical challenge is loading a zero-valent TM atom. Beneficial from the advantage of GDY as the supporting substrate, TM atoms such as Ni, Fe, Co, Pd and Pt have been used to form zero-valence GDY-AC due to their evident energy barrier difference between gaining and losing electrons, which is regarded as a breakthrough in the field of ACs.[97-98]

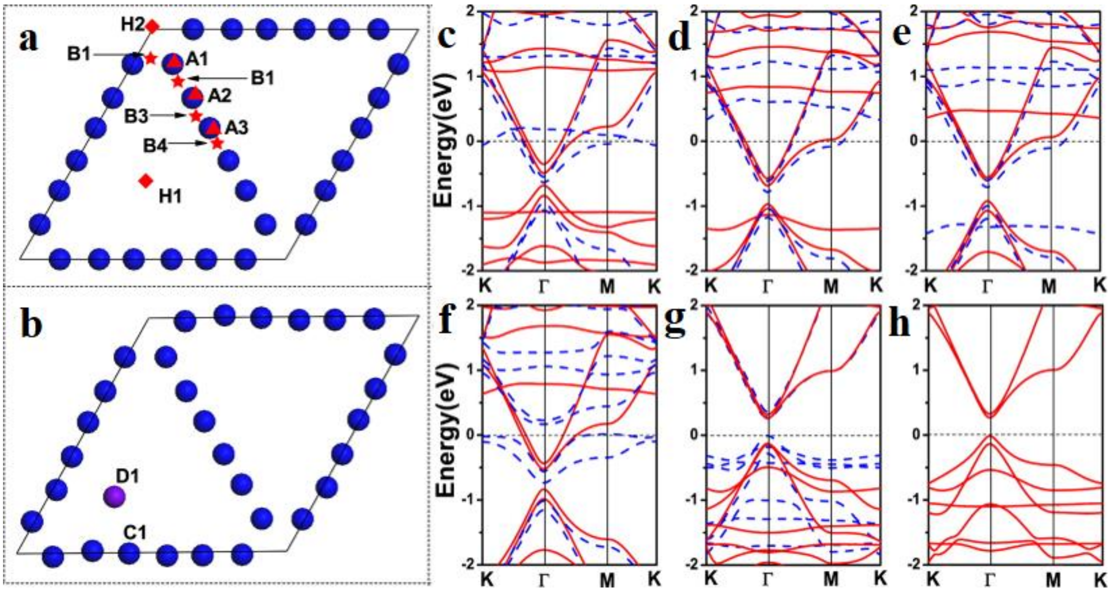

Figure 1.2.4 (a) Pristine GDY, where the possible adsorption sites of TM atoms are represented as Ai (top), Bi (bridge), and Hi (hollow). (b) The most favourable adsorption location (D1) for the TM atoms after relaxation. The carbon and TM atoms are represented by the blue and pink spheres, respectively. The modification of band structures of GDY after the adsorption of (c) V, (d) Cr, (e) Mn, (f) Fe, (g) Co, and (h) Ni, where the majority spin channels represented by red line and minority spin channels represented by dashed blue lines.[99]

Recently, studies have successfully designed highly efficient GDY-ACs using earth-abundant non-NMs.[100-101] Regarding the use of inexpensive TMs in GDY-ACs, Sun's group has conducted a systematic first-principles study based on DFT-U calculations on the adsorption of 3d-TM atoms (V, Cr, Mn, Fe, Co, and Ni) on the GDY layer (**Figure 1.2.4**).[99] The calculation results suggest that the magnetism of TM-GDY is due to distinct spin polarization arising from the anchoring of V, Cr, Mn, Fe, and Co atoms. Meanwhile, adsorption of the aforementioned TMs also leads to varying degrees of bandgap narrowing and electron transfer, depending on the adsorbed TM. Notably, the DFT study also indicated that the transferred charge increased with the adsorption energy between atoms and GDY.[102] Hence, electron transfer plays a crucial role in stabilizing adsorbents (graphene/GDY) in the presence of heavy metal atoms. GDY-ACs based on non-precious metals are a potential candidate for OER/HER/NRR. For instance, the reduction of Ni^{2+} and Fe^{3+} ions can anchor the zero-valent Ni and Fe atoms on GDY. The resulting Ni^{0}-GDY and Fe^{0}-GDY demonstrate outstanding catalytic activity toward HER with low overpotentials of 88 mV and 66 mV (at 10 mA cm^{-2}), respectively.

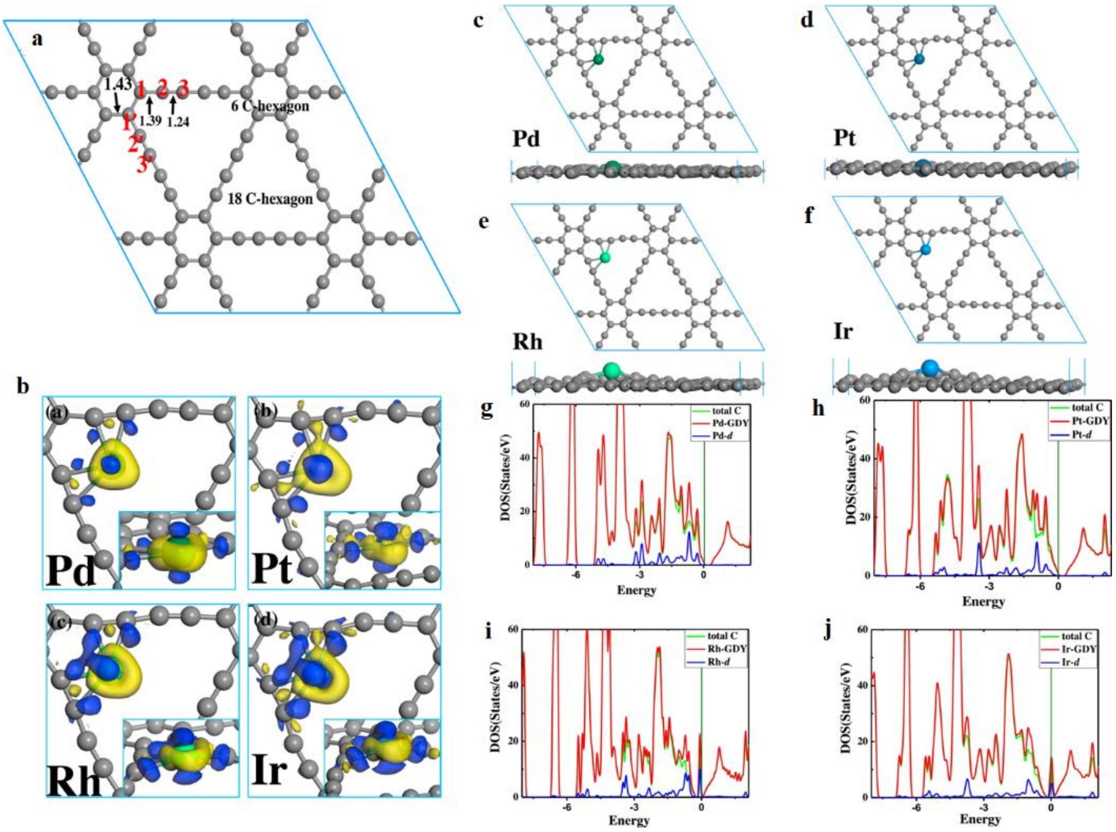

Figure 1.2.5 (a) The most stable configurations of the pristine GDY. (b) The charge density difference is presented for the NM/GDY, where charge depletion and accumulation are represented by blue and yellow regions, respectively. (c-f) The atomic structure of NM/GDY. (g-j) The density of states (DOS) profiles for NM/GDY.[103]

Furthermore, NM can also be incorporated into GDY with reduced metal loading. Yang et al.[103] have systematically studied the anchoring of Pd, Pt, Rh, and Ir on the GDY framework, suggesting that Pd and Pt easily achieve high concentration adsorption (**Figure 1.2.5**). In contrast, Rh and Ir atoms have low concentrations on the GDY, which is suitable for forming GDY-ACs. The study also showed that the NM atoms tend to adsorb on the GDY via a covalent bond, as evidenced by the accumulation of electron density at the NM-carbon bond and a small electron density difference between the NM and the adjacent carbon. In electromagnetism, the results showed that the NM adatoms in the GDY have zero magnetic moment, with no spin polarization. Additionally, the downshift of the conduction band upon adsorption of Pd, Pt, Rh, and Ir leads to a significant decrease in the band gaps. In particular, the apparent narrowing of the bandgap in Rh-GDY arises from the metal 3d states near the Fermi level (E_F), which push the valence band upwards. In contrast, the 3d states on Ir-GDY lie between the conduction and valence bands, closing the bandgap and giving rise to a metallic state with a zero bandgap. The strong covalent bonds are formed through hybridization between the NM 3d states and carbon states (hybridized). More importantly, the lowest unoccupied molecular orbital (LUMO) and highest occupied molecular orbital (HOMO) are primarily located on the NM sites, indicating that these sites serve as the active centers for catalytic reactions. For instance, the highest occupied state on the NM site can act as an electron donor to react with electronically deficient species. In contrast, the lowest unoccupied state can act as an electron acceptor, reacting with electron-rich species.

1.2.3 Neighbouring Effects on Atomic Catalysts[2]

Although SACs have several advantages, including superior catalytic activity, maximized metal atom utilization, and well-defined active centers, the single isolated active center on SACs also limits their ability to optimize the binding energy of different intermediates. Therefore, for electrocatalytic reactions such as CO_2RR involving multiple intermediates, SACs suffer from the inherent limitation of linear scaling

---

[2] **H. H. Wong**, M. Sun, T. Wu, C. H. Chan, L. Lu, Q. Lu, B. Chen and B. Huang, eScience 2024, 4 (1), 100140.

relations and lack ensemble sites for intermediate coupling processes.[104-105] Regarding such limitations, the cooperation between the active centre and the neighbouring atoms in ACs can give unique and interesting phenomena in electrocatalytic performance. For instance, the surrounding atoms can induce electronic modulation at the TM active site via charge redistribution, thereby further enhancing its activity.

Based on this, a literature review summarizes the synergistic effects of GDY-based electrocatalysts.[106] Studies have revealed that the activity of heteroatom-doped TM-GDY and GDY-DACs has been significantly improved compared to non-doped TM-GDY and TM-GDY SACs, due to the synergistic effects between sites. Experimental and theoretical investigations have demonstrated that the surrounding atoms can induce electronic modulation of the active metal centre in ACs and can participate in the CO_2RR catalytic process as second-assisted active or adsorption sites. These kinds of neighbouring effects can provide tremendous benefits to the performance of CO_2RR catalysis. The neighboring interactions on ACs, including carbon−heteroatom (C−X) interactions, metal−carbon (M−C) interactions, and M−X−C interactions, in which the coordination environment of the active site is critical for the activity and selectivity of CO_2RR (**Figure 1.2.6**). In general, the vacant and occupied d-orbitals on TMs contribute to the activity of TM-based electrocatalysts, as these vacant and occupied orbitals can form σ-donation or π-backdonation with molecules.[107-108]

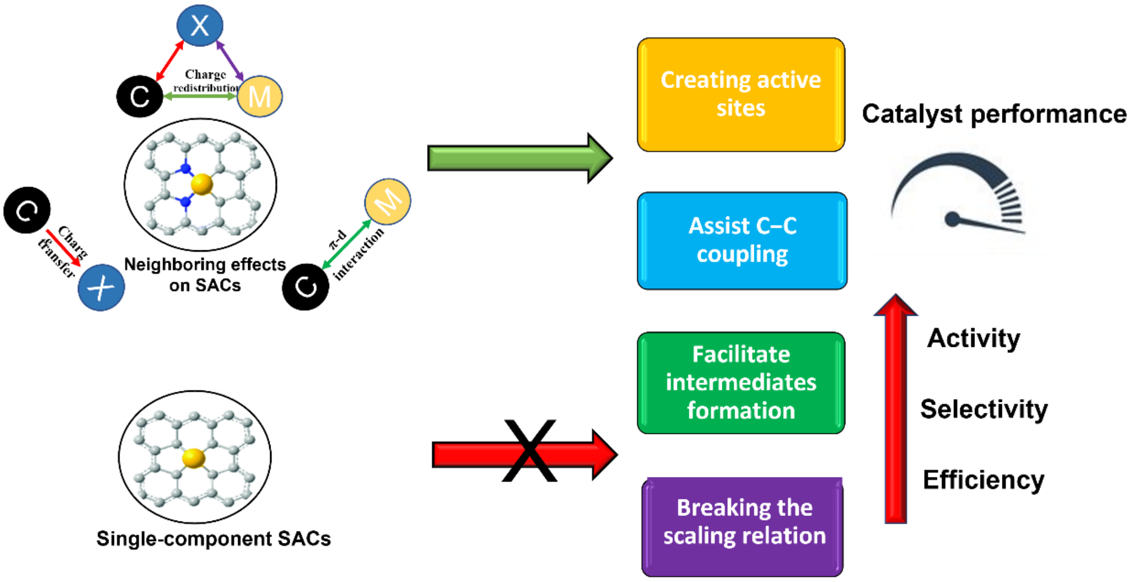

Figure 1.2.6 The benefits of neighbouring effects on ACs for catalyst performance, compared to ACs lacking neighbouring effects.

Although pristine carbon is typically regarded as electrochemically inactive due to the absence of d-orbitals, several studies have shown that efficient carbon-based metal-free SACs can be developed through heteroatom doping.[109-110] The heteroatom dopant with different electronegativity can induce a significant polarization to trigger the CO_2RR catalytic activity of carbon atoms.[111] In such circumstances, the heteroatoms with larger electronegativity will be negatively charged and act as a Lewis base in the CO_2RR process. For example, N-doped graphene has shown electrocatalytic activity in the reduction of CO_2 to CO and HCOOH, as the negatively charged N-group can be regarded as a Lewis base that reacts readily with the Lewis acid CO_2.[112] Studies have supported the favourable CO_2 adsorption on the doped pyridinic-N atom in the initial CO_2RR process.[113-116] However, the N atom tends to be positively charged in graphitic-N due to the transfer of an electron from the N to the π-conjugated state, verified by the microscopy/spectroscopy and DFT calculation.[117-119] The positively charged N created a negatively charged nearby carbon atom due to the screening effect. Regarding the above examples of N-doping on carbon materials, the charge density distribution varies with the doping location, providing an opportunity to tune the reactivity of surface atoms according to the Lewis acid-base theory of C−X interactions.

Additionally, the M−C interaction on ACs is significantly influenced by the C atom hybridization. The TMs tend to bind with the sp- and sp^2-C due to the existence of active 2p-orbitals for TM−C π-d interaction. Hence, carbon materials composed of sp^2-hybridized carbon, such as graphene, carbon nanotubes, and mesoporous carbon, are frequently utilized as supports for TM atoms.[56, 120-121] Notably, the charge redistribution between the TM atom and nearby carbon is realized via significant overlap between the 2p-orbitals on carbon and d-orbitals on the TM atom, while the incorporation of 2p-orbitals into d-orbitals results in a diminished d-character of the Pt atom, and the disruption of the scaling relation stems from the d-band center theory.[122] Another example is illustrated by the delocalized charge distribution and the significant π→d and d→π* interactions observed in TM-GDY systems, in which the sp-C atoms on TM-GDY modulate the electronic structure of the metal atom, suppressing H_2 production and enhancing selectivity toward CH_3OH (**Figure 1.2.7**).[123]

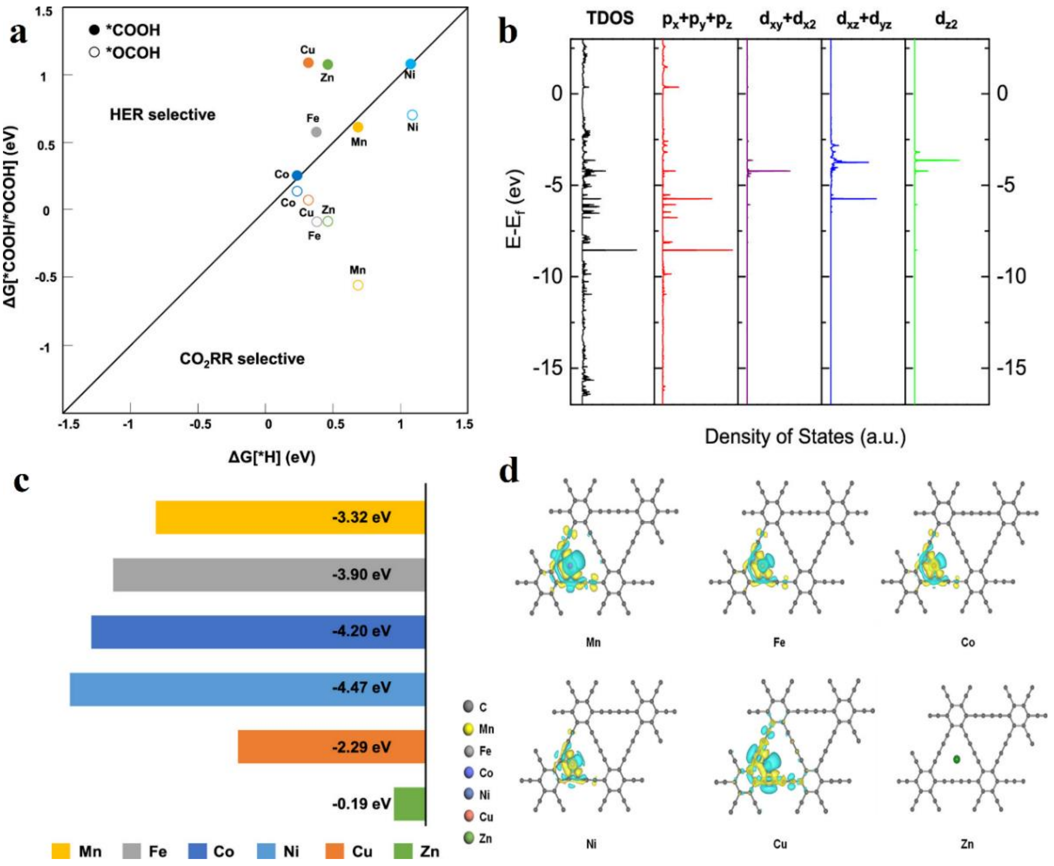

Figure 1.2.7 (a) Comparison between the CO2RR and HER on various TM–GDY. (b) TDOS and PDOS of Cu–GDY that show π → d interactions. (c) The adsorption energy of TM atoms on GDY. (d)The differential charge density of TM–GDY, where the yellow isosurfaces represent regions of charge accumulation in space, whereas the blue isosurfaces denote areas of charge depletion.[123]

The doping of heteroatoms also significantly improves the activity and stability of the TM-SACs by forming a more stable M−X−C interaction. However, not all heteroatoms can interact strongly with TM atoms, such as M−B bonding, which is infrequently reported in synthesized TM-SACs due to the weak interaction between TM and the B dopant in B-doped carbon materials.[124] In addition, TM atoms tend to aggregate on the surface of B-doped graphene, which accounts for the infrequent reporting of the

M−B−C moiety in carbon-supported TM-SACs. In contrast, M−N−C structures exhibit exceptional stability, resisting thermal aggregation and leaching.[125] For instance, the CN (N atoms) of the metal centre in Fe–N–C and Ni–N–C catalysts has significantly impacted the CO_2RR performance.[55] The study revealed that the d-band centre position is correlated with N coordination, with the electron transfer from the Ni atom to the surrounding atoms decreasing as N coordination decreases, leading to an upshift in the Ni d-band centre and enhanced activation of CO_2 (**Figure 1.2.8**).

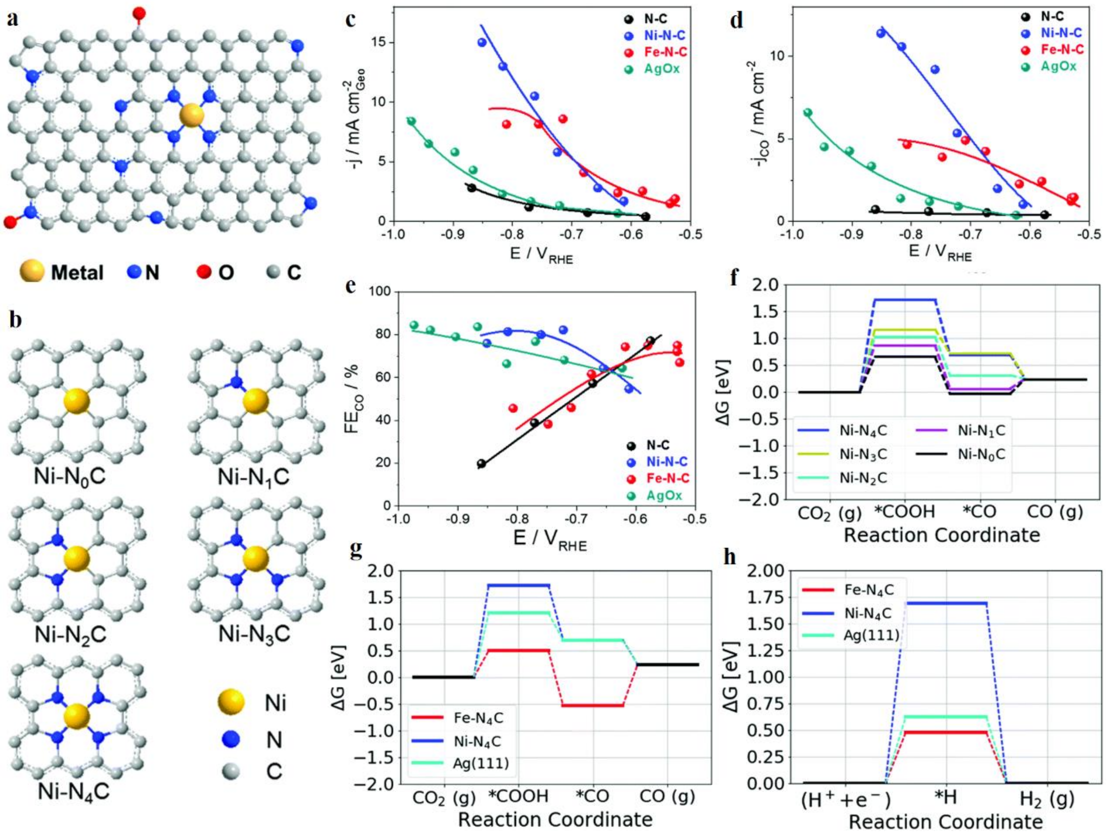

Figure 1.2.8 (a) Structure of the of M–N–C SACs. (b) Various M–N_x moieties on the synthesized M–N–C SACs. (c) Absolute geometric current densities. (d) Geometric CO production current densities. (e) FE of CO production. (f) The binding strength of the *COOH and *CO intermediates under different CN (N atoms) of Ni. (g) Free energy profiles of CO_2RR (CO formation). (h) Free energy profiles of the competitive HER.[55]

It is widely accepted that the exceptional catalytic activity of ACs originates from the characteristics of isolated metal atoms. However, the catalytic potential of neighboring carbon sites has received relatively little attention. Research has further demonstrated that carbon atoms adjacent to anchored metal atoms can also exhibit catalytic activity, influenced by electronic modulation induced by the anchored metal atom.[126] For instance, Sun et al.[127] have conducted a comprehensive DFT study on the TMs and lanthanide-based GDY-SACs. The calculation results indicated that the metal-atom-modified alkyl chains on GDY are the preferred adsorption sites for CO_2 binding, owing to their stronger affinity for CO_2 than the metal sites. Especially, the adsorption of CO_2 is highly favorable on lanthanide-based GDY-SACs without evidential over-binding, in which the moderate binding strength help realize the C_{2+} formation during CO_2 reduction.

Chapter 2. Methodology

2.1. Density Functional Theory (DFT)

Ab initio calculations, also known as first-principles methods, are one of the most significant theoretical approaches for investigating material and structural properties at the atomic level. In particular, the first principles of methods have proven effective in studying chemical reactivity and catalysis. DFT is the dominant computational quantum-mechanical modelling method among first-principles methods. The DFT has been well established for simulating periodic many-electron systems, providing an alternative approach to solving the complex Schrödinger equation based on the electron density. As a result, DFT can achieve similar accuracies with much less computation than other electronic structure methods. Over the past few decades, the DFT method has been widely applied to predict the geometry and electronic structure of catalyst surfaces, playing a crucial role in improving the efficiency of existing catalysts and facilitating the development of novel catalysts.

2.1.1 Schrödinger equation

A fundamental equation of quantum mechanics is the Schrödinger equation, and the wavefunction (Ψ) of a quantum system, including both electrons and nuclei, is the solution (eigenfunction) of the equation. For a quantum system with N electrons with coordinates r_i and K nuclei with position R_k, the general time-independent, non-relativistic Schrödinger equation is expressed as:

$$\hat{H}\Psi\,(r_1, \dots, \mathrm{r}_N,\ \mathrm{R}_1, \dots, \mathrm{R}_K) = \ \mathrm{E}\Psi\,(\mathrm{r}_1, \dots, \mathrm{r}_N, \mathrm{R}_1, \dots, \mathrm{R}_K) \qquad (2.1)$$

$$\hat{H} = \underbrace{-\frac{1}{2}\sum_{i=1}^{N}\nabla_i^2}_{\hat{T}_e} + \underbrace{\frac{1}{2}\sum_{i\neq 1}^{N}\frac{1}{|r_i-r_j|}}_{\hat{V}_{ee}} - \underbrace{\sum_{i=1}^{N}\sum_{k=1}^{K}\frac{Z_k}{|r_i-R_k|}}_{\hat{V}_{en}} - \underbrace{\frac{1}{2M_k}\sum_{k=1}^{K}\nabla_k^2}_{\hat{T}_e} + \underbrace{\sum_{k\neq l}^{K}\frac{Z_k Z_l}{|R_k-R_l|}}_{\hat{V}_{nn}} \quad (2.2)$$

The E is the total energy (eigenvalue) for the system, and the $\hat{H}$ is the Hamiltonian operator. The 1st term $\hat{T}_e$ is the kinetic energy operator of the electron. The 2nd term $\hat{V}_{ee}$ is the Coulomb repulsive energy between electrons. The 3rd term $\hat{V}_{en}$ is the attractive interaction between electrons and nuclei. The 4th term $\hat{T}_e$ and 5th term $\hat{V}_{nn}$ are the kinetic energy of the nuclei and the Coulomb nuclei-nuclei repulsive energy, respectively. The Z_k and M_k are the charge number and masses of the atomic nuclei. The first approximation in quantum chemistry is the Born-Oppenheimer approximation. It assumes that electronic motion is much faster than nuclear motion since each proton or neutron in a nucleus is more than 1800 times heavier than an electron. Therefore, the heavy nuclei can be treated as a fixed particle when describing the atom's electrons, and the wavefunction of nuclei and electrons is separable.[128]

$$\Psi = \psi_n\,(\mathrm{R}_1, \dots, \mathrm{R}_K) \times \psi_e\,(\mathrm{r}_1, \dots, \mathrm{r}_N) \quad (2.3)$$

This approximation allows us to neglect the nuclear coordinates. As a result, the wavefunctions will be functions only on electronic coordinates when calculating the electronic energy, and the electronic Hamiltonian $\hat{H}_e$ is:

$$\hat{H}_e\psi_e\,(\mathrm{r}_1, \dots, \mathrm{r}_N) = \mathrm{E}_e\psi_e\,(\mathrm{r}_1, \dots, \mathrm{r}_N) \quad (2.4)$$

$$\hat{H}_e = \hat{T}_e + \hat{V}_{ee} + \hat{V}_{en} \quad (2.5)$$

The Schrödinger equation with the electronic Hamiltonian $\hat{H}_e$ and determined the electronic energy by solving the 3N-dimensional electronic wavefunction ψ_e. Moreover, the computational cost of solving this 3N-dimensional equation increases exponentially with the number of electrons.

2.1.2 Hartree-Fock method

For many-electron systems with N electrons, the electron wavefunction is a function of each of the coordinates of all electrons. Meanwhile, it is possible to approximate the electron wavefunction as a product of the individual electron wavefunction, and this combination of the individual wave function is known as a Hartree product:

$$\psi_{HP}(r_1, \ldots, r_N) = \phi_1(r_1)\, \phi_2(r_2), \ldots, \phi_N(r_N) \tag{2.6}$$

Based on that, solving the Schrödinger equation is simplified to a 3-dimensional eigenvalue problem for individual ϕ (r_i) spatial orbital. Besides, fermions (such as electrons) have not only three spatial degrees of freedom, but also have an intrinsic spin coordinate ω (α or β), in which the notion χ(x) is represented by the spin-orbital:

$$\chi(x) = \begin{cases} \phi\,(r) \times \alpha \\ \phi\,(r) \times \beta \end{cases} \tag{2.7}$$

In addition, the Hartree product is not a good approximation because the Hartree product violates the Pauli exclusion principle and is not necessarily antisymmetric with respect to the interchange of any two fermions. Therefore, an antisymmetric wavefunction can be mathematically described by a Slater determinant:

$$\psi_e(r_1, r_2, \dots, r_N) = \frac{1}{\sqrt{\mathrm{N}!}} \begin{vmatrix} \chi_1(x_1) & \chi_1(x_2) & \cdots & \chi_1(x_N) \\ \chi_2(x_1) & \chi_2(x_2) & \cdots & \chi_2(x_N) \\ \vdots & \vdots & & \vdots \\ \chi_\mathrm{N}(x_1) & \chi_\mathrm{N}(x_2) & \cdots & \chi_\mathrm{N}(x_N) \end{vmatrix} \tag{2.8}$$

The Hartree-Fock method provides the variational ground state energy and molecular orbitals for given basis functions with the single determinant (mean-field) approximation. In the Hartree-Fock calculation, the Schrödinger equation for each electron is written as:

$$\left[-\frac{\mathrm{h}^2}{2\mathrm{m}_e}\nabla^2 + V_{(r)} + V_{H(r)}\right] \chi_\mathrm{j}(x_i) = \mathrm{E_j}\, \chi_\mathrm{j}(x_i) \tag{2.9}$$

$$V_{H(r)} = e^2 \int \frac{n(r')}{|r-r'|} d^3r' \tag{2.10}$$

Where the Hartree potential $V_{H(r)}$ is the Coulomb interaction of an electron with average electron density $n(\mathbf{r})$. To define the Hartree potential $V_{H(r)}$, the average electron density needs to be determined.

$$\mathrm{n(r)} = \sum_{\mathrm{i=1}}^{\mathrm{N}} [\phi_i(r)]^2 \tag{2.11}$$

The electron density can be obtained from the electron wavefunction, which is determined using the individual spin orbitals. By making a trial spin-orbital $\chi_i(x_i)$, the electron density $n(r')$ can be defined and used to solve the above single-electron Schrödinger equation for the spin-orbital $\chi_j(x_j)$. If the $\chi_j(x_j)$ is consistent with the $\chi_i(x_i)$, then these are the solutions to the Hartree-Fock problem. If those spin orbitals are not consistent, then a new trial spin-orbital $\chi_i(x_i)$ is needed to make the resulting $\chi_j(x_j)$ is converged. This procedure, known as the SCF or mean-field method, is widely used in quantum chemistry to describe many-electron systems. Mean-field methods can yield reasonable values for the total energies of atoms and molecules, but electron correlation introduces significant errors. To yield a more accurate result, the correlation energy must be approximated. This can be achieved using post-Hartree-Fock methods, such as configuration interaction (CI), which require a multi-determinant wavefunction to account for electron correlation. The multi-determinant wavefunction is a linear combination of configuration state functions:

$$\Psi = \underbrace{\mathrm{a}_0\Phi_{HF}}_{\substack{HF\\ grondstate}} + \underbrace{\textstyle\sum_{i=1}\mathrm{a}_i\Phi_i}_{\substack{Linear\ combination\ of\\ exciated\ slater\ determinant}} \tag{2.12}$$

In principle, the numerically exact solution to the Schrödinger equation can be obtained by considering all possible excitation configurations (Full CI). However, full CI is usually impractical, and only limited excitation configurations will be considered in practice, such as single excitation (CIS) and single- and double-excited (CISD). For calculations involving small numbers of atoms, wave-function-based Hartree-Fock methods can provide reasonably accurate results, especially when accounting for correlation energy. However, the computational expense for these calculations increases rapidly with the number of atoms, owing to the use of a large basis set to converge on the true solution of the Schrödinger equation. Therefore, DFT will be used to handle a system with many atoms.

2.1.3 Hohenberg–Kohn Theorems

In the Schrödinger equation, the properties of a many-electron system are based on a description of the motion of individual electrons, in which the wavefunction is a function of 3N coordinates for N electrons. Hence, solving such a 3N-dimensional wavefunction is mathematically very complicated. On the other hand, the DFT turns the 3N-dimensional wavefunction into a 3-dimensional electron density problem, in which the total electron density n(r) with N electrons is given by:

$$\mathrm{n(r)} = N \int \int \dots \int \psi^{*}{}_{e}\, (\mathrm{r}_1, \dots, \mathrm{r}_N)\, \psi_e\, (\mathrm{r}_1, \dots, \mathrm{r}_N) d^3 r_1 d^3 r_2 \dots d^3 r_N \tag{2.13}$$

If the ψ_e is a normalized wavefunction:

$$\int n(r)\, d^3 r = N \tag{2.14}$$

The entire field of the DFT rests on two theorems proved by Hohenberg and Kohn in 1964.[129] The first theorem states that all properties of a system can be calculated as an explicit or implicit functional of electron density, and hence, ground state energy from the Schrödinger equation is a unique function of the electron density $\mathrm{n_0(r)}$:

$$E_0 0 \;=\; \mathrm{E[n_0(r)]} \tag{2.15}$$

According to the variational principle, the energy calculated with all appropriate wavefunctions is always larger than or equal to the exact ground state energy ($\mathrm{E_{gs}}$):

$$\langle\Psi|\hat{H}|\Psi\rangle \geq \mathrm{E_{gs}} \qquad (2.16)$$

Therefore, by minimizing all possible wavefunctions with allowed N electrons, the ground state energy of a system can be determined. Within the framework of the DFT approach, a similar approach can be adopted to determine the ground-state electron density using the variational theorem for density. According to the variational theorem, the electron density that minimizes the total energy of the functional represents the actual electron density, corresponding to the complete solution of the Schrödinger equation:

$$\mathrm{E[n(r)]} \geq E_0 \qquad (2.17)$$

This minimum principle is the second HK theorem. Although the HK theorems simplify the many-body problems by using density functions, the theorems have not provided the exact expression of this functional.

2.1.4 Kohn-Sham Equations

From the Hohenberg-Kohn theorems, the energy of the many-body system is a functional of the electronic density. The total energy can be expressed as:

$$E\,[\mathrm{n}] = \mathrm{T}[\mathrm{n}] + E_{ee}[\mathrm{n}] + \int drV_{ext}(r)n(r) \tag{2.18}$$

$$E\,[\mathrm{n}] = F_{HK}[\mathrm{n}] + \int drV_{ext}(r)n(r) \tag{2.19}$$

The terms T[n] and E_{ee}[n] is the kinetic energy and electron-electron interaction energy, respectively. These two energies are called the universal functional F_{HK}[n] which is independent of the external potential. The total electronic energy can be approximated by the Thomas-Fermi functional:

$$E_{TF}[\mathrm{n}] = \underbrace{C_1 \int dr\, n(r)^{5/3}}_{\substack{K.E\ of\ the\ system\ of \\ non-interacting\ electron \\ with\ uniform\ density}} + \underbrace{\frac{e^2}{2}\int \frac{n(r)n(r')}{|r-r'|} d^3r\, d^3r'}_{Hartree\ energy\ V_H} + \underbrace{\int drV_{ext}(r)n(r)}_{E_{ext}[n]} \tag{2.20}$$

The Thomas-Fermi model approximates the kinetic energy functional based on the uniform electron gas.[130-131] On the other hand, the Hartree approach reintroduces a single-particle wavefunction to treat the unknown universal functional.[132]

$$\mathrm{E}[n] = F_{HK}[n] + \int drV_{ext}(r)n(r) + T_s\,[n] - T_s[n] + V_H - V_H \tag{2.21}$$

The $T_c[n]$ is the kinetic energy functional of a non-interacting particle system of density n. By rearranging the terms, the total energy of a system is expressed as:

$$\mathrm{E}[\mathrm{n}] = \underbrace{T_s[n] + V_H + \int drV_{ext}(r)n(r)}_{E^H[n]} + \underbrace{F_{HK}[\mathrm{n}] - T_s[n] - V_H}_{E_{xc}[n]} \tag{2.22}$$

$$E_{xc}[n] = \mathrm{T[n]} - T_s[n] \ + E_{ee}\mathrm{[n]} - V_H = E_x + E_c \tag{2.23}$$

The $E^H[n]$ is the energy based on the Hartree approach, which is a simple independent particle system. Whereas the new term $E_{xc}[n]$ is the exchange-correlation energy of an interacting system with density n. The $E_{xc}[n]$ stands for the correction of the approximation due to the exchange (E_x) and correlation (E_c) effect. As a result, the single-electron Kohn-Sham equation for a quantum system can be expressed as:

$$\left[\frac{\mathrm{h}^2}{2\mathrm{m}_e}\sum_{\mathrm{i=1}}^{\mathrm{N}} \nabla^2 + V_{ext} + V_{H(r)} + V_{XC(r)}\right] \psi_{\mathrm{i}}(r) = \epsilon_{\mathrm{i}}\, \psi_{\mathrm{i}}(r) \tag{2.24}$$

$$V_{ext} = \sum_{\mathrm{k}}^{\mathrm{K}} \frac{Z_k}{|r_i - R_k|} \tag{2.25}$$

$$V_{H(r)} = e^2 \int \frac{n(r')}{|r - r'|} d^3r' \tag{2.26}$$

$$\mathrm{n(r)} = \sum_{\mathrm{i=1}}^{\mathrm{N}} [\phi_i(r)]^2 \tag{2.27}$$

$$V_{XC(r)} = \frac{\delta E_{xc}[n(r)]}{\delta n(r)} \tag{2.28}$$

Where the $\psi_{\mathrm{i}}(r)$ and ϵ_{I} are the single-electron Kohn-Sham orbitals and energies, respectively. The V_{ext}, $V_{H(r)}$ and $V_{XC(r)}$ are the external potential, Hartree potential and the functional derivative of the $E_{xc}[n]$, respectively.

2.2 Exchange-Correlation Functionals

The exchange-correlation functional is the term in DFT that accounts for the $E_{xc}[n]$ on a many-body system. Since the exact form of the $E_{xc}[n]$ is not known, approximations must be made to represent the relation between exchange-correlation energy and electron density. For current DFT calculations, the exchange-correlation functional determines the accuracy of DFT in describing the interaction between electrons/electron-ion in the system. Therefore, selecting a suitable exchange-correlation functional to describe a given system is crucial for obtaining reliable results from DFT calculations.[133-134] Although numerous approximations exist for the exchange-correlation, they can be classified into three families: the LDA, GGA, and hybrid functional.[135]

2.2.1 Local Density approximation

The LDA is the simplest approximation for the exchange-correlation functions.[136] The LDA assumes that the electrons in a system locally behave as a uniform electron gas:

$$\mathrm{E}_{\mathrm{xc}}^{\mathrm{LDA}}[n(r)] = \int n(r)\, \epsilon_{\mathrm{xc}}[n(r)] d^3r \tag{2.29}$$

$$\epsilon_{\mathrm{xc}} = \epsilon_{\mathrm{x}}[n(r)] + \epsilon_{\mathrm{c}}[n(r)] \tag{2.30}$$

Where the ϵ_{xc} is the exchange-correlation energy per electron of a homogeneous UEG with electron density $n(r)$. The analytic form of the exchange of energy $\epsilon_{\mathrm{x}}[n(r)]$ for uniform electron gas can be expressed as:

$$\epsilon_{\mathrm{x}}[n(r)] = -\frac{3}{4\pi}[3\pi^2 n(r)]^{\frac{1}{3}} = \frac{3}{4\pi}k_F = \frac{3}{4\pi}\frac{(\frac{9\pi}{4})}{r_s} \tag{2.31}$$

The k_F is the Fermi wavevector, and the Seitz radius $r_s = \sqrt[3]{\frac{3}{4\pi\rho}}$ is the radius of a sphere containing one electron on average. For the $\epsilon_c[n(r)]$, the exact analytic expressions are not known, but the asymptotic expansion for high- and low-density limits has been derived:

$$\epsilon_c^{high} = a_0 ln(r_s) + a_1 + r_s(a_2 \ln(r_s) + a_3) \tag{2.32}$$

$$\epsilon_c^{low} = \frac{-b_0}{r_s} + \frac{-b_1}{{r_s}^{3/2}} + \cdots \tag{2.33}$$

The popular representations of correlation energy, including VWN80, PZ81 and PW92, have been developed based on the Quantum Monte Carlo data. Although the LDA is a simple approximation based on a homogeneous electron gas, it works well for systems whose density varies slowly, such as bulk metals. However, the accuracy of LDA is not enough for compounds with inhomogeneous density, and LDA produces overestimated adsorption energies. Those drawbacks limited the chemical applications of LDA, and a better exchange-correlation functional is required to improve LDA.

2.2.2 Generalized Gradient approximation

The GGA is an extension of the LDA functional, offering improved accuracy. It constructs the exchange-correlation functional in terms of the local electron density

$n(r)$ and its local gradient $\nabla n(r)$ in order to account for the inhomogeneity of the electron gas.[137-138] Therefore, the resulting exchange-correlation energy for GGA is similar to LDA but with an additional enhancement factor F_{xc} to describe the deviations of LDA functional from the uniform electron gas and satisfies the exact properties of the exchange-correlation hole.

$$\mathrm{E}_{\mathrm{xc}}^{\mathrm{GGA}}[n(r)] = \int n(r)\, \epsilon_{\mathrm{xc}}[n(r)]\, F_{xc}(n(r), s(r))d^3r \tag{2.34}$$

The $s(r)$ is the reduced density gradient and can be expressed as:

$$\mathrm{s}(r) = \frac{|\nabla n(r)|}{2(3\pi^2)^{1/3} n(r)^{4/3}} \tag{2.35}$$

Since the F_{xc} can be determined by exact constraints, the $\mathrm{E}_{\mathrm{xc}}^{\mathrm{GGA}}[n(r)]$ can be constructed without using empirical parameters. The GGA functionals offer a significant improvement over the LDA functional, particularly in reducing overestimation of adsorption energy while maintaining relatively low computational cost. The universal GGA approach in solid-state physics is the PBE functional, named after Perdew, Burke and Ernzerhof in 1996.[137] PBE is usually the default exchange-correlation functional in GGA and is widely used in studies of molecular interactions with metal surfaces. Although the PBE functional is neither the most accurate GGA approach for molecules nor the best functional for lattice parameters of bulk solids, it can provide reasonably good results when calculating systems containing both small organic molecules and bulk materials.[139-140]

2.2.3 Hybrid Exchange Functional

Advanced exchange-correlation functionals are developed by incorporating additional variables or mixing a certain amount of nonlocal Hartree–Fock (HF) exchange energy. As the name suggests, the hybrid exchange-correlation functional combines some of the exchange energy from the HF approximation, while the correlation component is still fully contributed by the GGA. This results in better accuracy in semi-local exchange and correlation functionals due to the error cancellation between semi-local exchange and correlation functionals.[141]

$$\mathrm{E}_{xc}^{hybrid} = \alpha \mathrm{E}_{x}^{HF} + (1-\alpha)\mathrm{E}_{x}^{GGA} + \mathrm{E}_{c}^{GGA} \tag{2.36}$$

The α is the mixing parameter in the hybrid functional calculation. One of the simple examples of hybrid functional is PBE0,[142] which mixes the PBE exchange energy with HF exchange energy in a ratio of 1:3 ($\alpha = 0.25$):

$$\mathrm{E}_{xc}^{PBE0} = \frac{1}{4}\mathrm{E}_{x}^{HF} + \frac{3}{4}\mathrm{E}_{x}^{PBE} + \mathrm{E}_{c}^{PBE} \tag{2.37}$$

Another popular hybrid functional used in molecular chemistry is B3LYP,[143] which employs Becke's three-parameter exchange functional and the Lee-Yang-Parr correlation functional to account for electron correlation. The exchange component of the B3LYP functional is contributed by 80% LDA exchange, 20% nonlocal HF exchange, and 72% of the Becke88 (B88) exchange functional. At the same time, the correlation part consists of 81% of the LYP correlation energy and 19% of the Vosko-Wilk-Nusair (VWN) correlation functional.

$$E_{xc}^{B3LYP} = (0.2E_x^{HF} + 0.8E_x^{LDA} + 0.72E_x^{B88}) + (0.19E_c^{VWN} + 0.81E_c^{LYP}) \quad (2.38)$$

The B3LYP functional can effectively describe systems with rapid electron density variation or long-range interactions, making it particularly suitable for calculations of molecular geometries, vibrational frequencies, and band gaps in molecular systems. However, the hybrid functionals are less accurate in calculating metallic systems than the LDA or GGA methods.[144] This is because hybrid functionals tend to suppress the DOS near the EF and overestimate the local magnetic moments of TMs.[145]

Chapter 3. Direct Cation Effects on CO Dimerization[3]

---

[3] **H. H. Wong**, M. Sun, T. Wu, L. Lu, Q. Lu, B. Chen, C. Hei Chan and B. Huang, Adv. Energy Sustainability Res. 2024, 5 (8), 2400110.

3.1 Introduction

Electrolytes are the fundamental component that controls electrochemical reactions. The electrolytes in electrochemical devices provide the medium for charge transfer, reactant movement, and electrochemical reactions. The influence of cations in electrolytes on CO_2RR was studied by Hori and co-workers in the 1980s, which suggested that the product selectivity (C_2 products) was significantly affected by the cationic species in the electrolytes.[146-148] In particular, the C_2H_4/CH_4 selectivity shows a trend $Li^+ > Na^+ > K^+ > Cs^+$, indicating that the 1st row AM^+ with larger size promotes the C_2 product formation during the CO_2RR. It is believed that the cation size significantly modulates the local pH near the cathode surface and, consequently, alters the product selectivity in CO_2 reduction.

Table 3.1.1 The ionic radii of 1st row AM^+ and their pK_a of hydrolysis.[149]

AM^+	Ionic radii (pm)	pK_a	
		Bulk	Cu electrode
Li^+	69	13.6	13.16
Na^+	102	14.2	11.44
K^+	138	14.5	8.49
Rb^+	149	14.6	7.23
Cs^+	170	14.7	4.32

Early investigations suggested that alkali cations in the electrolyte altered the potential at the OHP and electrode surface. The larger cations (e.g., Cs^+ and K^+) with lower solvation energies can more readily adsorb onto the electrode, thereby positively shifting the potential at the OHP and the surface. Hence, the H^+ concentration at OHP may naturally be lower (higher local pH), leading to higher C_2 selectivity due to the suppression of C_1 product formation and competing HER. Meanwhile, cation adsorption on the electrode surface is unfavourable at typical CO_2RR operating potentials.[150] However, a more recent investigation has shown that the adsorption of AM^+ (Li^+, Na^+, K^+, and Cs^+) on the Cu electrode is favourable at moderate CO_2RR overpotentials, with an equilibrium adsorption potential lower than −1.5 V (vs. NHE).[151] While the specific adsorption of cations also promotes the C_{2+} formation, such as the adsorption of Cs^+ with a lower potential results in a higher C_{2+} production since it generates the strongest surface dipole moment.

More recently, Singh et al. demonstrated that changes in local pH with different AM^+ are related to cation hydrolysis near the cathode.[149] The study revealed that the water molecule on solvated cations dissociates and releases H^+ when the cation approaches the cathode, driven by the electrostatic interaction between the electrode surface charge and the cation. Hydrolysis allows the solvated cation to act as a pH buffer, offsetting the polarization losses associated with the increased pH. As shown in **Table 3.1.1**, the effect strongly depends on the cation size, since the pK_a for cation hydrolysis near the cathode surface decreases with increasing cation size. Due to the electrostatic interaction between the solvated cation and the cathode surface increasing with the size increase, the buffering ability of cations increases in the order $Li^+ > Na^+ > K^+ > Rb^+ >$

Cs^+. Experimental measurements confirmed that the decrease in polarization loss due to stronger buffering ability benefits the selectivity of C_2 products (**Figure 3.1.1**), in which the C_2H_2/CH_4 FE (%) ratio significantly increased for the larger K^+, Rb^+ and Cs^+ cations.

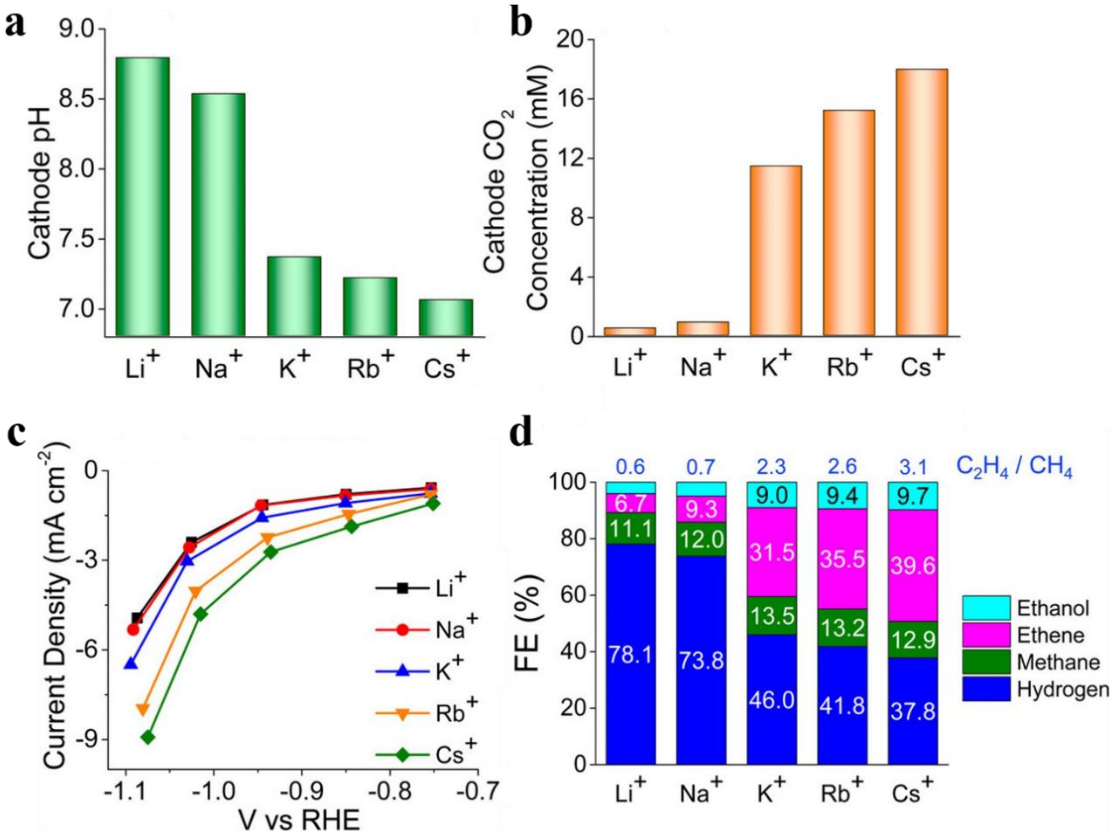

Figure 3.1.1 (a) Calculated pH value on Cu electrode. (b) Calculated CO_2 concentration on Cu electrode. (c) Current density as a function of applied potential on a Cu electrode. (d) FEs for ethanol, ethene, methane, and hydrogen generated on a Cu electrode at −1 V versus the reversible hydrogen electrode (RHE) in CO_2-saturated 0.1 M $MHCO_3$ electrolyte, where M represents Li, Na, K, Rb, or Cs.[149]

Cation-induced interfacial electric field tuning can also explain the trend in cation size and CO_2RR activity, as well as C_2 product selectivity.[152] Compared to the pH, which significantly impacts both HER and CO_2RR, the electric field effect does not affect the intermediate without a dipole moment (H* intermediate). However, the induced electric field will strongly affect the CO_2RR intermediates (e.g., intermediates with a C=O bond: *CO_2, *CO, *OCCO, and *OCCHO) due to their considerable dipole moment and polarizability, as shown in **Table 3.1.2**. For example, the local cation-induced electric field can promote the CO_2-to-CO reduction by stabilizing the adsorbed *CO_2 on weakly adsorbing metals. Further DFT calculations revealed that the solvated AM^+ in the OHP generates a high electrostatic field of approximately -1.0 V/Å, leading to a field stabilization effect for various CO_2RR intermediates on the Cu surface (**Figure 3.1.2**).[153] In particular, the *OCCO intermediates with a larger dipole moment and polarizability could gain greater field stabilization than *CO, which promotes the formation of the initial C_2 intermediate.

Table 3.1.2 The dipole moment and polarizability of reaction intermediates on Cu(111) surface.[153]

Intermediates	**Dipole moment (eÅ)**	**Polarizability (eÅ^2/V)**
$*CO_2$	0.76	0.40
$*COOH$	−0.19	0.60
$*OCHO$	0.04	0.42
$*CO$	0.23	0.22
$*CHO$	0.00	0.36
$*OCCO$	0.66	0.54
$*OCCHO$	0.75	0.74
$*CHOH$	−0.05	0.52
$*CH$	−0.02	0.18
$*CH_2$	−0.08	0.26
$*CH_3$	−0.03	0.44
$*OH$	−0.26	0.14
$*H$	0.00	0.00

However, the variation in cation size did not significantly change the electric field in the vicinity of the adsorbate. It is believed that the cationic size specificity on promoting C_2 product formation ($Li^+ < Na^+ < K^+ < Rb^+ < Cs^+$) originates from the cation concentration at the OHP increases with increasing cation size, in which the larger cations (K^+ and Cs^+) are more energetically favoured at the OHP than the smaller cations (Li^+ and Na^+). Further study has supported this hypothesis using DFT calculations combined with a continuum surface-charge model based on a modified Poisson–Boltzmann approach.[154] It revealed the electrolyte distribution and showed that the repulsive interaction between solvated cations reduces the cation concentration at the OHP, thereby lowering the surface charge density and the local electric field. This model illustrated that the larger AM$^+$ (lower solvation energy) concentrates more at the OHP due to the smaller solvated AM$^+$ and weaker repulsive interaction.

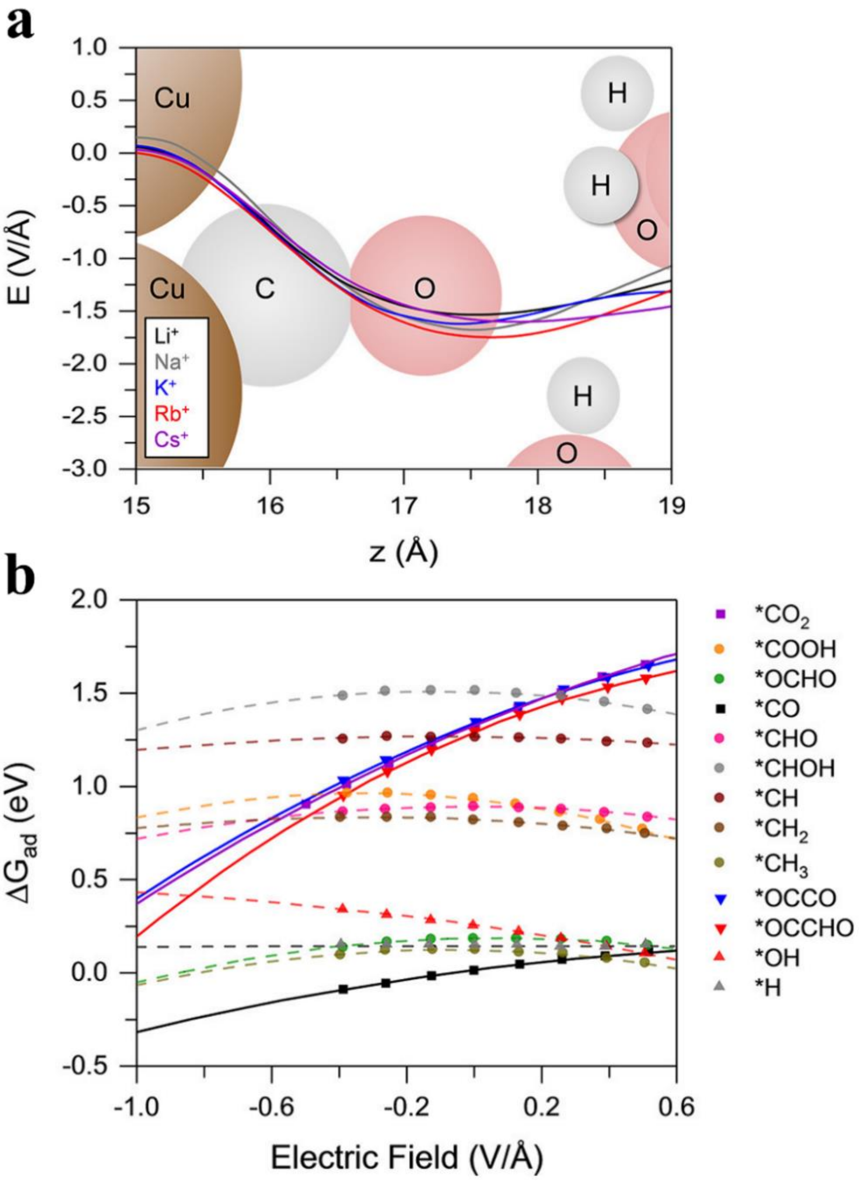

Figure 3.1.2 (a) Electric field variation near the surface of the Cu(111) with adsorbed

*CO intermediate plotted as a function of the z-coordinate. (b) Field effects on various CO_2RR intermediates on Cu(111) surface.[153]

Recent studies have also demonstrated that electrostatic interactions between the cation and intermediates affect CO_2RR activity. Qin et al. demonstrated that short-range electrostatic interactions between intermediates and cation species facilitate inner-sphere CO_2 activation and electron transfer, thereby stabilizing the initial *CO_2 intermediate and enhancing CO_2RR activity.[155] Similar to CO_2, C_2 intermediates (e.g *OCCO) can also be stabilized by the coordination of cation species, which can promote C_2 product formation by enhancing the C–C coupling. For instance, MD simulations have revealed that the larger AM^+ can desolvate earlier and closer to the interface, allowing it to directly coordinate with the adsorbed intermediate and partially replace the hydrogen-bond stabilization provided by water molecules, thereby exerting a greater promoting effect on C_2 product formation. The study also found that the local hydrophobic microenvironment created by larger cations prevents the formation of *COH, which may favor CO dimerization.

The coupling between C_1 intermediates is typically regarded as the critical step leading to the C_2 pathway on the metal surface. Studies have shown that CO dimerization is the rate-determining step for the C_2 pathways. In particular, the effect of AM^+ on the CO_2RR process has been intensively studied, including its promotion of C–C coupling in C_2 pathways. The current theoretical investigation of cation effects primarily relies on MD simulations, which show that solvated cations in the OHP alter local pH and surface charge density, thereby boosting C–C coupling. Meanwhile, the short-range interaction between the solvated cation and the reaction intermediates has also been studied recently, revealing that larger cations are more likely to coordinate with surface intermediates, thereby facilitating their formation. However, these studies primarily emphasize the solvation effects induced by water molecules, and the intrinsic effects caused by the cation have not been discussed.

Based on this, we have conducted a DFT investigation of the direct cation effect on the NM surfaces during CO dimerization. Our work revealed, from a thermodynamic perspective, the stabilization effects induced by AM^+ (Li^+, Na^+, K^+, and Cs^+) and suggested that the intrinsic effects of cations may differ due to solvation considerations, as indicated by the correlation between the direct stabilization energy and the energy of the CO dimerization reaction. Moreover, further investigation demonstrated electronic modification of AM^+, which explains the origin of the cation stabilization and promotes the CO dimerization process. We believe this work can provide a significant theoretical reference for the cation effect in CO_2RR and facilitate improvements in C_2 selectivity in future research.

3.2 Computational Details

This work performed all DFT calculations using the Cambridge Serial Total Energy Package (CASTEP) implemented in BIOVIA Materials Studio.[156] The exchange-correlation energy is described by the Generalized Gradient Approximation, along with the Perdew–Burke–Ernzerhof (GGA-PBE) exchange-correlation functional, for all model calculations.[137-138] The ultrasoft pseudopotential approximation was used to describe the interaction between the ion cores and the valence electrons. At the same time, the Broyden–Fletcher–Goldfarb–Shanno (BFGS) algorithm was adopted as the optimizer for the geometry optimization.[157-158] The plane-wave cutoff energies for the Pt(100) and Cu(100) adsorption models were set as 380 eV and 440 eV, respectively. The k-point grid parameter was set with coarse quality. The convergence criteria for the single point energy calculation and geometry optimizations were selected as follows: SCF tolerance is 1.0×10^{-5} eV/atom, the Hellmann-Feynman force per atom is 0.1 eV/Å; the Max. Stress is 0.2 GPa, and the Max. Displacement is 0.005 Å.

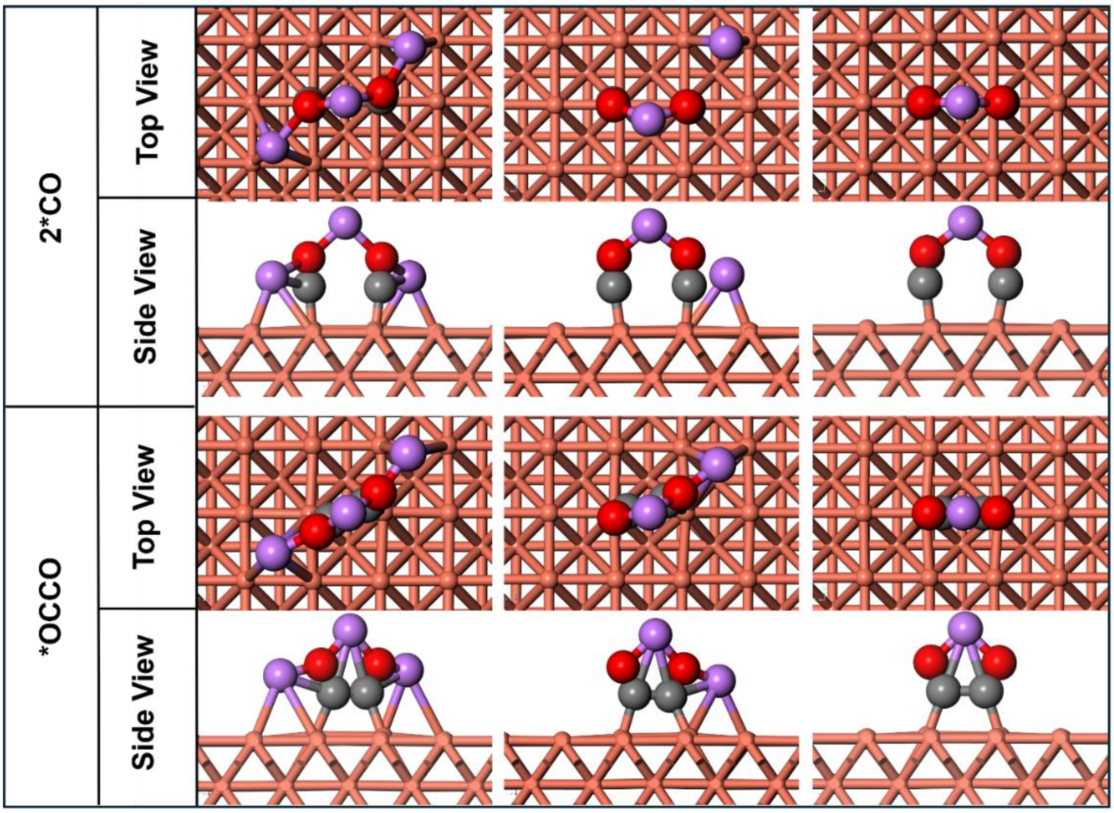

Figure 3.2.1 Adsorption configuration of *OCCO and 2*CO on Cu(100) surface with cations. The black spheres are C atoms, the red spheres are O atoms, and the light purple spheres are cations.

The Pt(100) and Cu(100) metal slabs with a 4 × 4 supercell and five atomic layers were used to simulate the adsorption of *CO and *OCCO. The thickness of the vacuum along the z-axis, perpendicular to the metal surface, was set to 20 Å to prevent spurious interactions between the repeated slabs. The top sites (T-sites) on metal surfaces were selected as adsorption sites for *CO, and the CO dimerization of two adsorbed *CO molecules occurs at the bridge site between two neighboring T-sites. The AM^+ coordinate with the 2*CO and *OCCO intermediate range from one (+1) to three (+3), as shown in **Figures 3.2.1** and **3.2.2**.

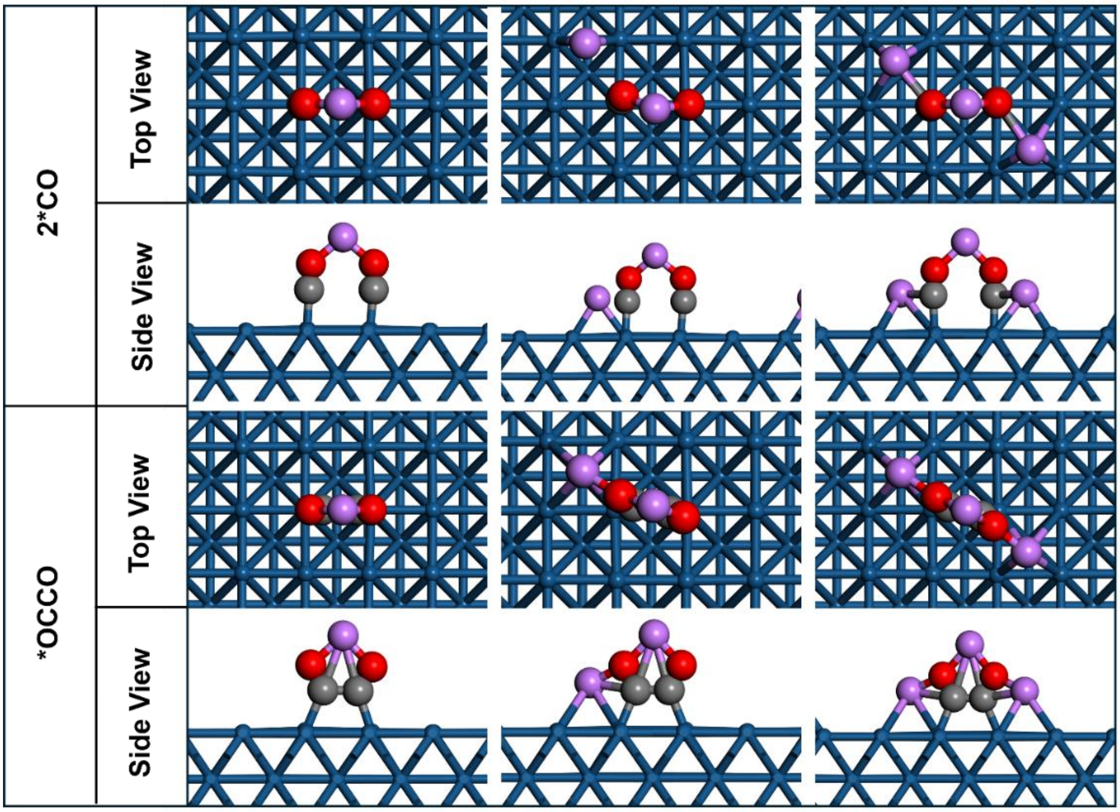

Figure 3.2.2 Adsorption configuration of *OCCO and 2*CO on the Pt(100) surface with cations. The black spheres are C atoms, the red spheres are O atoms, and the light

purple spheres are cations.

The adsorption energy (ΔE_{ads}) of the *CO and *OCCO is defined as:

$$\Delta E_{ads} = E_{\mathrm{slab+intermediate}} - E_{\mathrm{slab}} - E_{\mathrm{intermediate}}$$

Where the $E_{\mathrm{slab+intermediate}}$ is the total energy of the metal slab binding with *CO and *OCCO intermediates. The E_{slab} and $E_{\mathrm{intermediate}}$ are the energy of the metal slab and isolated intermediates, respectively. The total stabilization effects induced by cation-intermediate interaction were defined as the cation-stabilization energy (ΔE_{stab}):

$$\Delta E_{\mathrm{interaction}} = E_{\mathrm{system}} - (E_{\mathrm{slab}} + E_{\mathrm{OCCO}} + E_{AM+})$$

$$\Delta E_{\mathrm{stab}} = \Delta E_{\mathrm{interaction}} - \Delta E_{\mathrm{OCCO}}$$

$$\Delta E_{\mathrm{stab}} = \Delta E_{\mathrm{AM+-slab}} + \Delta E_{\mathrm{AM+-dimer}}$$

The $\Delta E_{\mathrm{AM+-slab}}$, $\Delta E_{\mathrm{AM+-dimer}}$ and $E_{\mathrm{AM+}}$ are the cation-slab interaction energy, cation-dimer stabilization energy, and cation species energy, respectively.

3.3 Geometry Data of the Adsorption Models

Previous DFT studies predicted that CO adsorption on the Cu(100) surface under vacuum conditions is preferred on the top site.[159] On the other hand, the bridge sites are predicted to be the most favourable sites for the adsorption of CO on the Pt(100) surface. However, the difference in adsorption strength between the second-favourite site and the favourite site is only 0.05 eV.[160] To compare Cu(100) and Pt(100) surfaces, the nearby top sites have been selected for the 2*CO adsorption, and the CO dimerization occurs at the bridge sites between the two neighbouring top sites with *CO adsorption. The neutral singlet OCCO (ethylenedione) molecule in the gas phase is unstable with respect to dissociation into two individual CO molecules.[161-162] The *OCCO intermediate can bind on the metal surface via two C atoms (C–C binding mode) or one side of the O–C placed parallel to the surface, while another side of the molecule lifts from the surface (O–C binding mode). The C–C binding mode is more commonly reported in the study of CO dimerization, but this *OCCO configuration dissociates into 2 *CO spontaneously on the Cu surface without any water. Meanwhile, the higher energy O–C binding of *OCCO is more stable under both vacuum and solvation conditions.[163-164] Through DFT calculations, we confirmed the previous conclusion that the only *OCCO with O–C binding form on Cu(100) surface under vacuum conditions, while *OCCO with both C–C and O–C binding can form on Pt(100) surface. We also showed that cation species can significantly stabilize the *OCCO with C–C binding on the Cu surface via cation-intermediate interactions. Herein, we employed the more commonly reported C–C binding mode with various AM^+ for further calculation and discussion.

Table 3.3.1 The bond length of the *OCCO under different AM^+ and the corresponding adsorption energy.

Surface	**AM^+**	**$d_{C–C}$ (Å)**	**$d_{C–O}$ (Å)**	**$d_{C–M}$ (Å)**	**ΔE_{OCCO} (eV)**	**ΔE_{2CO} (eV)**	**ΔE_{AM+} (eV)**
Cu(100)	Li^+	1.482	1.300	1.928	–0.87	–1.43	–7.19
	Na^+	1.562	1.261	1.935	–1.24	–1.57	–6.86
	K^+	1.571	1.257	1.945	–1.31	–1.58	–6.38
	Cs^+	1.610	1.242	1.946	–1.43	–1.59	–6.11

Pt(100)	Li^+	1.519	1.266	1.964	–2.97	–3.23	–1.39
	Na^+	1.539	1.254	1.967	–3.06	–3.33	–0.88
	K^+	1.557	1.243	1.976	–3.16	–3.34	–0.47
	Cs^+	1.573	1.238	1.975	–3.18	–3.24	–0.20

The *OCCO intermediate on Cu(100) and Pt(100) surfaces showed varying C–C (d_{C-C}), C–O (d_{C-O}), and C–M (d_{C-M}) bond lengths with the coordination of different alkali cation species. When varying the cations, a noticeable variation in the adsorption energy is observed on the Cu and Pt surfaces. **Table 3.3.1** summarizes the geometry information and adsorption energies of *OCCO (ΔE_{OCCO}), 2*CO (ΔE_{2CO}) and cations (ΔE_{AM+}) on the Cu(100) and Pt(100) surfaces. The calculations of the adsorption energy are shown in Section 3.2: Computational details. The ΔE_{OCCO}, ΔE_{2CO} and ΔE_{AM+} determined the binding strengths of *OCCO, 2*CO and cations on the Cu and Pt surfaces, respectively. With the coordination of cations (AM^+), the ΔE_{OCCO} and ΔE_{2CO} is defined by the reaction energy of the following equation:

$$*AM^+ + OCCO/2CO \rightarrow [*OCCO/*2CO \cdot AM^+]^+$$

Accordingly, a more negative value of ΔE_{OCCO} and ΔE_{2CO} means a stronger binding strength on the Cu and Pt surfaces. We observed that the change of the cation from Cs^+ to Li^+ (decreasing in cation size: Cs^+ 167 pm, Li^+ 90 pm) significantly shortened d_{C-C} on the *OCCO on the Cu(100) surface, in which the d_{C-C} decreased from 1.610 to 1.482 Å. The bond length variation suggests a strong C–C bonding form during CO dimerization, with the coordination of smaller AM^+ cations, such as Li^+ and Na^+. In contrast, the d_{C-C} of *OCCO on the Pt(100) surface was less affected by the variation of AM^+, as the d_{C-C} decreased from 1.573 to 1.519 Å when changing the cation from

Cs^+ to Li^+. The formation of *OCCO on Cu and Pt surfaces is accompanied by C–O bond stretching due to the intramolecular repulsion between the lone pair electrons on the O atom. Compared with two individual *CO molecules adsorbed on the T sites with $d_{C–O}$ of 1.170 Å, the formation of *OCCO on the Cu(100) surface resulted in an elongated $d_{C–O}$ ranging from 1.242 to 1.300 Å with different coordinated cations. The $d_{C–O}$ elongation of *OCCO was also observed on the Pt(100) surface with a similar trend. It should be noticed that the elongation of the C–O bond helps stabilize the *OCCO intermediate by reducing the lone pair electron repulsion of the O atoms. The exothermic C–C bond formation serves as the thermodynamic driving force for the CO dimerization, in which the released energy is primarily used to compensate for the C–O bond elongation; hence, the shorter the C–C bond, the more C–O bond elongation occurs.

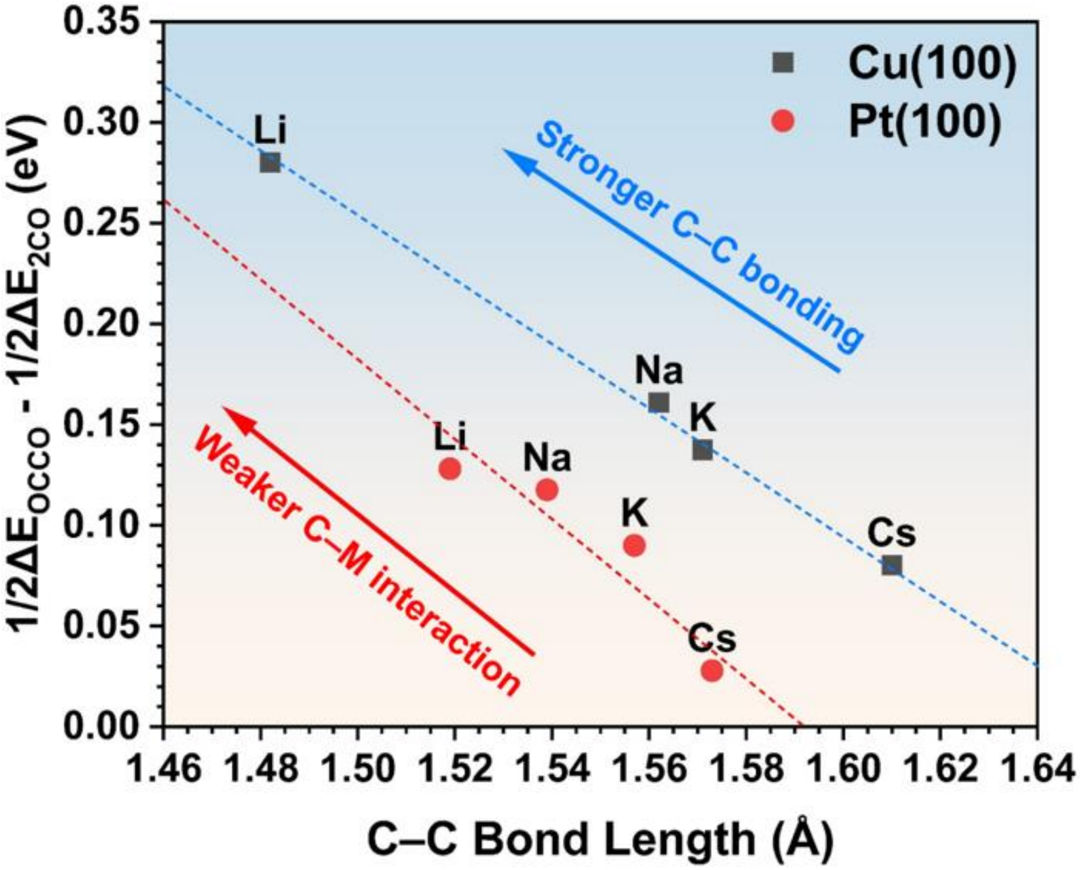

Figure 3.3.1 The change of the adsorption energy difference between *OCCO and *CO on Cu(100) and Pt(100) against the C–C bond length variation of the formed *OCCO.

Although the values of $d_{C–M}$ are similar, the adsorption strength of *OCCO and 2*CO on Pt(100) is much stronger than that on Cu(100). The overbinding of the intermediates may contribute to the poor performance of the CO_2RR on the Pt surface.[165-166] The adsorption energy also showed that the larger AM^+ strengthened the adsorption of *CO and *OCCO on Cu(100) and Pt(100) surfaces, which the ΔE_{OCCO} downshifted from −0.87 to −1.43 eV (ΔE_{2CO}: −1.43 to −1.59 eV) and −2.97 to −3.18 eV (ΔE_{2CO}: −3.23 to −3.24 eV) when changing the cation from Li^+ to Cs^+ on Cu(100) and Pt(100) surfaces, respectively. We noted that the change in adsorption energy on the Pt surface was relatively minor compared to that on the Cu surface, indicating that the strong adsorption of intermediates on the Pt surface was less affected by surrounding cations. In addition, the variation of adsorption energies of the initial 2*CO and final *OCCO ($1/2\Delta E_{OCCO} - 1/2\Delta E_{2CO}$) was positive, indicating the weakening of the C–M interaction after the formation of the C–C bond on Cu(100) and Pt(100) surfaces. Moreover, the weakening of the C–M interaction correlated with the C–C bond length of the *OCCO intermediate, in which the stronger C–C bonding (shorter the C–C bond length) showed more weakening of the C–M interaction (**Figure 3.3.1**). We believed that the weakening of the C–M interaction is attributed to the shifting (redistribution) of electron density from the C–M to C–C bond in CO dimerization, where the shifting of electron density was easier on the Cu(100) surface with smaller cations. The alkali cations display strong binding on the Cu(100) surface ΔE_{AM+} < –6.00 eV, especially the smaller cations (Li^+ and Na^+) have stronger binding than the larger cations (K^+ and Cs^+). In contrast, the Pt(100) surface adsorbs cations much more weakly than the Cu(100) surface, suggesting that the cation effects induced via specific cation adsorption were more likely on the Cu surface than the Pt surface.[167] Previous studies have demonstrated that cation adsorption on the Cu(100) surface can also induce a steric effect during electrochemical processes, thereby facilitating CO dimerization on Cu-based materials.[168] Overall, the adsorption behaviour revealed the impacts of cation coordination on the bonding of the intermediates. At the same time, further thermodynamic and electronic investigations were conducted to fully elucidate the role of direct cation effects on the CO dimerization process.

3.4 Energy Profile of CO Dimerization

To fully reveal the effects of AM^+ coordination toward the thermodynamic feasibility of CO dimerization, the reaction energy of *OCCO formation (ΔH_{OCCO}) have been determined by using DFT calculations. The ΔH_{OCCO} defined as the energy difference between the dimerization final state (FS) *OCCO and the initial state (IS) 2*CO on the Cu and Pt surfaces. It is believed that the ΔH_{OCCO} is related to the geometry of the final adsorbed *OCCO due to the variation of cation-*OCCO coordination, in which the significant differences in the $d_{C–C}$ and $d_{C–C}$ of the adsorbed *OCCO defined the most stable *OCCO on the Cu(100) and Pt(100) surfaces after the dimerization of 2*CO. As shown in **Figure 3.4.1**, DFT calculations demonstrated that the formation of the *OCCO was highly unfavourable on Cu(100) and Pt(100) surfaces without the coordination of cation species. It should also be noted that the final state *OCCO on the Cu(100) surface adopted the high energy state C–O bonding configuration with ΔH_{OCCO} of 0.71 eV, which differs from the C–C bonding configuration on the Pt(100) surface. It is believed that strong intermediate adsorption on the Pt(100) surface stabilizes the *OCCO with C–C bonding under vacuum, but the formation of *OCCO on Pt(100) displayed a high ΔH_{OCCO} of 1.04 eV due to the over-binding.

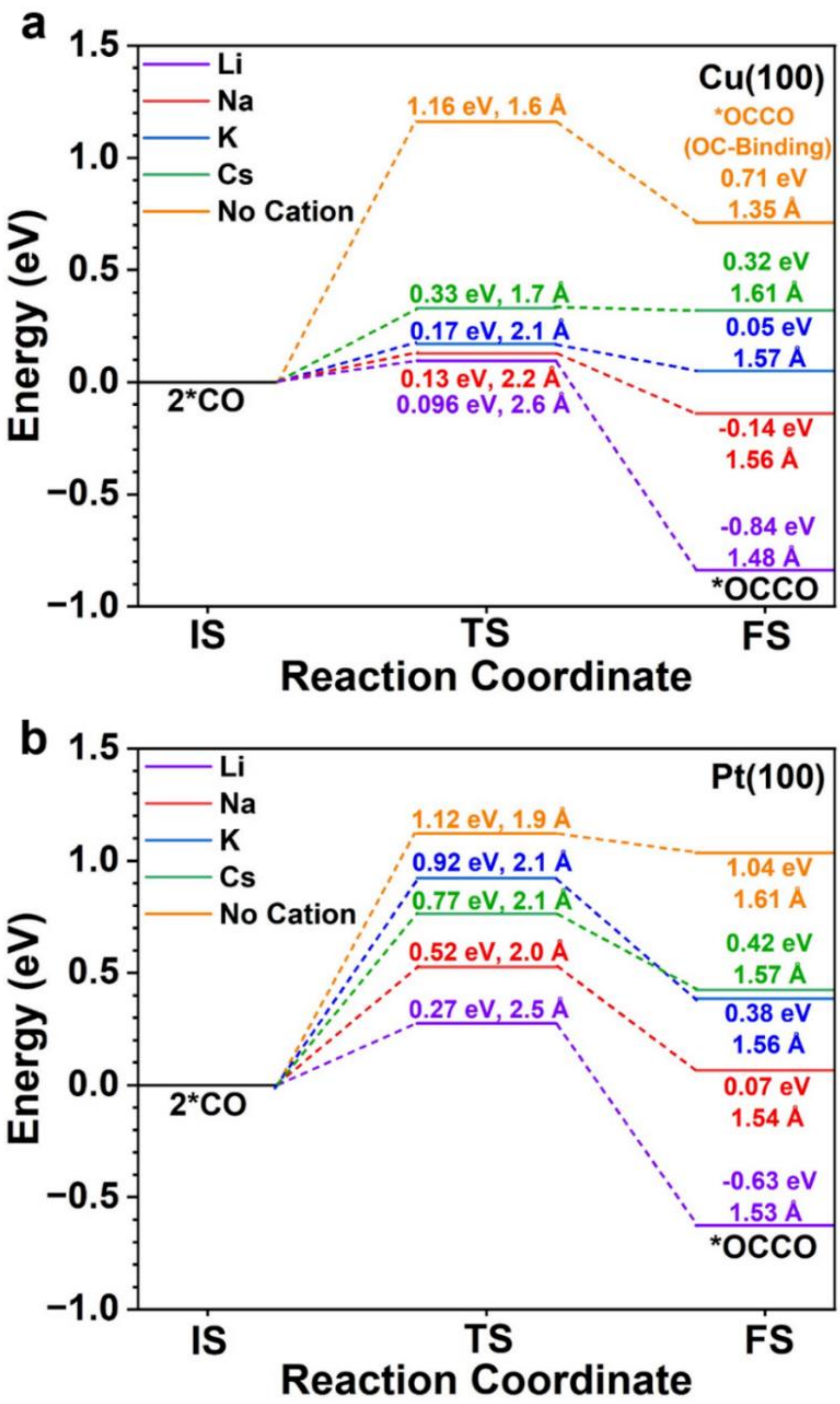

Figure 3.4.1 The reaction energy diagram of reaction paths for the CO dimerization on (a) Cu(100) surface and (b) Pt(100) surface. The energies and bond length shown above the transition state (TS) represent the energy barrier and the corresponding d_{C-C} distance at the TS. The energies and bond length shown on the final state (FS) are the reaction

energy for *OCCO formation and the corresponding $d_{C–C}$ at FS.

For the CO dimerization on the Cu and Pt surfaces under the AM^+ coordination, the DFT calculation results demonstrated an overall trend of $Li^+ < Na^+ < K^+ < Cs^+$ for the ΔH_{OCCO} on Cu(100) and Pt(100) surfaces, suggesting the dimerization process is more thermodynamically favourable with the coordination of smaller AM^+. As discussed in the previous chapter, the size of the cation has played a crucial role in the CO_2RR. Experimental and MD simulation results have demonstrated that larger cations can more effectively promote the CO_2RR and the formation of C_2 products. This may be attributed to the solvation environment of the cation species perturbing the direct cation-intermediate coordination during the CO_2RR process. Nevertheless, calculation results demonstrated that the size of the cation influences the ΔH_{OCCO} on both Cu and Pt surfaces, the smaller AM^+ can potentially facilitate the *OCCO formation without the kinetic interruption of the water solvation.

Moreover, the calculations predicted that forming *OCCO intermediate on the Pt(100) surface is less thermodynamically feasible than on the Cu(100) surface, even with AM^+ coordination. On the Pt(100) surface, the endergonic ΔH_{OCCO} of 0.07, 0.38, and 0.42 eV for Na^+, K^+, and Cs^+ cations suggested that the CO dimerization will not easily take place on the surface, while the exergonic ΔH_{OCCO} of −0.63 eV during Li^+ coordination implied that dimerization becomes spontaneous. For the Cu(100) surface, although the overall trend of the ΔH_{OCCO} not change, the ΔH_{OCCO} were lower than those on the Pt(100) surface with the same cation. The calculated ΔH_{OCCO} of CO dimerization under Li^+, Na^+, $K^{+,}$ and Cs^+ were −0.84 eV, −0.14 eV, 0.05 eV, and 0.32 eV, respectively. In particular, both Li^+ and Na^+ displayed negative ΔH_{OCCO} of -0.84 eV and -0.14 eV on the Cu(100) surface, respectively, indicating that the C–C bond formation between two *CO was more favourable due to the exergonic ΔH_{OCCO}. For the larger cation species, although the Cs^+ has an endergonic CO dimerization process with ΔH_{OCCO} of 0.32 eV, the K^+ displayed a near-zero ΔH_{OCCO} of 0.05 eV. These results also suggested that the *OCCO formation was more thermodynamically favourable on the Cu(100), especially with the introduction of direct cation stabilization of the *OCCO.

On the other hand, the energy barriers of the CO dimerization with different AM^+ were also determined. Our work defined the TS as the configuration (C–C distance) with the highest energy state during the dimerization. After obtaining the optimized IS (2*CO) and the FS (*OCCO) via geometry optimization, the reaction profiles and TS configuration of dimerization can be determined by applying a constrained geometry optimization (fixing the C–C distance between the two adsorbed *CO). By manually changing the C–C distance during constrained geometry optimization, we can force the dimerization process and probe the TS configurations with their energy.

In addition, the TS configuration of the dimerization showed a similar trend, with the coordination of smaller AM^+ resulting in a lower energy barrier for the *OCCO formation on both Cu(100) and Pt(100) surfaces. For the Cu(100) surfaces, the absence of cations leads to a high barrier of 1.16 eV for the formation *OCCO with O–C binding mode, suggesting that moving 2*CO toward each other is relatively difficult. However, the energy barrier is significantly reduced to 0.33 eV with the coordination of Cs^+, followed by 0.17 eV and 0.13 eV for the K^+ and Na^+ coordination. Notably, the coordination of the smallest Li^+ cation can effectively promote *OCCO formation, with the lowest energy barrier of 0.0096 eV for the 2*CO movement via direct cation-intermediate interactions. In contrast, the Pt(100) surface displayed significantly higher energy barriers for the C–C coupling. Without AM^+, the Pt(100) surface displays a 1.12 eV energy barrier for the formation of *OCCO intermediate. Under the coordination cations, the energy barrier of *OCCO formation on the Pt surface followed the trend $Li^+ < Na^+ < Cs^+ < K^+$ with barriers of 0.27, 0.52, 0.77, and 0.92 eV, respectively. Instead of the largest Cs^+, the coordination of K^+ has the highest barrier for 2*CO movement owing to the similar TS configuration.

We also found that the reaction energy profile for CO dimerization shows an interesting correlation with the intermediate configuration ($d_{C–C}$). The calculation results showed that the CO dimerization with lower ΔH_{OCCO} and energy barrier has a longer $d_{C–C}$ on their TS. It is believed that the TS resembles the structure of the nearest stable species, in which the CO dimerization with exergonic ΔH_{OCCO} has a longer $d_{C–C}$ on TS due to the reactant-like TS. Whereas the CO dimerization with endergonic ΔH_{OCCO} has a product-like TS (shorter $d_{C–C}$ on TS). Therefore, we believe that stabilizing the FS due to cation-*OCCO coordination thermodynamically drives *OCCO formation and reduces the 2*CO movement barrier on Cu and Pt metal surfaces.

3.5 Direct Stabilization Effect of Cation

To further investigate the role of the AM^+ in promoting CO dimerization, the stabilization effects of the CO dimerization on metal surfaces have been determined.

As shown in **Figure 3.5.1**, the ΔE_{OCCO} adsorption energy can indicate the stability of *OCCO adsorption, and we found that the ΔE_{OCCO} display a linear relationship with the ΔH_{OCCO} on Cu and Pt surfaces individually. It is believed that the difference in cation-surface and *OCCO-surface interactions on Cu and Pt surfaces leads to limited correlation, in which the different surface electronic properties of Cu and Pt surfaces contribute to the considerable difference in the ΔE_{OCCO} on the metal surfaces. In other words, the ΔE_{OCCO} indicated that the overall stabilization was affected by both cations and metal surfaces.

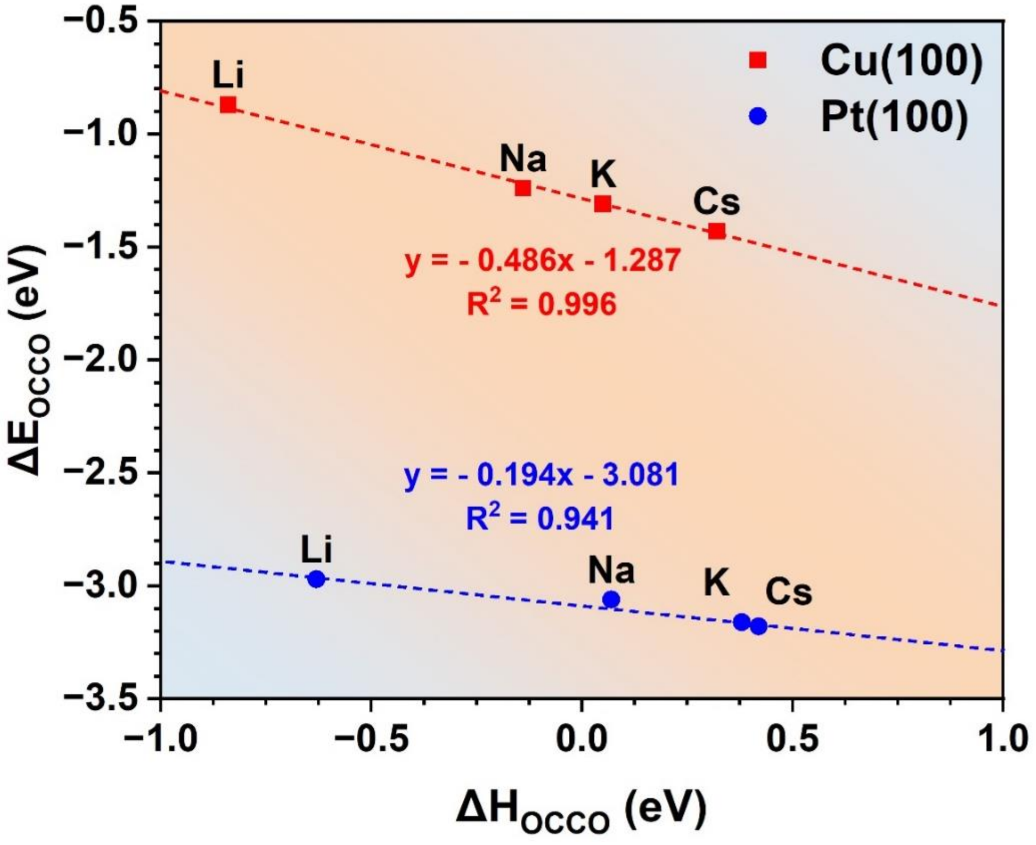

Figure 3.5.1 The linear correlation between the ΔE_{OCCO} adsorption energy and $\Delta \mathrm{H}_{\mathrm{OCCO}}$ on Cu(100) and Pt(100) surfaces.

To evaluate the overall stabilization effect induced by the AM^+ on Cu(100) and Pt(100) surfaces, the cation stabilization energy (ΔE_{stab}) was determined. The ΔE_{stab} is the summation of the direct cation stabilization ($\Delta E_{cation-dimer}$) and surface-induced stabilization ($\Delta E_{cation-surface}$), in which a more negative value indicates the better stabilization of *OCCO intermediate. As shown in **Figure 3.5.2a, b**, the ΔE_{stab} vary with the change of AM^+ and the relative ratio of the cation (AM^+: *OCCO) on the metal surfaces. On both Cu and Pt surfaces, the overall stabilization effects were weakening with the increase of cation size ($Li^+ > Na^+ > K^+ > Cs^+$), while the higher relative ratio of the cation (+1, +2 and +3) also resulted in a larger stabilization with a more negative ΔE_{stab}. This indicated that cation stabilization is regulated by both the type of AM^+ and the relative ratio of cations. For instance, the Li^+ cation (3+) system on the Cu(100) surface has the most significant overall stabilization effect.

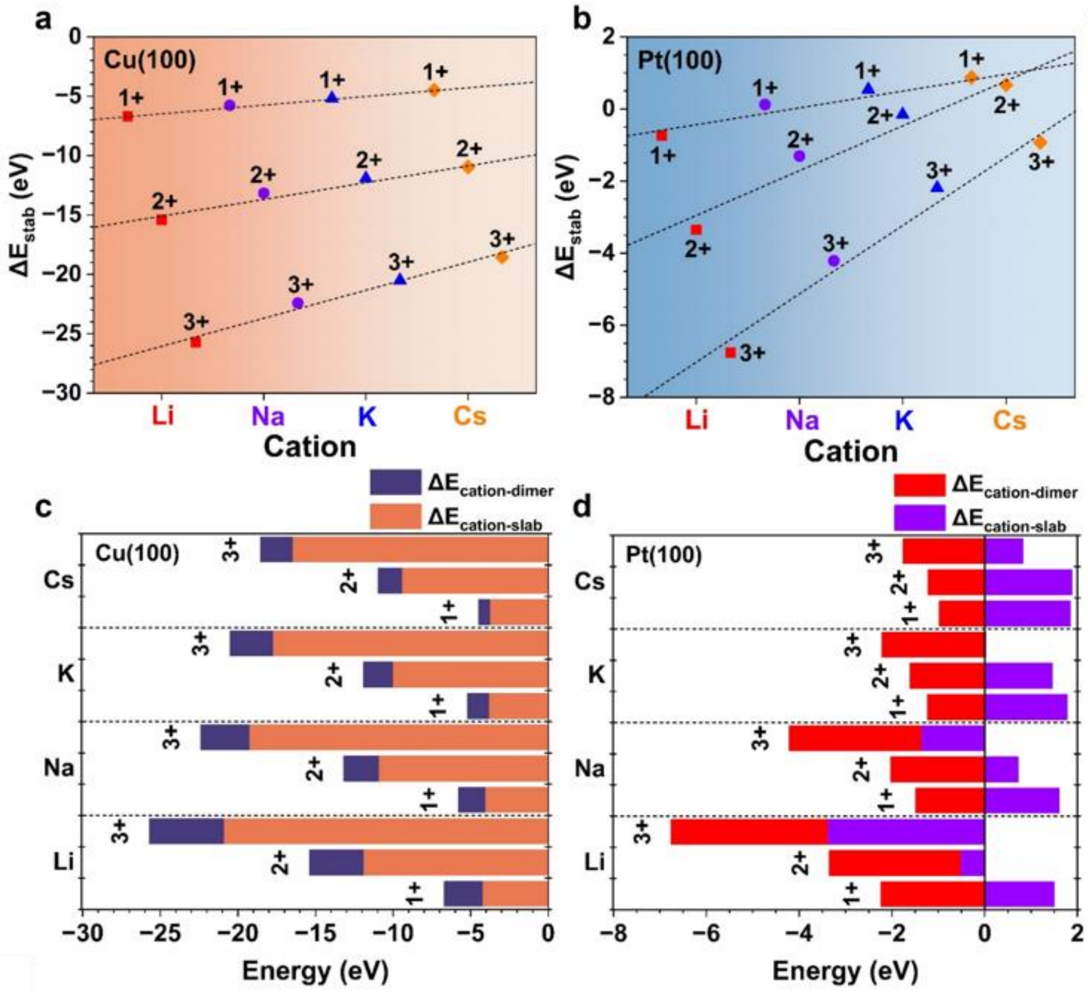

Figure 3.5.2 The calculated ΔE_{stab} for *OCCO formation for (a) Cu(100) surface and (b) Pt(100) surface with different alkali metal ions. The $\Delta E_{cation-dimer}$ and $\Delta E_{cation-slab}$ contributed to the ΔE_{stab} for (c) Cu(100) surface and (d) Pt(100) surface. The 1+, 2+, and 3+ represent relative ratios of one, two, and three cations per adsorbed *OCCO.

In contrast, the system on Pt(100) surface with Cs^+ has ΔE_{stab} close to zero, suggesting the weak overall stabilization of large cations on the Pt surface. The overall cation stabilization on the Cu(100) surface is larger than on the Pt(100) surface. **Figure 3.5.2c, d** shown that the less cation-induced stabilization on the Pt(100) surface is related to the mostly positive value of $\Delta E_{cation-surface}$. This indicated that the cation-surface interaction on Pt tends to weaken the overall stabilization effect. Differ from the Pt(100) surface, the Cu(100) has strongly negative $E_{cation-slab}$. Hence, the overall cation stabilization on the Cu(100) surface was mainly due to the strong cation-surface interaction. Intriguingly, it is worth noticing that the magnitude $\Delta E_{cation-dimer}$ displayed less surface dependency for Cu and Pt metal surfaces, which implied that the direct cation-*OCCO coordination was less affected by the electronic properties of the metal surfaces.

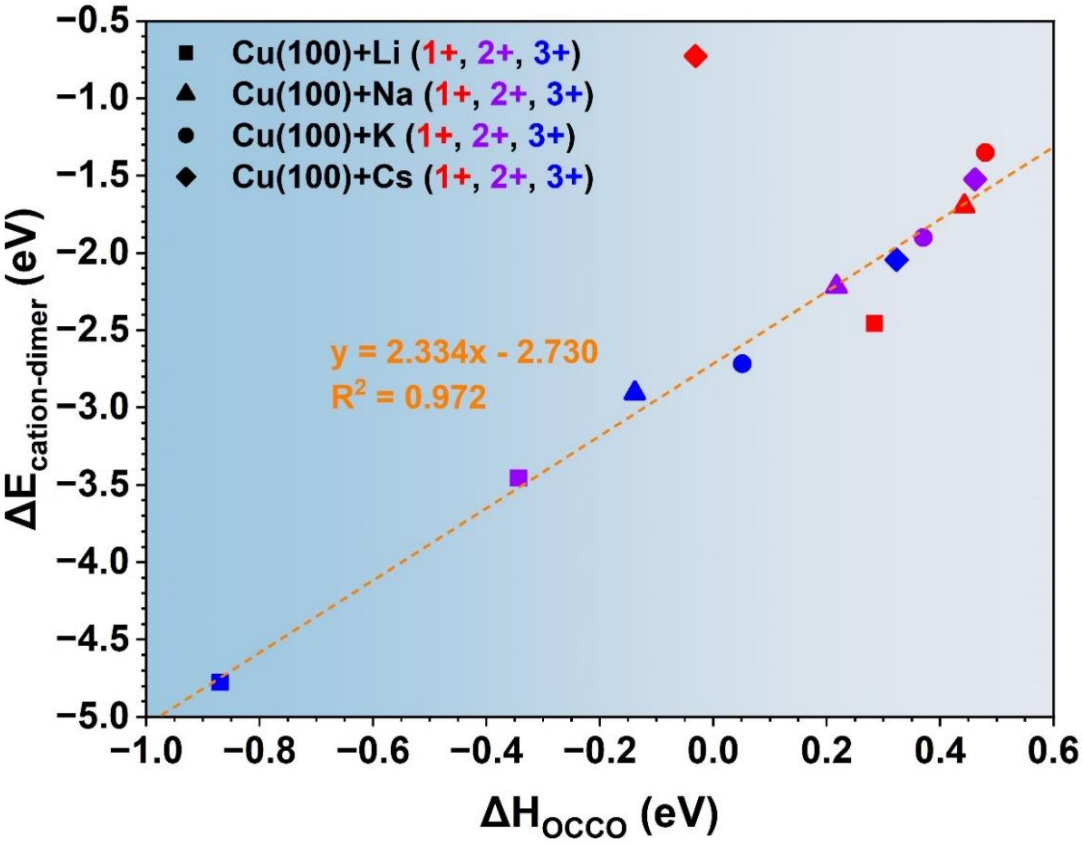

Figure 3.5.3 The individual linear correlation between the ΔH_{OCCO} and the $\Delta E_{cation-dimer}$ on Cu(100) surface with various alkali metal ion (Li^+, Na^+, K^+ and Cs^+) and different relative ratio of the cations (1+, 2+ and 3+).

On the other hand, the $\Delta E_{cation-dimer}$ displayed a linear correlation with the ΔH_{OCCO} on both Cu(100) and Pt(100) surfaces. In particular, the $\Delta E_{cation-dimer}$ showed a strong linear relationship with ΔH_{OCCO} on Cu(100)) surface with $R^2 = 0.972$ (**Figure 3.5.3)**. Meanwhile, the correlation between the reaction energy ΔH_{OCCO} and $\Delta E_{cation-dimer}$ is weaker on the Pt(100) surface ($R^2 = 0.797$), in which the variation of the AM^+ only leads to a slight change of the ΔH_{OCCO}, especially for the larger cation (**Figure 3.5.4**). This slight variation suggested that the CO dimerization on the Pt(100) surface was unsusceptible to the cation stabilization effects because of the over-binding of *CO and *OCCO intermediates. Both the *CO and *OCCO intermediates were stabilized owing to the strong intermediate-Pt interaction, which makes it hard to stabilize the *CO and *OCCO intermediates further, like on the Cu surface.

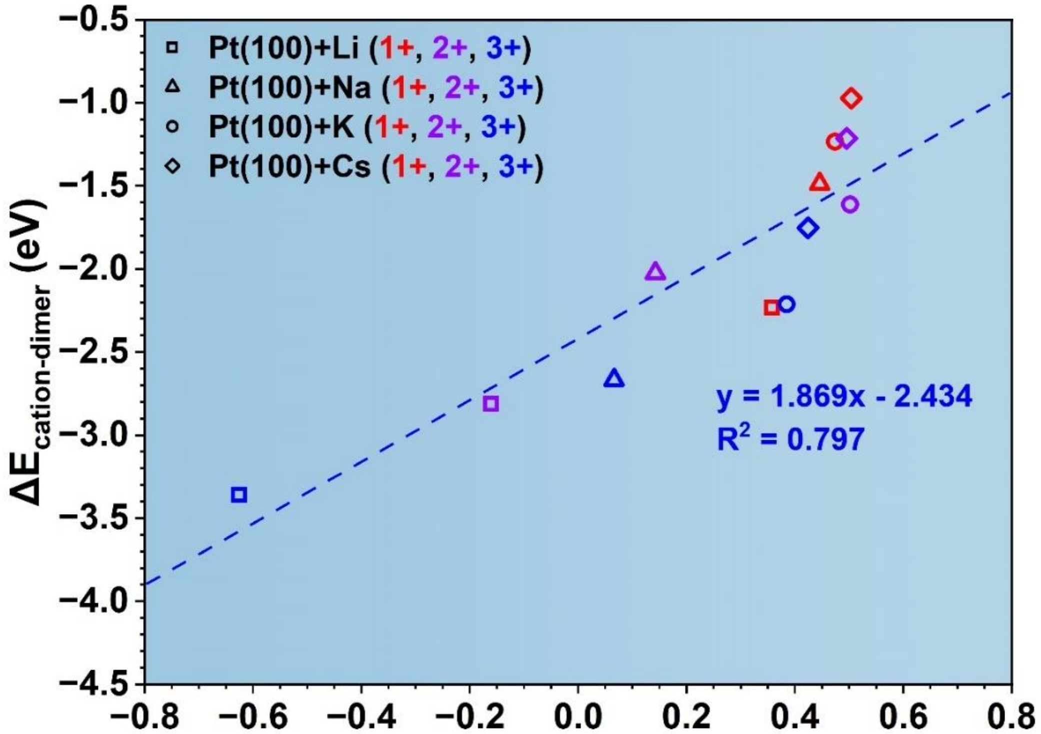

Figure 3.5.4 The individual linear correlation between the ΔH_{OCCO} and the $\Delta E_{cation-dimer}$ on Pt(100) surface with various alkali metal ion (Li^+, Na^+, K^+ and Cs^+) and different relative ratio of cations (1+, 2+ and 3+).

Although the correlation between the ΔH_{OCCO} and $\Delta E_{cation-dimer}$ much weaker on the Pt(100) surface, it still displays an overall strong linear correlation with $R^2 = 0.891$ on the Cu(100) and Pt(100) surfaces, as shown in **Figure 3.5.5**. However, an outlier data point was found at $\Delta E_{cation-dimer} = -0.7$ eV in the linear plot, which corresponds to the 1Cs^+ on Cu(100). In this 1Cs^+:1*OCCO coordination, there is no stable adsorption configuration for the final *OCCO intermediate because the weak stabilization of Cs^+ is insufficient to stabilize *OCCO on the Cu(100) surface. For the Pt(100) surface, the data points of $\Delta E_{cation-dimer}$ were concentrated in $\Delta H_{OCCO} > 0$ eV owing to the larger $\Delta E_{cation-dimer}$ value compared to on Cu(100) surface. Nevertheless, the overall linear relationship revealed that the direct interactions between the cation species and *OCCO have a significant role in determining the thermodynamic feasibility of CO dimerization on metal surfaces, in which the $\Delta E_{cation-dimer}$ can be considered as the descriptor of the CO dimerization process.

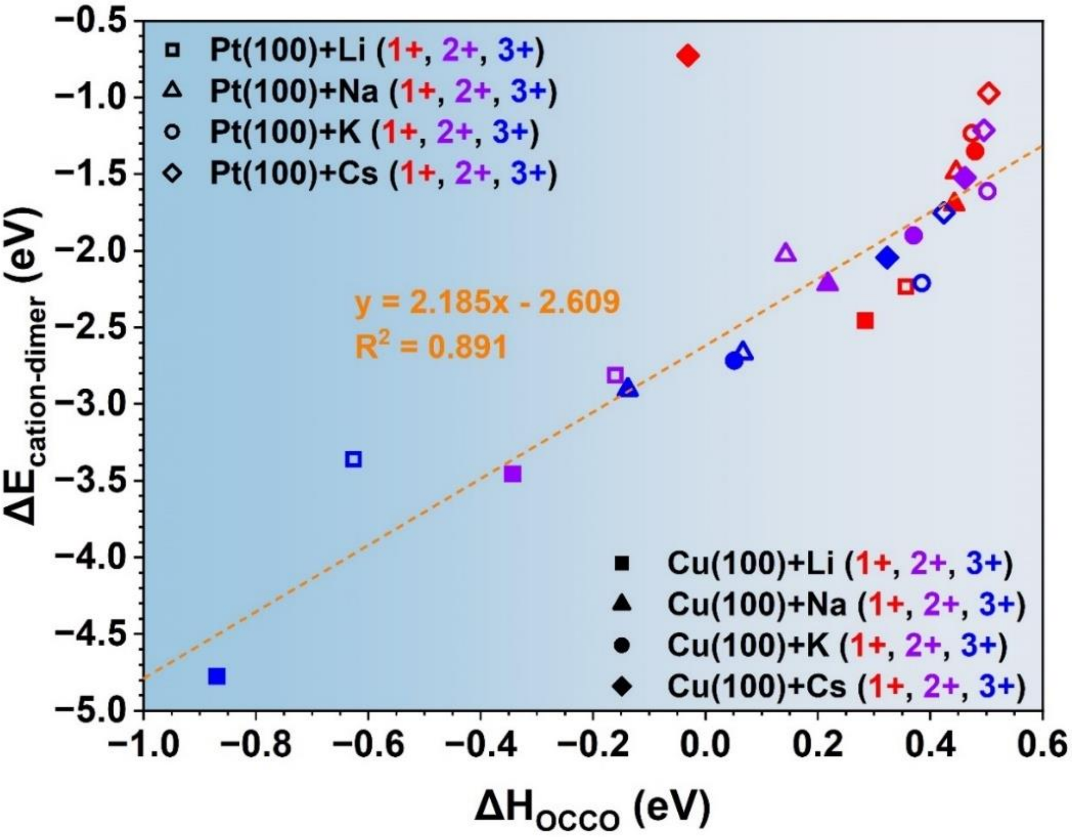

Figure 3.5.5 The linear correlation between the ΔH_{OCCO} and the $\Delta E_{cation-dimer}$ on Cu(100) and Pt(100) surface with various alkali metal ion (Li^+, Na^+, K^+ and Cs^+) and different relative ratio of cations (1+, 2+ and 3+).

3.6 Electronic Properties Analysis

Electronic properties analysis was performed to investigate the stabilization effects of AM^+. Previous studies demonstrated the electron transfer to the *OCCO from the metal surface upon CO dimerization, in which the reduced $*OCCO^-$ stabilized on the Cu surface by adopting a high-spin quartet-like geometry.[169-171] Herein, the Mulliken population analysis is used to investigate the charge distribution on the adsorbed *OCCO on metal surfaces under different AM^+.

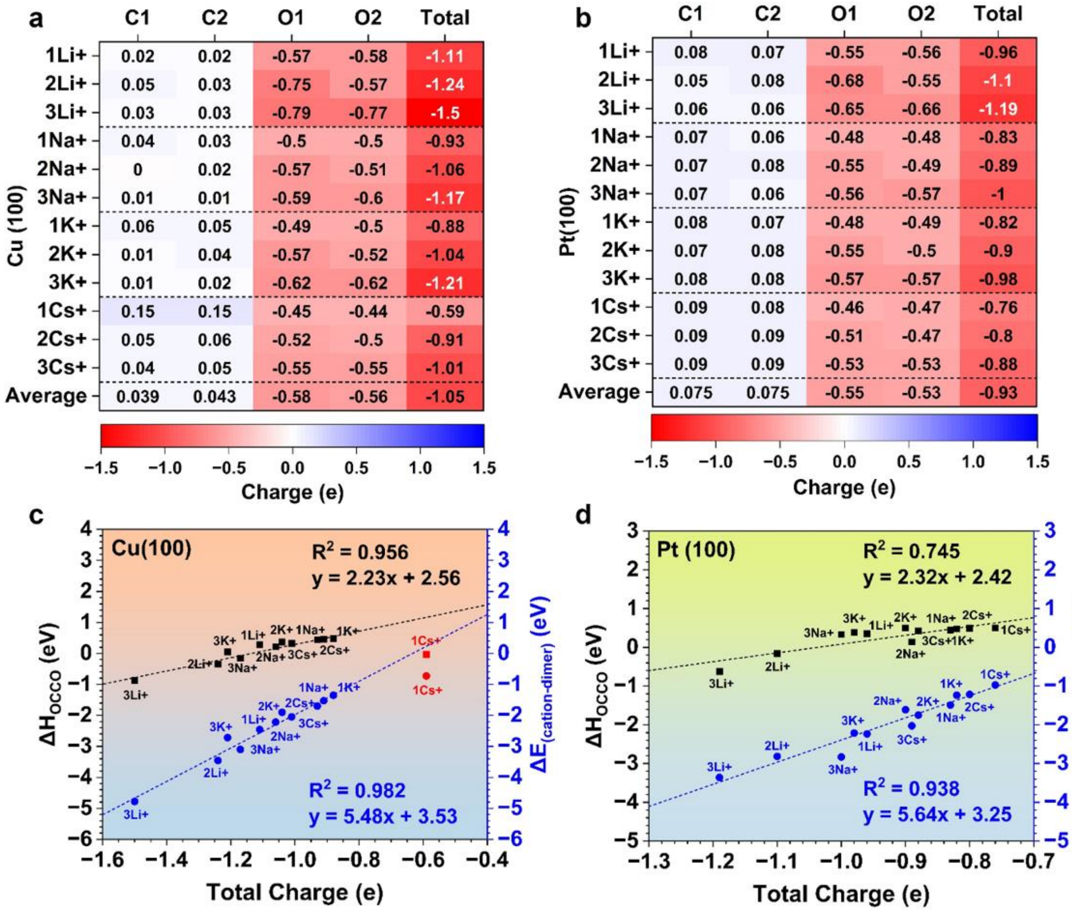

a

Cu (100)	C1	C2	O1	O2	Total
1Li+	0.02	0.02	-0.57	-0.58	-1.11
2Li+	0.05	0.03	-0.75	-0.57	-1.24
3Li+	0.03	0.03	-0.79	-0.77	-1.5
1Na+	0.04	0.03	-0.5	-0.5	-0.93
2Na+	0	0.02	-0.57	-0.51	-1.06
3Na+	0.01	0.01	-0.59	-0.6	-1.17
1K+	0.06	0.05	-0.49	-0.5	-0.88
2K+	0.01	0.04	-0.57	-0.52	-1.04
3K+	0.01	0.02	-0.62	-0.62	-1.21
1Cs+	0.15	0.15	-0.45	-0.44	-0.59
2Cs+	0.05	0.06	-0.52	-0.5	-0.91
3Cs+	0.04	0.05	-0.55	-0.55	-1.01
Average	0.039	0.043	-0.58	-0.56	-1.05

b

Pt(100)	C1	C2	O1	O2	Total
1Li+	0.08	0.07	-0.55	-0.56	-0.96
2Li+	0.05	0.08	-0.68	-0.55	-1.1
3Li+	0.06	0.06	-0.65	-0.66	-1.19
1Na+	0.07	0.06	-0.48	-0.48	-0.83
2Na+	0.07	0.08	-0.55	-0.49	-0.89
3Na+	0.07	0.06	-0.56	-0.57	-1
1K+	0.08	0.07	-0.48	-0.49	-0.82
2K+	0.07	0.08	-0.55	-0.5	-0.9
3K+	0.08	0.08	-0.57	-0.57	-0.98
1Cs+	0.09	0.08	-0.46	-0.47	-0.76
2Cs+	0.09	0.09	-0.51	-0.47	-0.8
3Cs+	0.09	0.09	-0.53	-0.53	-0.88
Average	0.075	0.075	-0.55	-0.53	-0.93

Figure 3.6.1. The Mulliken charge distribution of *OCCO molecules for (a) Cu(100) surface and (b) Pt(100) surface. The correlation between the total net charge on *OCCO and the stabilization effect on the (c) Cu(100) surface and (d) Pt(100) surface, in which the red dots represent the stabilization effect induced by cations, and black squares are the corresponding reaction energy of *OCCO formation.

Figure 3.6.1a, b shown the Mulliken population analysis of the *OCCO intermediate on Cu(100) and Pt(100) surfaces, which showed that the *OCCO carries a negative charge due to the charge transfer from the metal surfaces to *OCCO. We noticed that the cation species and metal surface affected the electron transfer (e^-). On Cu and Pt surfaces, the direct coordination of smaller cations led to the larger charge transfer and charge accumulation (~ 1.0 e^{-}) on the adsorbed *OCCO intermediate. The population analysis also showed that the electron was distributed mainly on the O atoms of the adsorbed *OCCO. In contrast, the C atoms that bind to the metal surface carry a slightly positive charge after the electron transfer. In particular, the magnitude of the negative charge on the adsorbed *OCCO intermediate is larger on Cu(100) than on the Pt(100) surface. This implied that the Cu(100) surface can better facilitate the reduction of the *OCCO intermediate through direct coordination of AM^{+}.

On the other hand, the smaller AM^{+} can induce larger electron transfer, which may contribute to better stabilization effects for the Li^{+} and Na^{+}. For the coordination of the largest Cs^{+}, negative charge accumulations of 0.91 and 1.01 e^{-} (2Cs^{+} and 3Cs^{+}) were found on the *OCCO for the Cu surface. Except for the 1Cs^{+} coordination on Cu surface, where there is no stable *OCCO form, a relatively minor electron transfer of ~ 0.59 e^{-} is observed. For the K^{+}, larger negative charge accumulations of 0.88, 1.04 and 1.21 e^{-} (1K^{+}, 2K^{+} and 3K^{+}, respectively) were observed on the Cu surface. The accumulation of negative charge on *OCCO due to coordination of Na^{+} (0.93, 1.04 and 1.17 e^{-} for 1Na^{+}, 2Na^{+} and 3Na^{+}, respectively) is very close to that of the K^{+} coordination. We think this is ascribed to the relatively small difference in their ionic radii (102 pm vs. 138 pm). For the smaller Li^{+}, the largest accumulation of negative charge on *OCCO was observed (1.11, 1.24, and 1.50 e^{-} for 1Li^{+}, 2Li^{+}, and 3Li^{+}, respectively). For the Pt surface, the overall trend of negative charge accumulation on *OCCO was preserved, but with a smaller magnitude. The overall trend of negative charge accumulation can be explained by the greater polarizing power of the smaller cations, with higher charge density, which should facilitate electron transfer via local electric fields. However, unlike the stark contrast between the smaller Li^+ and the largest Cs^+, the Na^+ and K^+ exhibit only subtle differences in their influence on the negative charge on *OCCO for the Cu surface, owing to their similar sizes, which result in comparable charge densities and polarizing capabilities. Furthermore, **Figure 3.6.1c,d** demonstrates that the electron transfer from the metal surface to the *OCCO intermediate is also correlated with the $\Delta E_{cation-dimer}$ (as well as the corresponding ΔH_{OCCO}) on both Cu(100) and Pt(100) surfaces, confirmed that the electron transfer from metal to *OCCO and the accumulation of negative charge is the key to stabilizing the intermediate.

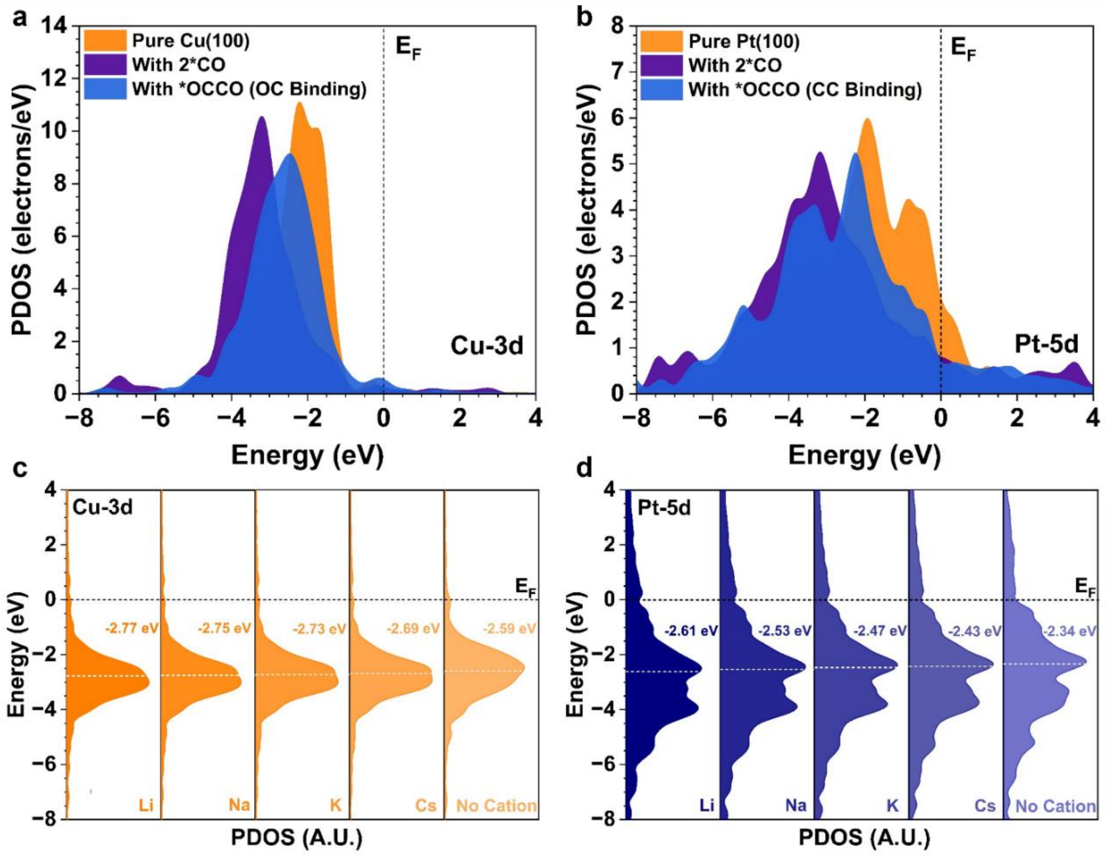

Figure 3.6.2 The shifting of the (a) 3d-states of the Cu(100) surface and (b) 5d-states of the Pt(100) surface due to the intermediate adsorption. The change of the d-band centre position of (c) Cu(100) surface and (d) Pt(100) surface under the direct cations

effect induced by alkali metal ions.

We further investigate the d-band of the Cu(100) and Pt(100) surfaces. As shown in **Figure 3.6.2**, the cations and intermediate adsorption significantly modified the d-band of the Cu(100) and Pt(100) surfaces. **Figure 3.6.2a, b** shown that as the *CO and *OCCO intermediates adsorbed on the Cu and Pt surfaces, the d-bands of the surface were moved away from the E_F. For the 2*CO adsorption, the d-band was downshifted by approximately 2 eV on the Cu(100) and Pt(100) surfaces. It is believed that the d-band shifting results from strong metal-intermediate interactions, in which the surface geometry deformation and electron transfer lead to significant d-band modification. Notably, the d-band downshifting due to the formation of *OCCO intermediate was less than 2*CO, which suggested that the adsorption of *OCCO intermediate less modifies the metal d-band owing to the weaker interaction between the *OCCO intermediate and the metal surface compared to the *CO intermediate.

The adsorption strength of the adsorbate on the TM surface can be determined by the centroid of the metal d-band, according to the d-band centre theory.[172-174] Therefore, upshifting the d-band centre on TMs with more than half-filled d-states (late-TMs) will strengthen the binding strength by reducing the population of antibonding states. In contrast, downshifting the d-band center toward the E_F resulted in weaker binding due to the increasing population of antibonding states. As the AM^+ was adsorbed on the Cu and Pt surfaces, the metal d-band centers were also modified (**Figure 3.6.2c, d**). With and without cation adsorption, the fully occupied Cu d-band lies below the E_F due to the Fermi–Dirac distribution. The low-lying d-band may explain the moderate intermediate adsorption on the Cu surface.

On the other hand, the Pt metal, with a partially filled d-band, was pinned near the E_F, allowing stronger intermediate adsorption than on the Cu surface. With the adsorption of AM^+, the d-band centre of Cu and Pt metals was significantly downshifted to lower energy, indicating that the adsorption of cations could alleviate the intermediates binding by d-band modification. On the Cu(100) surface, the d-band centre gradually upshifted from −2.77 eV to −2.69 eV by changing the cation from the smallest Li^+ to the largest Cs^+ (vs. −2.59 eV without cation), and the *OCCO adsorption energy downshifted from −0.87 eV to −1.43 eV. While on the Pt(100) surface, a similar trend of d-band centre variation was observed. Our results demonstrated that the larger alkali cations led to a less downshifted d-band centre on the Cu and Pt surfaces. Hence, the stronger intermediate adsorption on the Cu(100) and Pt(100) surfaces with Na^+, K^+, and Cs^+ can be attributed to their higher d-band centres than those of Li^+.

Based on the DFT calculations, the stronger *OCCO adsorption tends to result in larger ΔH_{OCCO} for CO dimerization. Hence, the moderate adsorption strength with smaller cations benefits the *OCCO formation, especially on the Cu surface. However, the difference in the d-band centre under different AM^+ was relatively small compared to the corresponding variation in adsorption energy. Therefore, we believe that the d-band centre modification may not fully contribute to the significant change in adsorption energy. Also, unlike the *OCCO intermediate, the upshift of the d-band centre resulted in weaker cation adsorption on Cu and Pt surfaces. This is because the AM^+ and metal surface interactions are mainly electrostatic. However, in a practical solution environment, the adsorption of AM^+ is inhibited by its much higher solvation energy.[175-176]

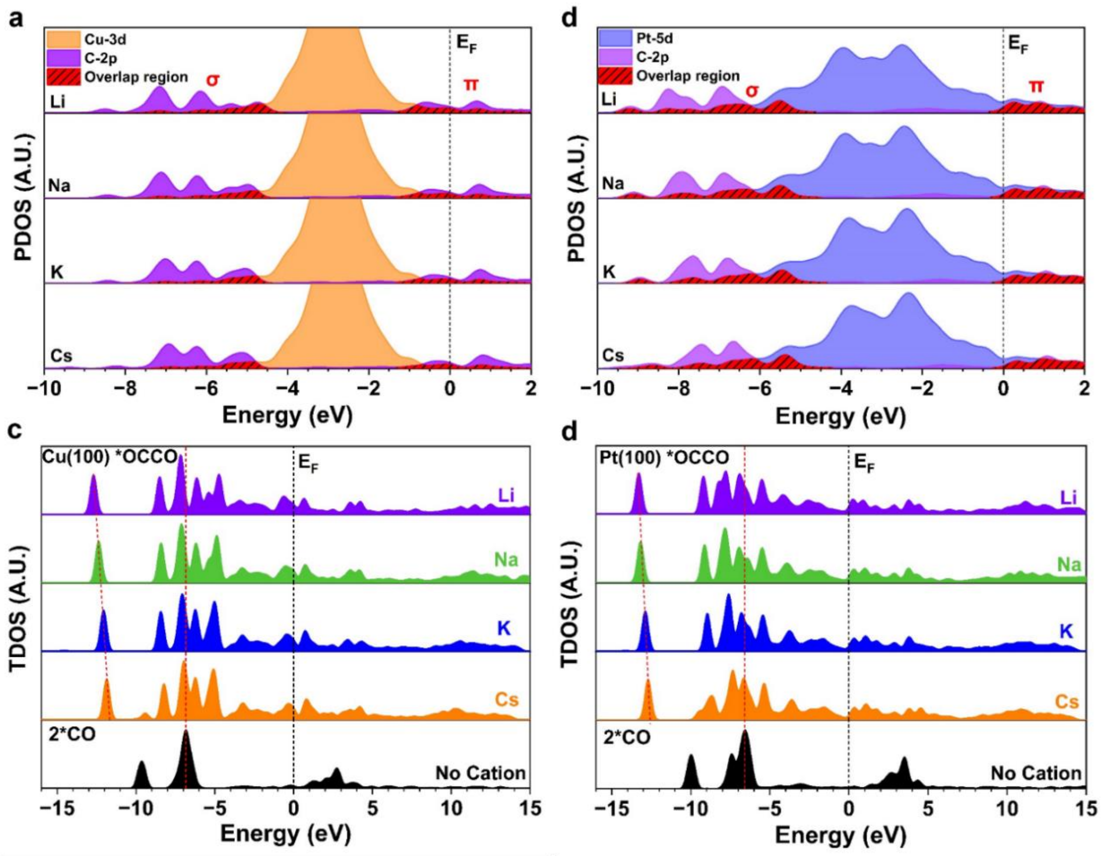

Figure 3.6.3 The PDOS and p-d orbital overlapping of binding metal sites and carbon atoms of *OCCO adsorbed on (a) Cu(100) surface and (b) Pt(100) surface. The TDOS of *CO and *OCCO adsorption on (c) Cu(100) surface and (d) Pt(100) surface.

The partial density of states (PDOS) analysis investigated the orbital coupling between the intermediate and metal adsorption sites. **Figure 3.6.3a, b** shows the p–d orbitals coupling between the binding metal sites and carbon atoms of *OCCO adsorbed on Cu(100) and Pt(100) surfaces, in which the overlapping area between the C-2p and metal d-states was used to evaluate the carbon-metal interactions. In general, the interplay between frontier orbitals, the highest occupied molecular orbital and lowest unoccupied molecular orbital (HOMO/LUMO), of the *OCCO intermediate and valence metal d-states results in low-lying σ-region and π-region interaction near E_F. For the adsorption *OCCO intermediate on the Cu(100) surface, the p-d overlapping on the σ-region and π-region showed a noticeable increase when changing the AM^+ from Cs^+ to Li^+, where the p-d overlapping area increases monotonically from 0.78 to 0.95 e^- and 0.72 to 0.89 e^- on the σ-region and π-region, respectively. On the other hand, the broad 5d orbitals of the Pt metal lead to a sizable overlap between the C 2p and Pt 5d orbitals. However, we revealed an opposite trend of the p-d overlapping area on the σ-region and π-region for the *OCCO adsorption on the Pt(100) surface, in which the overlapping on the σ-region decreased from 1.65 to 1.51 e^-. The overlap on the π-region increased from 0.83 to 0.91 e^- when varying the AM^+ from Cs^+ to Li^+.

On the Cu(100) surface, increasing p–d overlapping on the σ-region and π-region when changing the cation implied directional electron transfer via the p–d orbital interaction. The resulting electron transfer via the p-d channel is believed to lead to the enhanced charge accumulation of the adsorbed *OCCO intermediate on the Cu surface. While on the Pt(100) surface, the opposite trend of the p–d overlapping on the σ-region and π-region indicated that the cations have less impact on electron transfer between the *OCCO and the Pt(100) surface. As a result, no obvious charge redistribution occurred with limited enhancement on *OCCO formation on the Pt(100) surface with AM^+ coordination.

In particular, LUMO states of *OCCO 2p are mainly located above E_F on the Pt(100) surface, in which the empty Pt-5d and C-2p states above E_F revealed that the binding of *OCCO is mainly via ionic/electrostatic interactions due to the partially filled π-region. Meanwhile, the LUMO states of *OCCO 2p significantly downshifted in energy and approached the E_F on the Cu(100) surface. This downshifting results from the E_F shifting for the chemisorbed *OCCO due to electron transfer from the Cu surface. In addition, we noticed that the change of the AM^+ from Cs^+ to Li^+ increased the splitting of the *OCCO 2p peaks located at around –6.5 eV due to the stronger C–C bond formation with the coordination of smaller AM^+. It is believed that the larger splitting of the 2p peaks originates from the C–C bond length decreases of *OCCO on Cu(100) and Pt(100) surfaces when changing the AM^+ from Cs^+ to Li^+.

The TDOS of the adsorbed *CO and *OCCO intermediate on Cu(100) and Pt(100) surfaces is shown in **Figure 3.6.3c,d**. For Cu(100) and Pt(100) surfaces, the TDOS spectrum was shifted to lower energies after forming *OCCO from 2*CO. Mainly, a smoother 2*CO to *OCCO conversion was observed on the Cu(100) surface compared to the Pt(100) surface. Additionally, on the Cu(100) surface, a more pronounced downshift of the TDOS is observed when the cation is changed from Cs^+ to Li^+, consistent with the previous discussion of the greater stabilization of larger cations on the Cu(100) surface. Furthermore, unlike the TDOS of 2*CO with a singlet peak at around −7.0 eV, the *OCCO displayed multiple patterns in the same region, which was associated with the C−C bond formation and the splitting of C 2p peaks in PDOS. The adsorbed *OCCO also displays more states at low energy levels than the adsorbed *CO, including a low-lying peak at about –13 eV. The TDOS above E_F was smeared out after forming *OCCO intermediate from 2*CO, indicating the increase of bonding states below the E_F. Also, the HOMO and LUMO were separated by a wide energy gap for the adsorbed *CO, which usually implies low chemical reactivity (high stability) of the 2*CO intermediate on the metal surface since adding (or extracting) electrons from high-lying LUMO (low-lying HOMO) is energetically unfavourable.[177-178] In contrast, the overall low stability of the adsorbed *OCCO was indicated by the higher TDOS near the E_F region, suggesting that the *OCCO is more reactive than the *CO.

3.7 Other C–C Coupling Pathways

The other C–C coupling pathways for forming C_2 intermediates were also studied intensively. According to previous studies, C_2 intermediates can also be formed by the coupling between *CO and *CHO/*COH species.[179-182] These alternative C–C coupling pathways required the *CO being hydrogenated ($+H^+/e^-$) to *CHO or *COH before the formation of C–C bonding, in which a theoretical study found that the hydrogenation of *CO usually occurs under high potential on the metal surface.[183] Meanwhile, although recent studies have revealed that the presence of H_2O and solvation effects can drive *CO hydrogenation, the step remains energetically uphill on the Cu surface with solvation treatment.[184] Based on that, CO hydrogenation on metal was also widely regarded as the key elementary step for the C_2 pathways.

Table 3.7.1 Adsorption energy (eV) of *CO, *CHO, *OCCHO and *OCCO on the

Cu(100) surface, where the adsorption energy of *CHO and *CHOCO are from ref.[185]

Intermediate	***CO**	***CHO**	***OCCHO**	***OCCO**
No Cation	-0.23	0.51	0.44	–1.22 (O–C binding)
Li^+	-0.60	-0.10	-0.54	–0.87
Na^+	-0.60	-0.01	-0.58	–1.24
Cs^+	-0.64	0.10	-0.66	–1.43

During the *CO hydrogenation, both *CHO and *COH are the possible C_1 intermediates. However, studies suggested that different C_1 intermediates are stabilized differently on various surfaces and require different strategies to stabilize each intermediate. For the *COH intermediate, recent DFT results reveal that there are no significant differential cation stabilization effects among alkali cations, which is indicated by the negligible differences in *COH adsorption energetics.[186] More importantly, the formation of the *COH intermediate is less favorable on the Cu(100) surface due to its higher activation barrier compared to that of *CHO, which contrasts with the results on the Cu(111) surface.[187] Since the formation of *COH requires the O–H bond forming, in which a proton is shuttled through a water molecule to the adsorbed *CO. In this H-shuttling process, the H_2O participates by forming a transient $H_3O^{\delta+}$ in the transition state, but the $H_3O^{\delta+}$ is less stable on Cu(100) compared to Cu(111), thereby restricting *COH formation. On the other hand, the lower coordinated surface Cu atoms on Cu(100) could better stabilize the C–H bond formation transition state for the *CHO formation. Therefore, we believed the C–C coupling between *COH and *CO intermediates could be exclusive for C_2 pathways on Cu(100) surfaces. Concerning the *CHO intermediate, previous DFT studies demonstrated that *CHO and *CO coupling are more favorable than 2*CO coupling on the Cu(100) surface under vacuum. However, CO dimerization is more kinetically favourable under explicit solvation treatment.[188]

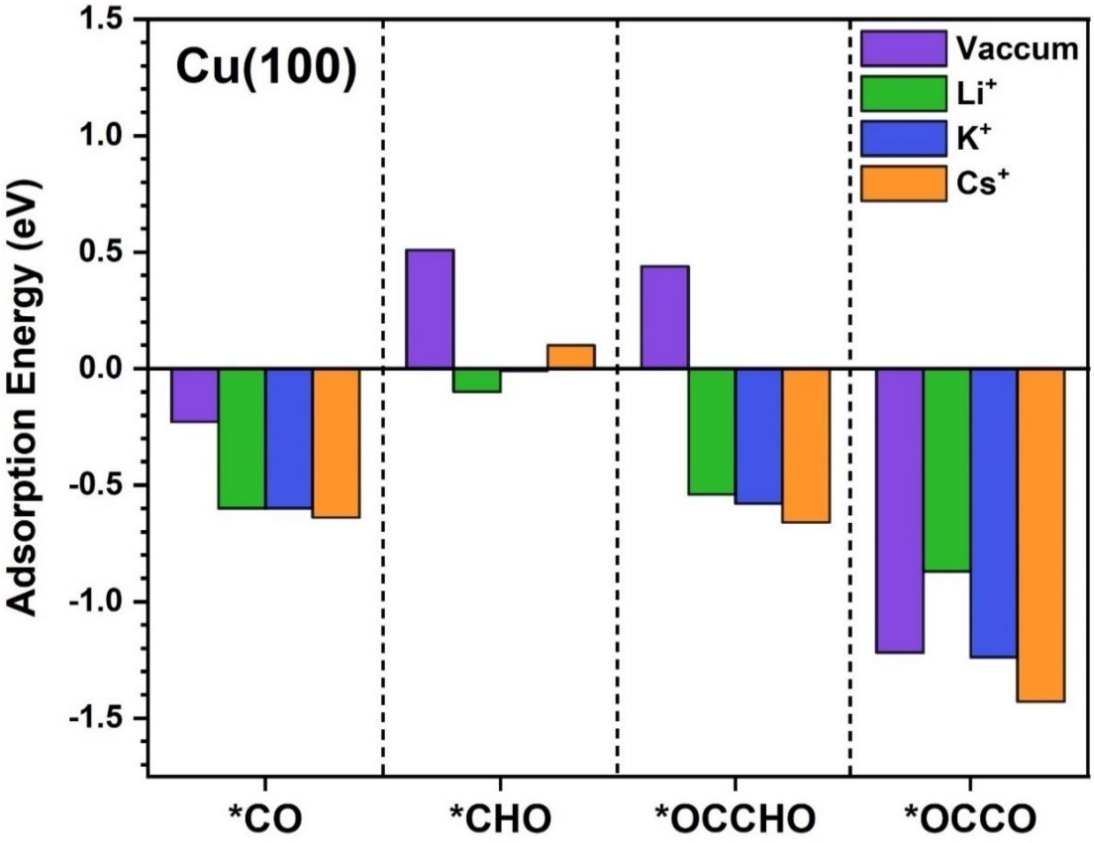

Figure 3.7.1 Adsorption energy of *CO, *CHO, *CHOCO, and *OCCO intermediates on Cu(100) surface, where the adsorption energy data of *CHO and *CHOCO are from previous literature.[185]

The adsorption energies (*CO, *CHO, *OCCHO and *OCCO) and energy barrier of CO dimerization and protonation were listed in **Table 3.7.1** and shown in **Figure 3.7.1**. Adsorption energy data showed that Cu(100) weakly adsorbed the *CHO intermediate (E_{ads} = 0.51 eV) in the absence of cations. The cation species (Li^+, Na^+, and Cs^+) strengthen the adsorption of ~ 0.5 eV on the Cu(100) surface, but the adsorption of *CHO is still weaker than *CO, *OCCHO and *OCCO intermediates. The weak adsorption of the *CHO intermediate implied that the *CHO was challenging to retain in high coverage for the C–C coupling process compared to *CO intermediate, which makes the coupling between *CO and *CHO rarely occur on the Cu(100) surface. Similarly, the adsorption strength of *OCCO is stronger than that of *OCCHO on the Cu(100) surface under both vacuum and the effect of cations. This suggests that the *OCCHO is less stable than the *OCCO on the Cu(100) surface with or without the presence of cations.

Table 3.7.2 The energy barrier (eV) for the possible C-C coupling reactions on the Cu(100) surface.

Reaction Step	**$*CO + *CO \rightarrow *OCCO$**	**$*CO + H \rightarrow *CHO$ [187]**
No Cation	1.16 (O–C binding)	0.73
Li^+	0.10	0.49

Na⁺	0.13	0.59
Cs⁺	0.33	0.54

Regarding the barriers for CO dimerization and *CO protonation (**Table 3.7.2**), it is shown that the formation of *CHO (*CO + H → *CHO) has a lower energy barrier than CO dimerization on the Cu(100) surface. However, introducing cation species has significantly reduced the energy barrier (1.06 eV) for CO dimerization on the Cu surface. In contrast, the energy barrier for *CHO formation was less affected by the cations, with a relatively minor decrease of 0.24 eV (**Figure 3.7.2**). Therefore, in the presence of cations, CO dimerization is more favorable than *CHO formation on the Cu(100) surface because of the lower energy barrier. Based on that, we believe the CO dimerization is more favoured than the *CHO–*CO coupling on the Cu(100) surface with cationic interactions. Additionally, previous calculations have also demonstrated that the promotion of *OCCO formation by cationic interactions can be attributed to the greater stabilization of C_2 intermediates compared to the regular C_1 intermediate on metal surfaces.[185] This suggests that the direct cation effects may play a similar role in other C–C coupling routes. Based on that, our results can also be considered as the initiation point for future studies of other C–C coupling among *CHO/*COH/*CO species.

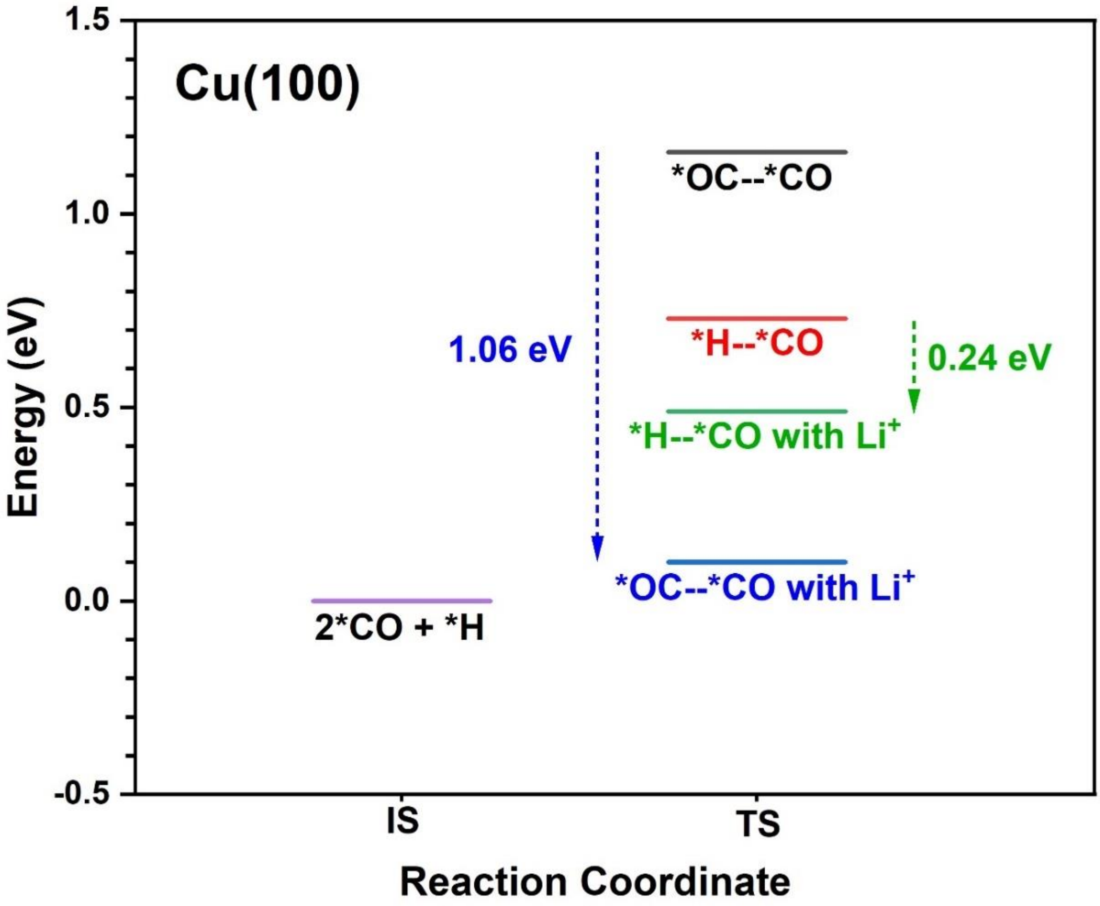

Figure 3.7.2. The energy barrier of CO dimerization from our work and *CHO formation from previous literature on the Cu(100) surface.[187]

3.8 Summary

In conclusion, the direct cation effects on CO dimerization on Cu and Pt surfaces were investigated using DFT. The adsorption, reaction, and stabilization energies calculations showed that the presence of AM^+ (Li^+, Na^+, K^+ and Cs^+) can significantly promote the formation of *OCCO via direct coordination. In particular, the coordination of smaller cation species (Li^+ and Na^+) can induce greater stabilization, characterized by lower energy barriers and reaction energies, in the CO dimerization process. Meanwhile, a strong linear correlation was observed between cation–dimer stabilization and the reaction energy of CO dimerization, suggesting that the reduction in reaction energy was highly correlated with the cation-induced stabilization.

On the other hand, the population analysis demonstrated that the direct cation stabilization effects may be related to the enhancement of electron transfer from the metal surface to the adsorbed *OCCO intermediate, in which the *OCCO formation on Cu(100) surface with smaller AM^+ is facilitated by the larger negative charge on *OCCO. Lastly, the electronic structures investigation showed that the d-band of the Cu(100) and Pt(100) surfaces was significantly modified by the adsorption of intermediate and cation species, where the d-band downshift altered the adsorption strength of *OCCO on metal surfaces. More importantly, the PDOS and TDOS revealed that the effective electron transfer via p-d orbital coupling between the chemisorbed *OCCO and Cu(100) benefits the *OCCO formation. We believed our work could offer valuable insights into the effects of cations on CO dimerization, providing excellent opportunities to synthesize C_2 products via CO_2RR.

Chapter 4. Solvation of Alkali Metal Cation in Aqueous Solution

4.1 Introduction

In addition to local pH and electric fields, water structure also plays a crucial role in the CO_2RR process.[189-192] The dipole moment on water molecules enables them to form hydrogen bonds with other water molecules (**Figure 4.1.1a, b**), resulting in a rigid hydrogen-bonding network. More importantly, the interfacial hydrogen-bonding networks may play a specific role in electrocatalysis, in which cations coordinate with water molecules, forming a solvated cation near the electrode surface (**Figure 4.1.1c**). For instance, research has shown that the hydrogen-bond structure is also influenced by cation size, with smaller cations facilitating the formation of hydrogen-bond networks. In contrast, the larger cations tend to break the networks (**Figure 4.1.1d, e**).[193] The effects of cation species on hydrogen-bonding networks were revealed by ab initio molecular dynamics (AIMD) simulations (**Figure 4.1.1f, g**).[194] The number of interface water molecules (N_w) gradually decreases as larger cations are introduced at the interfaces. In addition, the average number of hydrogen bonds (N_{Hbond}) accepted by adsorbed *CO is significantly affected by the size of cations, in which the smallest cation Li^+ has the highest N_{Hbond} compared to the other larger cations. The study conducted that the change in N_{Hbond} is attributed to the surface charge density variation under different cations, where the cation with a higher Helmholtz capacitance can lead to higher negative surface charge density under the same electrode potential.

The hydrogen-bonding network plays a crucial role in influencing the formation of the C_2 product during CO_2RR. A weakened hydrogen-bonding network restricts the separation of C_1 intermediates, thereby decreasing the distance between adjacent C_1 intermediates and facilitating C–C coupling.[195-197] For example, Li et al. claimed that the cation-induced electric field near electrode surfaces is too small to modulate the C_2 product selectivity.[198] While surface-enhanced infrared absorption spectroscopy (SEIRAS) results suggested that larger cations can disrupt hydrogen bonding between interfacial water molecules and *CO, thereby tuning the selectivity of CO_2RR on a Cu electrode in aqueous electrolytes. However, a recent theoretical study revealed that small cations with tight hydrogen-bonding networks can enhance proton transfer kinetics during CO_2RR on a molecular cobalt catalyst.[199]

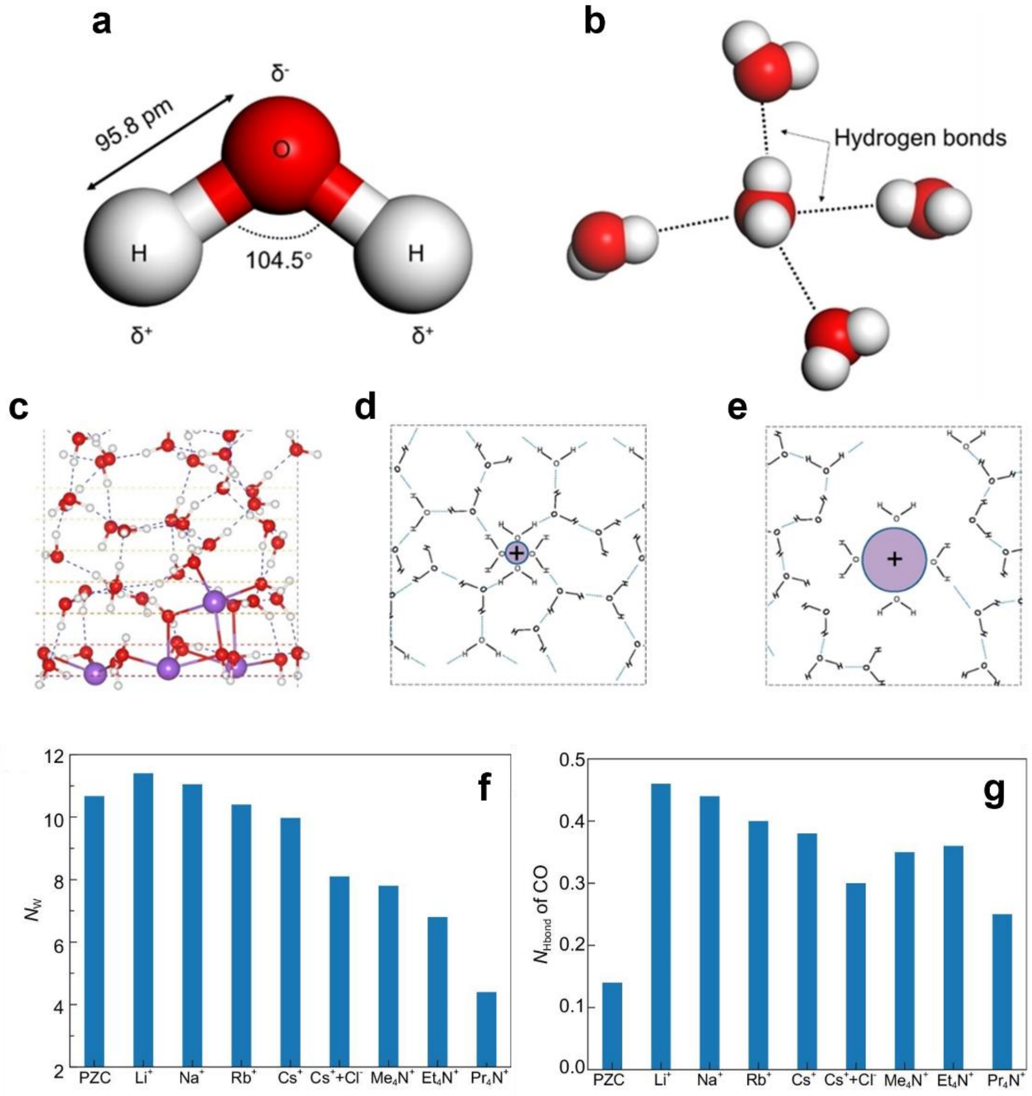

Figure 4.1.1 (a) Molecular structure and dipole moment of the H_2O molecule. (b)

Hydrogen-bonding network between H_2O molecules. (c) The MD simulated the hydrogen bond network with the influence of cations. (d) The small cations make the hydrogen bond structure. (e) The large cations break the hydrogen bond structure.[193] (f) Number of interface water molecules (N_w) with different cations. (g) Averaged hydrogen bonds (N_{Hbond}) number between the surface *CO and water.[194]

A recent study also proposed an effective method to manipulate the interfacial hydrogen-bonding network through inherently implanting Cu_2O using C_8F_{18} during CO_2RR.[200] By strengthening interfacial hydrogen bonding connectivity with C_8F_{18}, the preferred C_2 product shifted from ethylene to ethanol in CO_2RR. The investigation found that the highly electronegative F on C_8F_{18} enables the molecule to form strong hydrogen bonds with H_2O and other O-containing intermediates, which also promote H* formation and favor the *CHCOH to *CHCHOH conversion due to enhanced hydrogen bonding. The DFT calculations revealed that the F-modified Cu(111) surface can significantly reduce the adsorption energy of H_2O and the energy barrier to H_2O dissociation, owing to a strengthened hydrogen-bond network. As a result, the enhanced H_2O dissociation increases the *H coverage, facilitating the protonation of *CO (*COH formation). Further calculation of reaction energy also demonstrated that the formation energy of the *CCH (ethylene pathway) on the pristine Cu(111) surface is lower than for *CHCHOH (ethanol pathway). However, the formation energy of *CHCHOH diminished with F-modified Cu(111). It was lower than that for forming *CCH, which indicated the preference for ethanol production on the F-modified Cu(111) surface.

Similarly, studies also found that reducing the number of hydrogen bonds in the near electrode surface can also inhibit the HER as well as the protonation of the C_1 intermediates (*CO to *COH), which suggests that the formation of *COH from *CO makes the C–C coupling process less thermodynamically favourable. For example, organic electrolyte cations (tetraalkylammonium cations) were developed to promote non-aqueous CO_2 reduction.[201] While studies have shown that not only the strength of the electric field would be affected by the size of organic electrolyte cations (length of the alkyl chain), the tetraalkylammonium cations with longer alkyl chain also help maintain hydrophobicity on the Cu surface, which suppresses the side completing HER and promotes the C–C coupling.

Solvation is defined as the interaction between solute and solvent molecules, in which the solvation of a solute by water is also known as hydration. The solvation of cations significantly impacts the properties of electrolytes in solution. In general, the solvation of ions is characterized by a negative solvation enthalpy that is significantly lower than the associated negative entropy, where the electrostatic effects primarily contribute to the negative Gibbs free energy of solvation.[202-203] For the 1st row AM^+, the solvation enthalpy at room temperature increased as the size of the cations increased, in which the smallest Li^+ has the highest charge density and stronger ion-water electrostatic interaction.

In particular, the electrocatalytic reaction at the metal surface was strongly influenced by the interaction between the cation and the solvent molecule near the electrode surface. In a bulk aqueous electrolyte, the ions and water molecules from solvated ions are considered the basic charged transport units. The strength of the ion-water interaction primarily determines the structure and CN of solvated ions. Therefore, determining solvation characteristics can effectively enhance understanding of the role of solvated cations in CO_2RR for C–C coupling. Herein, we investigated the cation solvation properties of AM^+ (Li^+, Na^+, K^+ and Cs^+) by determining the CN via MD simulations. Moreover, further DFT investigation was carried out to determine the structure of the solvated ion and the reactivity of the AM^+ centre.

4.2 Computational Details

4.2.1 Molecular Dynamics (MD) Simulations

MD simulations were conducted using the Forcite module within the Materials Studio software. The simulations were performed under the NVT ensemble at 298 K. An initial 5 picosecond simulation was performed to achieve equilibrium at 298 K. For the production phase, MD simulations were conducted under the NPT ensemble, maintaining a constant temperature of 298 K and ambient pressure for 20 nanoseconds. Each MD simulation step used a time increment of 1 femtosecond, and the COMPASS II force field, an ab initio force field suitable for both organic and inorganic systems, was employed to model all ion interactions.[204-205]

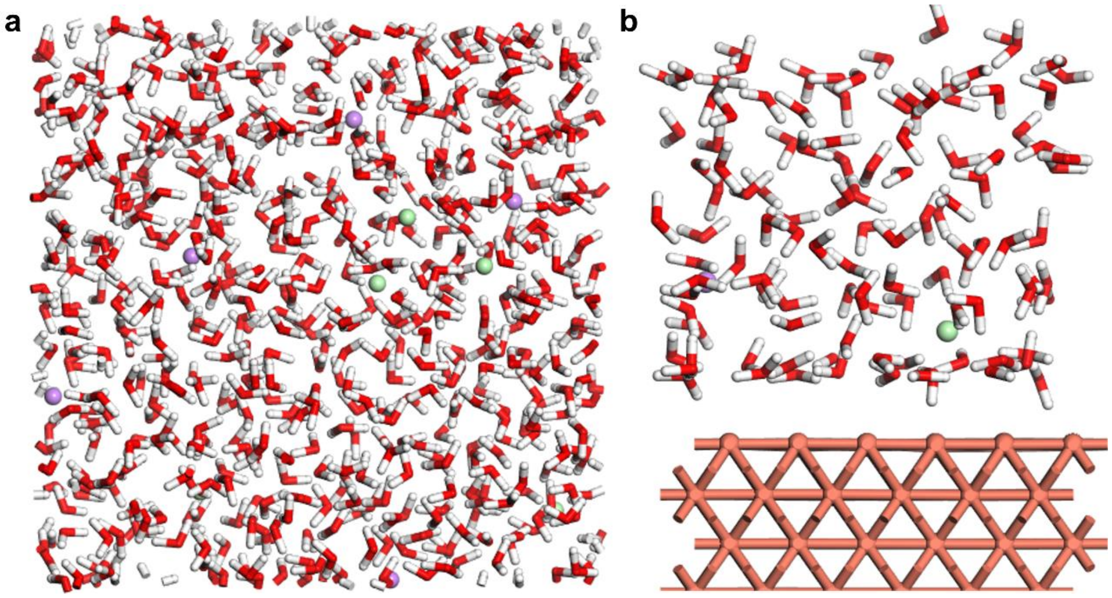

Figure 4.2.1 (a) Bulk electrolyte model and (b) electrode-electrolyte interface model. The red and white sticks represent H_2O molecules. The light purple and green spheres represent AM^+ cations and Cl^- anions, respectively.

The Nosé–Hoover thermostat and Berendsen barostat were applied to control the temperature and pressure during the MD simulations. The $LiCl_{(aq)}$, $NaCl_{(aq)}$, $KCl_{(aq)}$ and $CsCl_{(aq)}$ were selected as the electrolyte models for the MD simulations. Each electrolyte model includes 555 H_2O molecules, 5 AM^+ and 5 Cl^- anions in the cell, representing an electrolyte concentration of ~ 0.5 M for typical CO_2RR (**Figure 4.2.1a**).[155] The electrode-electrolyte interface model includes 111 H_2O molecules, 1 AM^+ and 1 Cl^- anions as the electrolyte, and Cu(100) metal slabs with a 4 × 4 supercell and five atomic layers as the Cu electrode (**Figure 4.2.1b**).

4.2.2 DFT Calculations

The electrolyte effects of solvated AM^+ (Li^+, Na^+, K^+ and Cs^+) on CO_2RR were calculated using the spin-polarized DFT with the implicit solution method. The structure of the solvated cations was based on the CN determined by the MD simulations. The DFT calculations were performed using the $DMol_3$ package.[206-207] The exchange-correlation potentials are described by the GGA-PBE functional.[137] The DSPP core treatment method and the DNP basis set with an orbital cutoff of 5.1 Å were employed for all solvated cation structures.[129, 208] The k-point separation was kept as 0.05 $Å^{-1}$. The long-range interactions were described by Grimme's empirical correction scheme (DFT-D2) with a reparametrized C_6 coefficient on AM^+.[209-210] The COSMO with a dielectric constant of 78.4 was used as the implicit solvation model to simulate the aqueous environment.[211] The convergence criteria for SCF calculations and geometry optimizations were selected as follows: SCF tolerance is 10^{-5} Ha, the maximum force is 0.004 eV/Å, and max. displacement is 0.005 Å.

4.3 Radial Distribution Function Analysis

The solvation structure of the AM^+ in an aqueous solution can be determined by MD simulations, in which the RDF were widely used to visualize the solvation of ions by the H_2O molecules.[212]

$$RDF = g\,(r) = \frac{dN}{4\pi r^2 \rho dr}$$

The $g\,(r)$ defined as the probability of finding an atom at a distance (r) from another tagged atom.

$$CN(r) = \int_0^r 4\pi r^2 \rho g(r) dr$$

The CN can be determined by integrating $g\ (r)$ into spherical coordinates to the first minimum of the RDF curve. The first peak of the RDF curve also gives the AM^+–O (H_2O) bond length in the first solvation shell of the H_2O molecule.

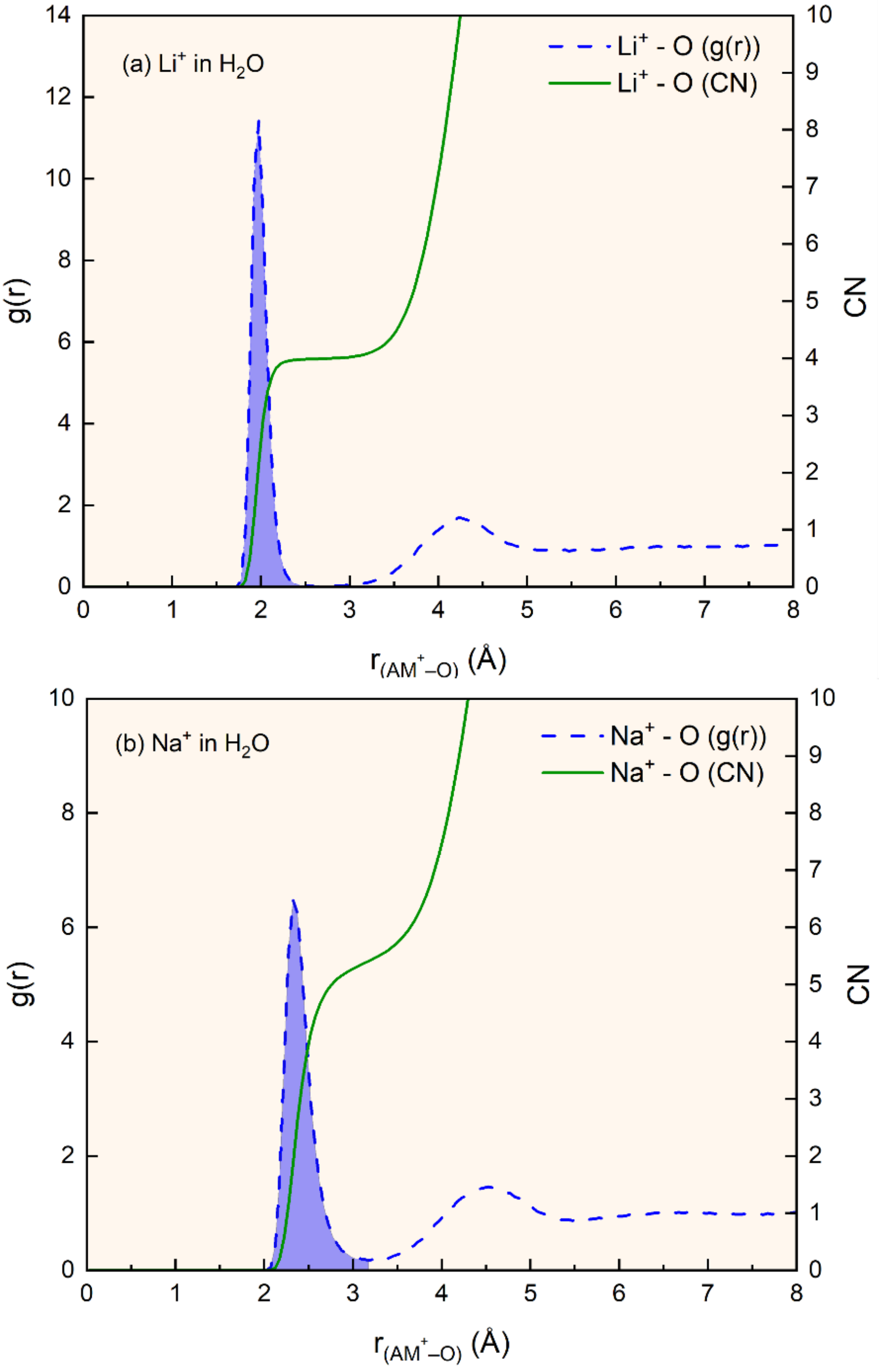

Figure 4.3.1 AM$^+$–O RDF for the 0.5 M (a) LiCl$_{(aq)}$ and (b) NaCl$_{(aq)}$. The blue dotted line represents the RDF, and the green line represents the integration of the RDF curve.

With the increase in ionic radius, the location of the first peak is shifted to a longer distance when changing from Li^+ to Cs^+. For the smallest Li^+ cation (**Figure 4.3.1a**), the RDF curve displayed a narrow peak at ~1.98 Å. At the same time, integration of the RDF curve of the first peak leads to a CN of ~ 4 for the $AM^+ - O$ (H_2O) in bulk aqueous. For the larger Na^+ cation (**Figure 4.3.1b**), the location of the first peak increased to 2.33 Å due to the increase in ionic radii for Na^+, and the integration of the broader peak also led to a higher CN of ~ 5.5. Besides, the first peak of RDF for Li^+ and Na^+ is sharp with a deep minimum. The sharp peak on Li^+ and Na^+ indicates that the first solvation shell is well-defined, and the H_2O molecules between the first and second solvation shells should be completely depleted. This could be attributed to the strong cation-water electrostatic interaction for the smaller Li^+ and Na^+ cations, in which the cation binds tightly to the water molecule, shielding the interaction between the cation and the second solvation shell. At the same time, a broader peak located at 2.73 Å and 3.18 Å was observed for larger K^+ and Cs^+ (**Figure 4.3.2**), respectively. The broad distribution of the first peak indicated CN values of ~7 for K+ and ~8 for Cs^+ in bulk aqueous solution. In addition, the broad first peak of the $AM^+ - O$ (H_2O) RDF curve also indicated that the solvation shell of K^+ and Cs^+ is relatively unstructured and diffuse compared to the smaller Li^+ and Na^+. Furthermore, the Cu(100) surface was introduced to the cell model to determine the CN of AM^+ near the metal surface. The MD simulations showed no significant variation in the AM^+–O (H_2O) bond length and CN near the metal surface compared to the bulk.

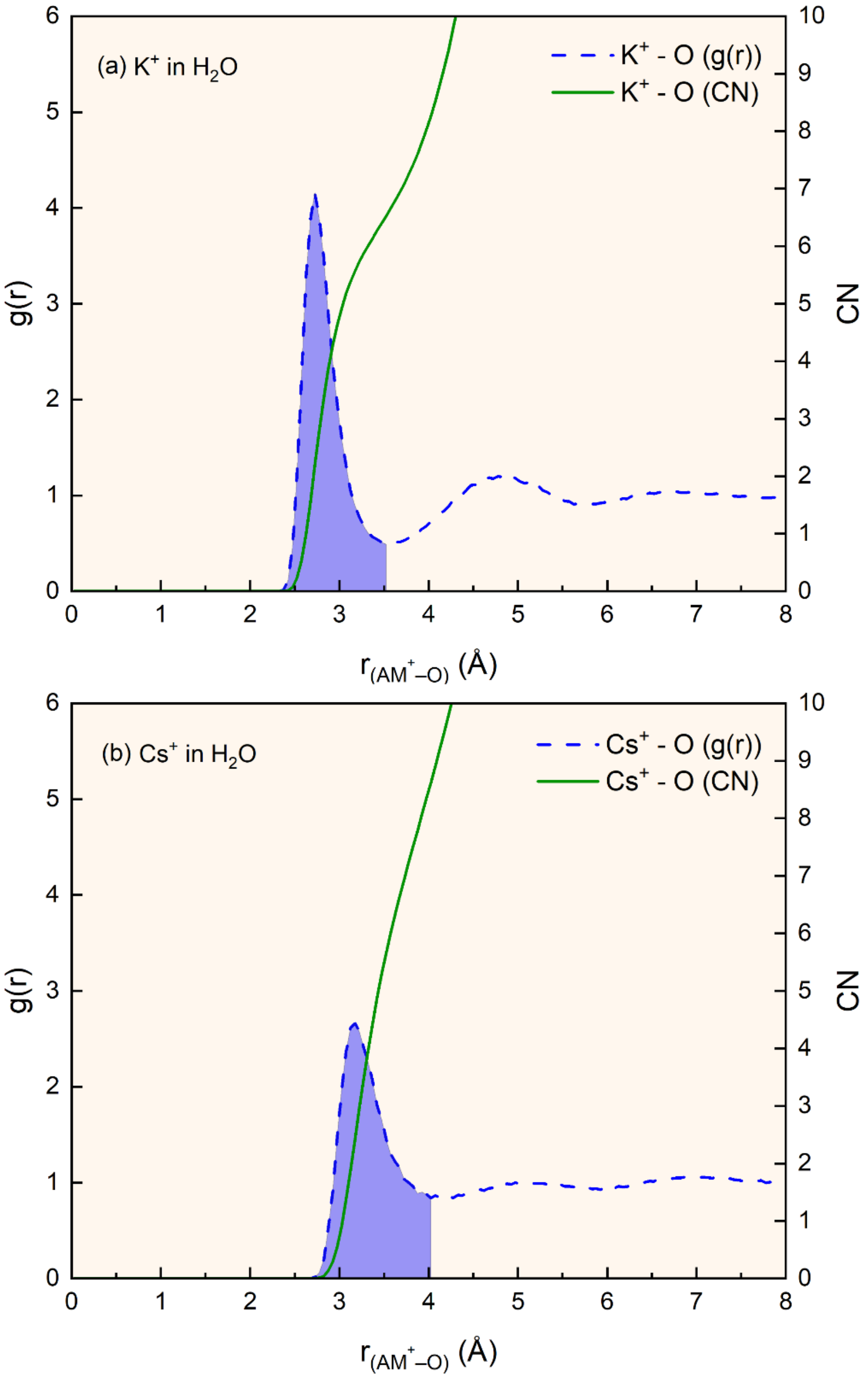

Figure 4.3.2 AM$^+$–O RDF for the 0.5 M (a) KCl$_{(aq)}$ and (b) CsCl$_{(aq)}$. The blue dotted line represents the RDF, and the green line represents the integration of the RDF curve.

4.4 Structural and Electronic Properties of Solvated AM^+

The structure of the solvated AM^+ was determined by the DFT calculations with implicit solvation treatment. **Table 4.4.1** shown the CN and coordination structures (first solvation shell) for Li^+, Na^+, K^+ and Cs^+ determined by the MD simulation. For smaller Li^+ and Na^+ cations, the CN of 4 and 6 suggests the tetrahedral-like $[Li(H_2O)_4]^+$ and octahedral-like $[Na(H_2O)_6]^+$ coordination structures in aqueous solution. For K^+ and Cs^+ cations, the larger cations could coordinate with more water molecules with an unstructured first solvation shell. Therefore, the K^+ and Cs^+ cations had difficulty in maintaining the coordination structures with water molecules while interacting with the *CO and *OCCO intermediates.

Table 4.4.1 The CN, solvated AM^+ structure and Fukui indices for Li^+, Na^+, K^+ and Cs^+ cations in aqueous solution.

AM^+	CN	Solvated Ion	Average M-O Bond Length (Å)	Fukui (+)
Lithium(I)	4	$[Li(H_2O)_4]^+$	1.97	0.016
Sodium(I)	6	$[Na(H_2O)_6]^+$	2.43	0.064
Potassium(I)	7	$[K(H_2O)_7]^+$	2.80	0.079
Cesium(I)	8	$[Cs(H_2O)_8]^+$	3.29	0.133

The structural details of the solvated ions were determined by using DFT with an implicit solvation model. The 4-coordinated $[Li(H_2O)_4]^+$ has an average $Li^+ - O$ bond length of 1.97 Å, which is very close to the RDF peak position (1.98 Å) obtained from MD simulation. This should be attributed to the narrow *RDF* distribution of the first peak for the Li^+ cation. In contrast, for the 6-coordinated $[Na(H_2O)_6]^+$, the optimized solvated ion structure has an average Na^+–O bond length of 2.43 Å, larger than the RDF peak position of 2.33 Å. For the $[K(H_2O)_7]^+$ and $[Cs(H_2O)_8]^+$, the RDF based on MD simulation indicated 2.73 Å and 3.18 Å AM^+–O bond length for most of the $[K(H_2O)_7]^+$ and $[Cs(H_2O)_8]^+$, respectively. However, the DFT results suggested a larger AM^+–O bond length for $[K(H_2O)_7]^+$ (2.80 Å) and $[Cs(H_2O)_8]^+$ (3.29 Å).

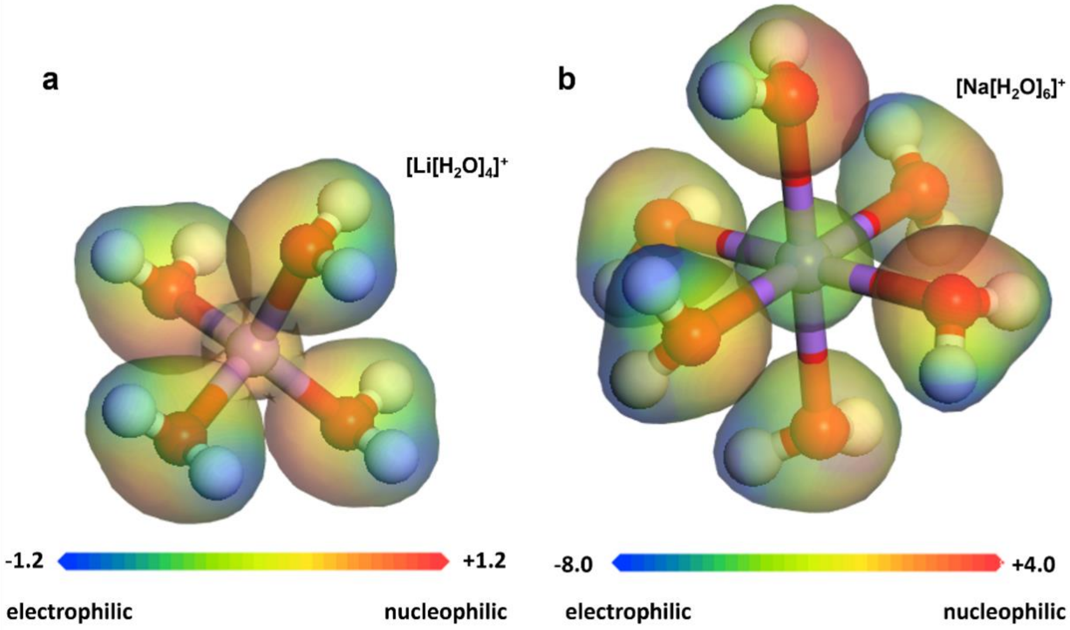

Figure 4.4.1 The charge distribution of (a) $[Li(H_2O)_4]^+$ and (b) $[Na(H_2O)_6]^+$.

The Fukui function was widely used as a reactivity index to indicate the site that preferentially accepts or donates electrons. The Fukui function describes the change in electron density when the number of electrons changes (either by adding or removing electrons). In the case of adding an electron, it indicates the reactivity of the site that will react with nucleophiles:

$$\text{Fukui function (add electron)} = \rho(N+1) - \rho(N)$$

Where $\rho(N)$ is the electron density of the neutral state (N electrons) and $\rho(N+1)$ is the electron density with N+1 electrons. The Fukui function can also be used to quantify local chemical reactivity by computing the atomic charge (q_k):

$$\text{Fukui (+)} = q_k(N+1) - q_k(N)$$

The atomic charge can be computed from several methods, such as Hirshfeld, Mulliken, Voronoi, and Bader charges. In this work, Fukui (+) values were calculated at the GGA-PBE/DNP (4.4 Version) level, and atomic charges were computed from Mulliken population analysis. The larger the Fukui (+) value of the site, the more easily the site accepts electrons (nucleophile). The O atom in *CO and *OCCO intermediates is electron-rich; these intermediates will act as the nucleophile. Hence, the higher the Fukui (+) value, the easier the site is to react with the O atom on *CO and *OCCO. As shown in **Table 4.4.1**, the Fukui (+) values increased gradually from Li^+ to Cs^+ as the size and CN increased. The Li^+ on $[Li(H_2O)_4]^+$ has the smallest Fukui (+) of 0.016 on Li^+, while the 6-coordinted $[Na(H_2O)_6]^+$ has a Fukui (+) of 0.064 on the Na^+ centre. For the$[K(H_2O)_7]^+$ and $[Cs(H_2O)_8]^+$, the K^+ and Cs^+ centre have a a larger Fukui (+) of 0.079 and 0.133, respectively. The smaller Fukui (+) on $[Li(H_2O)_4]^+$ indicates that the Li^+ on $[Li(H_2O)_4]^+$ is less reactive to the intermediate O atom with lone pair electrons. In contrast, the Na^+, K^+, and Cs^+ ions with higher CN values have significantly larger Fukui (+) values, especially the Fukui (+) value of Cs^+ on $[Cs(H_2O)_8]^+$, which is greater than 0.1, suggesting that Cs^+ possesses high reactivity towards nucleophiles.

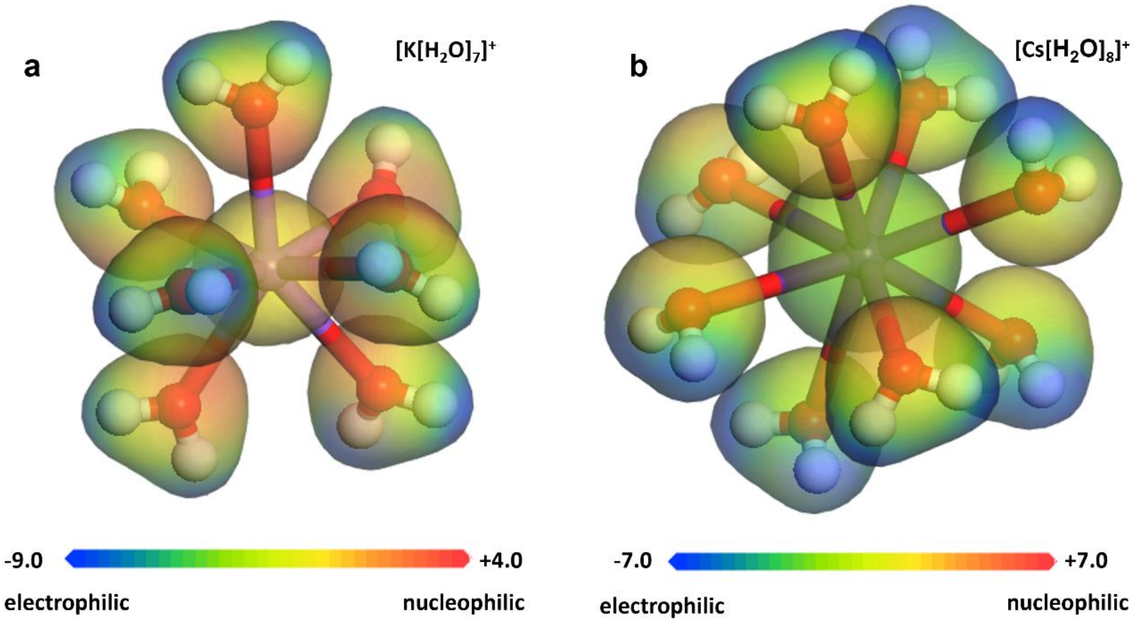

Figure 4.4.2 The charge distribution of (a) $[K(H_2O)_7]^+$ and (b) $[Cs(H_2O)_8]^+$.

On the other hand, the charge distribution analysis (**Figures 4.4.1** and **4.4.2**) reveals that the Li^+ on $[Li(H_2O)_4]^+$ is slightly nucleophilic (electron-rich) due to the strong electrostatic interaction between the cation and coordinated water molecules. Whereas the electrophilic (electron deficient) properties of Na^+, K^+ and Cs^+ on $[Na(H_2O)_6]^+$, $[K(H_2O)_7]^+$ and $[Cs(H_2O)_8]^+$ persevered because of the weaker cation solvation. It is also worth noting that the H atom on the water molecule is also electron-deficient since the O atom is withdrawing electrons from the H atom. In particular, the H atoms carry greater electrophilic character than the cation center. These electron-deficient H atoms in the coordinated water molecules exhibit enhanced acidity due to polarization induced by the cation. This implied that the O-H bond on coordinated water molecules is susceptible to bond cleavage, allowing the H atoms to serve as proton donors for the protonation processes.

4.5 Summary

As discussed in the previous Chapter, the AM^+ can act as a promoter for the CO_2RR electrocatalytic reaction, especially for the formation of C_{2+} products. Although our study demonstrated the direct stabilization effects of cation-intermediate interactions, the literature indicates that the solvation of cations also plays a significant role in the CO_2RR process. This work investigates the aqueous solvation of 1st-row AM^+ (Li^+, Na^+, $K^{+,}$ and Cs^+) via MD and DFT methods. The MD simulations revealed that the CN of AM^+ in aqueous solution increases from 4 to 8 when the cation is changed from Li^+ to Cs^+. The first peak at the RDF curve also displayed a sharp peak for the smaller Li^+ and Na^+ cations, suggesting that the first solvation shell of Li^+ and Na^+ cations is relatively well-defined with a complete depletion of H_2O molecules between shells. Whereas the broader first peak at the RDF curve indicates an unstructured and diffuse solvation shell for the larger K^+ and Cs^+.

Furthermore, the DFT calculation with an implicit solvation model was used to determine the structure of solvated cations. The calculation results showed that the 4-coordinated $[Li(H_2O)_4]^+$ adopted a tetrahedral-like structure with an average Li^+–O bond length of 1.97 Å. While the 6-coordination octahedral-like $[Na(H_2O)_6]^+$ has an average Na^+–O bond length of 2.43 Å. For K^+ and Cs^+ cations, the weak cation-water interaction results in an unstructured first solvation shell. The further charge distribution analysis showed that the trend of reactivity (react with nucleophiles) of the cation centre is $[Li(H_2O)_4]^+ < [Na(H_2O)_6]^+ < [K(H_2O)_7]^+ < [Cs(H_2O)_8]^+$. Especially the Li^+ on $[Li(H_2O)_4]^+$ is slightly nucleophilic (electron-rich) due to the strong electrostatic interaction.

Chapter 5. Conclusion and Outlook

5.1 Conclusion

The CO_2RR is a promising approach for achieving sustainable development. By utilizing renewable energy sources, the CO_2RR can produce a range of chemicals and fuels from CO_2, thereby mitigating greenhouse gas emissions and reducing reliance on fossil fuels. Unfortunately, the selective formation of multi-carbon products remains a significant challenge due to complex reaction pathways and sluggish C–C coupling on the C_2 pathway. These multi-carbon products are particularly valuable due to their wide applications in the chemical and fuel industries, making the efficient production of multi-carbon products crucial for advancing sustainable technologies. In this regard, the cation effect has emerged as a crucial factor in modulating the performance of CO_2RR electrocatalysis, as it can alter the electrochemical environment and influence the adsorption strength of intermediates. In particular, the cation can enhance the formation of C_2 products by facilitating C–C coupling on the metal surface. Therefore, we have employed DFT calculations to investigate the direct effects of cations on the NM surfaces during CO dimerization. Through the calculation of intermediate adsorption energies, energy barrier, CO dimerization reaction energy, cation-dimer stabilization energy, and electronic properties, we revealed the role of direct cation-dimer coordination in promoting the *OCCO formation on Cu and Pt surfaces. The calculation results demonstrated that the larger direct cation stabilization occurred on the Cu(100) surface, with smaller AM^+ facilitated by *OCCO formation. Further electronic analysis showed that this promotion of *OCCO formation can be attributed to the enhancement of charge transfer from the Cu metal surface to the adsorbed *OCCO intermediate. At the same time, the DOS also suggested that effective charge transfer via p-d orbital coupling between the chemisorbed *OCCO and the Cu surface facilitates *OCCO stabilization. Based on this, we believe this work can provide a significant advancement by offering valuable insights into the cation effect on enhancing C_2 product formation, thereby aiding the production of C_2 products via CO_2RR.

On the other hand, the solvation of cations is one of the most important electrolyte properties in solution. Studies have demonstrated that cation solvation at the electrolyte-electrode interface also plays a vital role during the CO_2RR process. Based on that, MD simulations and DFT calculations were used to study the solvation of AM^+ in aqueous solution. The RDF showed that CN of AM^+ in aqueous solution increases from 4 to 8 when changing the cation from Li^+ to Cs^+. In addition, the RDF curve in smaller Li^+ and Na^+ cations indicated a well-defined first solvation shell, and the H_2O between the first and second solvation shell is completely depleted. In contrast, unstructured and diffuse solvation shells were observed around the K^+ and Cs^+ cations, which have larger ionic radii. The structures of the solvated cations were investigated using DFT with an implicit solvation model and dispersion corrections. The calculations revealed that the $[Li(H_2O)_4]^+$ ion adopted a tetrahedral-like structure, characterized by an average Li^+–O bond length of 1.97 Å. An octahedral-like structure was observed from the $[Na(H_2O)_6]^+$ with an average Na^+–O bond length of 2.43 Å. Moreover, an unstructured first solvation shell was observed for the larger K^+ and Cs^+ cations due to the weak cation-water interaction, where the K^+–O bond length of 2.80 Å and Cs^+–O bond length of 3.29 Å were determined. Lastly, Fukui indices have been employed to predict the reactivity of solvated cations in aqueous solution. The Fukui indices suggested that the trend of reactivity (react with nucleophiles) of the cation centre is $[Li(H_2O)_4]^+ < [Na(H_2O)_6]^+ < [K(H_2O)_7]^+ < [Cs(H_2O)_8]^+$, in which the Li^+

centre is slightly nucleophilic (electron-rich) due to the strong electrostatic interaction.

5.2 Outlook

The electrochemical CO_2RR is considered an essential cornerstone technology for a sustainable future, offering a pathway to address climate change and achieve carbon neutrality. The current development of electrochemical CO_2RR toward converting CO_2 to C_1 products is relatively advanced, but achieving high selectivity, especially toward C_2 product formation, remains challenging. Recently, numerous efforts have been devoted to addressing the low C_2 product formation in electrochemical CO_2RR, including utilising neighbouring-site effects on ACs and optimising the electrolyte through cation effects. Neighbouring site effects in ACs play a crucial role not only in enhancing C–C coupling for C_{2+} products in SACs but also in enabling tandem catalysis in ACs with dual-site configurations. Based on that, leveraging neighbouring site effects in ACs for CO_2RR is highly promising, with anticipated breakthroughs in dual-atom catalysts (DACs) and heterostructure SACs to overcome current limitations in C_{2+} products formation and long-term stability. Moreover, combining these effects with other strategies, such as electrolyte engineering, can create synergistic microenvironments that further facilitate C–C coupling and the formation of C_{2+} products.

On the other hand, electrocatalytic CO_2 reduction to long-chain hydrocarbons (e.g., C_{3+} products) is also a promising, sustainable method for producing valuable chemicals and high-energy-density fuels. However, the formation of long-chain hydrocarbons via CO_2RR faces challenges in product yield and selectivity, and the complex mechanisms for synthesizing these hydrocarbons also make it difficult to design optimal catalysts. To overcome the low product yield of forming long-chain hydrocarbons, several strategies have been explored, focusing on further enhancing the C–C coupling ability in electrocatalysis. The production of long-chain hydrocarbons could be inspired by the thermocatalytic Fischer–Tropsch synthesis (FTS) using cobalt-based catalysts. Besides, natural catalysts, such as coenzymes, can effectively produce long-chain hydrocarbons at ambient conditions via multi-metal active sites, which inspire biomimetic CO_2RR for efficient C–C coupling.

Future work on electrolytes for CO_2RR should focus on developing a wider variety of electrolyte systems. Recent studies have demonstrated that non-metallic organic cations, such as alkylammonium, imidazolium, pyridinium, and tetraalkylammonium, can have a profound effect on CO_2RR performances, suggesting that these organic cations can be designed to optimise the reaction environment for CO_2RR. In particular, unlike simple metal cations, organic cations with various carbon chains are synthetically tunable, offering a broader design space for electrolyte design. Although recent studies have demonstrated that the length of carbon chains on organic cations can influence product selectivity in CO_2RR, the understanding of the correlations between molecular features of cations (molecular structure, functional groups, and charge distribution) and CO_2RR performance remains incomplete. Moreover, the production of long-chain hydrocarbon products via CO_2RR (such as C_{3+} products) remains highly limited. Based on that, it is essential to design efficient and selective electrocatalysts for CO_2RR to produce larger molecules with higher value and broader applications.

Beyond these approaches, additional engineering strategies can be employed to accelerate the progress in C_{2+} production. For example, electrocatalyst modifications, such as Cu doping with Ag, Sn, or halogens, can create heterogeneous surfaces that favour C–C coupling by tuning oxidation states and exposing specific facets. In particular, integrating machine learning (ML) with high-throughput screening to accelerate catalyst discovery could significantly enhance the development of optimised alloys and heterostructures for CO_2RR. These data-driven approaches can be used to explore the potential of earth-abundant materials for CO_2RR. Especially, sustainability-focused innovations emphasise earth-abundant materials to minimise environmental impact during catalyst synthesis and operation. Earth-abundant metals are increasingly prioritised over scarce noble metals owing to their lower costs and widespread availability, which reduces the overall carbon footprint of CO_2RR systems. Metal-free carbon-based electrocatalysts can also be considered as an alternative that offers greater environmental benefits by eliminating metal usage.

List of Publications

1. **H. H. Wong**, M. Sun, T. Wu, L. Lu, Q. Lu, B. Chen, C. Hei Chan and B. Huang, Direct Cation Stabilization Effects of CO Dimerization for Boosting C_2 Pathways of CO_2 Reduction on Noble Metal Surfaces. *Adv. Energy Sustainability Res.* **2024**, *5* (8), 2400110.

2. **H. H. Wong**, M. Sun, T. Wu, C. H. Chan, L. Lu, Q. Lu, B. Chen and B. Huang, Neighboring effect in single-atom catalysts for the electrochemical carbon dioxide reduction reaction. *eScience* **2024**, *4* (1), 100140.

3. **H. H. Wong**, M. Sun and B. Huang, Synergistic Effect of Graphdiyne-based Electrocatalysts. *Chem. Res. Chin. Univ.* **2021**, *37* (6), 1242-1256.

4. **H. H. Wong**, M. Sun and B. Huang, Electronic modification in graphdiyne for future electrocatalytic applications. *2D Mater.* **2021**, *8* (4), 044009.

5. C. Hei Chan, **H. H. Wong**, S. Liang, M. Sun, T. Wu, Q. Lu, L. Lu, B. Chen and B. Huang, Electrolyte Developments for All-Solid-State Lithium Batteries: Classifications, Recent Advances and Synthesis Methods. *Batteries Supercaps* **2024**, *7* (12), e202400432.

6. M. Sun, **H. H. Wong**, T. Wu, A. W. Dougherty and B. Huang, Entanglement of Spatial and Energy Segmentation for C_1 Pathways in CO_2 Reduction on Carbon Skeleton Supported Atomic Catalysts. *Adv. Energy Mater.* **2022**, *12* (14), 2103781.

7. M. Sun, **H. H. Wong**, T. Wu, Q. Lu, L. Lu, C. H. Chan, B. Chen, A. W. Dougherty and B. Huang, Double-Dependence Correlations in Graphdiyne-Supported Atomic Catalysts to Promote CO_2RR toward the Generation of C_2 Products. *Adv. Energy Mater.* **2023**, *13* (7), 2203858.

References

[1] T. A. Boden, R. J. Andres, G. Marland, United States 2015.

[2] R. Karan, R. Bhatia, R. K. Rawal, in *Green Sustainable Process for Chemical and Environmental Engineering and Science*, (Eds: Inamuddin, R. Boddula, A. M. Asiri, M. M. Rahman), Elsevier, 2021.

[3] J. C. Arango-Daza, M. A. Rivero-Crespo, *Chem. Eur. J.* **2024**, 30, e202400443.

[4] D. A. Pirgach, F. M. Miloserdov, D. S. van Es, P. C. A. Bruijnincx, J. H. Bitter, *ChemCatChem* **2024**, 17, e202401473.

[5] M. J. Hülsey, C. W. Lim, N. Yan, *Chem. Sci.* **2020**, 11, 1456.

[6] L.-N. Zhang, R. Li, H.-Y. Zang, H.-Q. Tan, Z.-H. Kang, Y.-H. Wang, Y.-G. Li, *Energy Environ. Sci.* **2021**, 14, 6191.

[7] J. Zhu, L. Hu, P. Zhao, L. Y. S. Lee, K.-Y. Wong, *Chem. Rev.* **2020**, 120, 851.

[8] Y. Feng, H. Yang, X. Wang, C. Hu, H. Jing, J. Cheng, *Int. J. Hydrogen Energy* **2022**, 47, 17946.

[9] M. Tahir, L. Pan, F. Idrees, X. Zhang, L. Wang, J.-J. Zou, Z. L. Wang, *Nano Energy* **2017**, 37, 136.

[10] X. Tian, X. F. Lu, B. Y. Xia, X. W. Lou, *Joule* **2020**, 4, 45.

[11] S. Liu, A. Wang, Y. Liu, W. Zhou, H. Wen, H. Zhang, K. Sun, S. Li, J. Zhou, Y. Wang, J. Jiang, B. Li, *Adv. Sci.* **2024**, 11, 2308040.

[12] H. Jin, S. S. Kim, S. Venkateshalu, J. Lee, K. Lee, K. Jin, *Adv. Sci.* **2023**, 10, 2300951.

[13] X. Long, F. Huang, Z. Yao, P. Li, T. Zhong, H. Zhao, S. Tian, D. Shu, C. He, *Small* **2024**, 20, 2400551.

[14] S. Nitopi, E. Bertheussen, S. B. Scott, X. Liu, A. K. Engstfeld, S. Horch, B.

Seger, I. E. L. Stephens, K. Chan, C. Hahn, J. K. Nørskov, T. F. Jaramillo, I. Chorkendorff, *Chem. Rev.* **2019**, 119, 7610.

[15] D. A. Lowy, J. R. Melendez, B. Mátyás, *Renew. Sustain. Energy Rev.* **2024**, 194, 114300.

[16] D. D. Zhu, J. L. Liu, S. Z. Qiao, *Adv. Mater.* **2016**, 28, 3423.

[17] L. Zhang, Z.-J. Zhao, J. Gong, *Angew. Chem. Int. Ed.* **2017**, 56, 11326.

[18] K. Li, B. Peng, T. Peng, *ACS Catal.* **2016**, 6, 7485.

[19] Q. Lu, F. Jiao, *Nano Energy* **2016**, 29, 439.

[20] S. Roy, A. Cherevotan, S. C. Peter, *ACS Energy Lett.* **2018**, 3, 1938.

[21] X.-M. Hu, M. H. Rønne, S. U. Pedersen, T. Skrydstrup, K. Daasbjerg, *Angew. Chem. Int. Ed.* **2017**, 56, 6468.

[22] J. S. Yoo, R. Christensen, T. Vegge, J. K. Nørskov, F. Studt, *ChemSusChem* **2016**, 9, 358.

[23] L. D. Ramírez-Valencia, E. Bailón-García, F. Carrasco-Marín, A. F. Pérez-Cadenas, *Catalysts* **2021**, 11.

[24] K. J. P. Schouten, Z. Qin, E. Pérez Gallent, M. T. M. Koper, *J. Am. Chem. Soc.* **2012**, 134, 9864.

[25] Y. Zheng, A. Vasileff, X. Zhou, Y. Jiao, M. Jaroniec, S.-Z. Qiao, *J. Am. Chem. Soc.* **2019**, 141, 7646.

[26] S. Dhakar, S. Sharma, *J. Phys. Chem. C* **2024**, 128, 4862.

[27] J. Dai, J. Zhu, Y. Xu, X. Liu, D. Zhu, G. Xu, H. Liu, G. Li, *ChemSusChem* **2024**, 18, e202402184.

[28] T. K. Todorova, M. W. Schreiber, M. Fontecave, *ACS Catal.* **2020**, 10, 1754.

[29] D. Ma, C. Zhi, Y. Zhang, J. Chen, Y. Zhang, J.-W. Shi, *ACS Nano* **2024**, 18,

21714.

[30] Y. Y. Birdja, E. Pérez-Gallent, M. C. Figueiredo, A. J. Göttle, F. Calle-Vallejo, M. T. M. Koper, *Nat. Energy* **2019**, 4, 732.

[31] D. Ren, Y. Deng, A. D. Handoko, C. S. Chen, S. Malkhandi, B. S. Yeo, *ACS Catal.* **2015**, 5, 2814.

[32] D. A. Torelli, S. A. Francis, J. C. Crompton, A. Javier, J. R. Thompson, B. S. Brunschwig, M. P. Soriaga, N. S. Lewis, *ACS Catal.* **2016**, 6, 2100.

[33] X. Yuan, L. Zhang, L. Li, H. Dong, S. Chen, W. Zhu, C. Hu, W. Deng, Z.-J. Zhao, J. Gong, *J. Am. Chem. Soc.* **2019**, 141, 4791.

[34] W. O. Silva, G. C. Silva, R. F. Webster, T. M. Benedetti, R. D. Tilley, E. A. Ticianelli, *ChemElectroChem* **2019**, 6, 4626.

[35] T.-T. Zhuang, Y. Pang, Z.-Q. Liang, Z. Wang, Y. Li, C.-S. Tan, J. Li, C. T. Dinh, P. De Luna, P.-L. Hsieh, T. Burdyny, H.-H. Li, M. Liu, Y. Wang, F. Li, A. Proppe, A. Johnston, D.-H. Nam, Z.-Y. Wu, Y.-R. Zheng, A. H. Ip, H. Tan, L.-J. Chen, S.-H. Yu, S. O. Kelley, D. Sinton, E. H. Sargent, *Nat. Catal.* **2018**, 1, 946.

[36] M. M. Abdelnaby, K. Liu, K. Hassanein, Z. Yin, *ChemNanoMat* **2021**, 7, 969.

[37] K. U. D. Calvinho, A. B. Laursen, K. M. K. Yap, T. A. Goetjen, S. Hwang, N. Murali, B. Mejia-Sosa, A. Lubarski, K. M. Teeluck, E. S. Hall, E. Garfunkel, M. Greenblatt, G. C. Dismukes, *Energy Environ. Sci.* **2018**, 11, 2550.

[38] X.-F. Yang, A. Wang, B. Qiao, J. Li, J. Liu, T. Zhang, *Acc. Chem. Res.* **2013**, 46, 1740.

[39] Z. W. Chen, L. X. Chen, C. C. Yang, Q. Jiang, *J. Mater. Chem. A* **2019**, 7, 3492.

[40] H. Zhang, X. F. Lu, Z.-P. Wu, X. W. D. Lou, *ACS Cent. Sci.* **2020**, 6, 1288.

[41] P. Su, K. Iwase, S. Nakanishi, K. Hashimoto, K. Kamiya, *Small* **2016**, 12, 6083.

[42] X. Zhang, Z. Wu, X. Zhang, L. Li, Y. Li, H. Xu, X. Li, X. Yu, Z. Zhang, Y. Liang, H. Wang, *Nat. Commun.* **2017**, 8, 14675.

[43] X. Li, W. Bi, M. Chen, Y. Sun, H. Ju, W. Yan, J. Zhu, X. Wu, W. Chu, C. Wu, Y. Xie, *J. Am. Chem. Soc.* **2017**, 139, 14889.

[44] K. Jiang, S. Siahrostami, A. J. Akey, Y. Li, Z. Lu, J. Lattimer, Y. Hu, C. Stokes, M. Gangishetty, G. Chen, Y. Zhou, W. Hill, W.-B. Cai, D. Bell, K. Chan, J. K. Nørskov, Y. Cui, H. Wang, *Chem* **2017**, 3, 950.

[45] C. Zhao, X. Dai, T. Yao, W. Chen, X. Wang, J. Wang, J. Yang, S. Wei, Y. Wu, Y. Li, *J. Am. Chem. Soc.* **2017**, 139, 8078.

[46] X. Wang, Z. Chen, X. Zhao, T. Yao, W. Chen, R. You, C. Zhao, G. Wu, J. Wang, W. Huang, J. Yang, X. Hong, S. Wei, Y. Wu, Y. Li, *Angew. Chem. Int. Ed.* **2018**, 57, 1944.

[47] Y. Pan, R. Lin, Y. Chen, S. Liu, W. Zhu, X. Cao, W. Chen, K. Wu, W.-C. Cheong, Y. Wang, L. Zheng, J. Luo, Y. Lin, Y. Liu, C. Liu, J. Li, Q. Lu, X. Chen, D. Wang, Q. Peng, C. Chen, Y. Li, *J. Am. Chem. Soc.* **2018**, 140, 4218.

[48] C. Zhang, S. Yang, J. Wu, M. Liu, S. Yazdi, M. Ren, J. Sha, J. Zhong, K. Nie, A. S. Jalilov, Z. Li, H. Li, B. I. Yakobson, Q. Wu, E. Ringe, H. Xu, P. M. Ajayan, J. M. Tour, *Adv. Energy Mater.* **2018**, 8, 1703487.

[49] F. Pan, H. Zhang, K. Liu, D. Cullen, K. More, M. Wang, Z. Feng, G. Wang, G. Wu, Y. Li, *ACS Catal.* **2018**, 8, 3116.

[50] K. Jiang, S. Siahrostami, T. Zheng, Y. Hu, S. Hwang, E. Stavitski, Y. Peng, J. Dynes, M. Gangisetty, D. Su, K. Attenkofer, H. Wang, *Energy Environ. Sci.* **2018**, 11, 893.

[51] C. Yan, H. Li, Y. Ye, H. Wu, F. Cai, R. Si, J. Xiao, S. Miao, S. Xie, F. Yang, Y.

Li, G. Wang, X. Bao, *Energy Environ. Sci.* **2018**, 11, 1204.

[52] F. Yang, P. Song, X. Liu, B. Mei, W. Xing, Z. Jiang, L. Gu, W. Xu, *Angew. Chem. Int. Ed.* **2018**, 57, 12303.

[53] Y. Wang, Z. Chen, P. Han, Y. Du, Z. Gu, X. Xu, G. Zheng, *ACS Catal.* **2018**, 8, 7113.

[54] C. Lu, J. Yang, S. Wei, S. Bi, Y. Xia, M. Chen, Y. Hou, M. Qiu, C. Yuan, Y. Su, F. Zhang, H. Liang, X. Zhuang, *Adv. Funct. Mater.* **2019**, 29, 1806884.

[55] T. Möller, W. Ju, A. Bagger, X. Wang, F. Luo, T. Ngo Thanh, A. S. Varela, J. Rossmeisl, P. Strasser, *Energy Environ. Sci.* **2019**, 12, 640.

[56] H. Yang, Y. Wu, G. Li, Q. Lin, Q. Hu, Q. Zhang, J. Liu, C. He, *J. Am. Chem. Soc.* **2019**, 141, 12717.

[57] P. Lu, Y. Yang, J. Yao, M. Wang, S. Dipazir, M. Yuan, J. Zhang, X. Wang, Z. Xie, G. Zhang, *Appl. Catal. B* **2019**, 241, 113.

[58] Y. Cheng, S. Zhao, H. Li, S. He, J.-P. Veder, B. Johannessen, J. Xiao, S. Lu, J. Pan, M. F. Chisholm, S.-Z. Yang, C. Liu, J. G. Chen, S. P. Jiang, *Appl. Catal. B* **2019**, 243, 294.

[59] X. Zu, X. Li, W. Liu, Y. Sun, J. Xu, T. Yao, W. Yan, S. Gao, C. Wang, S. Wei, Y. Xie, *Adv. Mater.* **2019**, 31, 1808135.

[60] Y. Wu, Z. Jiang, X. Lu, Y. Liang, H. Wang, *Nature* **2019**, 575, 639.

[61] D. Karapinar, N. T. Huan, N. Ranjbar Sahraie, J. Li, D. Wakerley, N. Touati, S. Zanna, D. Taverna, L. H. Galvão Tizei, A. Zitolo, F. Jaouen, V. Mougel, M. Fontecave, *Angew. Chem. Int. Ed.* **2019**, 58, 15098.

[62] H. Xu, D. Rebollar, H. He, L. Chong, Y. Liu, C. Liu, C.-J. Sun, T. Li, J. V. Muntean, R. E. Winans, D.-J. Liu, T. Xu, *Nat. Energy* **2020**, 5, 623.

[63] L. Han, S. Song, M. Liu, S. Yao, Z. Liang, H. Cheng, Z. Ren, W. Liu, R. Lin, G. Qi, X. Liu, Q. Wu, J. Luo, H. L. Xin, *J. Am. Chem. Soc.* **2020**, 142, 12563.

[64] L. Ma, W. Hu, B. Mei, H. Liu, B. Yuan, J. Zang, T. Chen, L. Zou, Z. Zou, B. Yang, Y. Yu, J. Ma, Z. Jiang, K. Wen, H. Yang, *ACS Catal.* **2020**, 10, 4534.

[65] K. Zhao, X. Nie, H. Wang, S. Chen, X. Quan, H. Yu, W. Choi, G. Zhang, B. Kim, J. G. Chen, *Nat. Commun.* **2020**, 11, 2455.

[66] J. Ma, H. Zhu, Y. Zheng, *Ionics* **2021**, 27, 2583.

[67] Y. Cai, J. Fu, Y. Zhou, Y.-C. Chang, Q. Min, J.-J. Zhu, Y. Lin, W. Zhu, *Nat. Commun.* **2021**, 12, 586.

[68] Y.-B. Chang, C. Zhang, X.-L. Lu, W. Zhang, T.-B. Lu, *Nano Res.* **2022**, 15, 195.

[69] W. Xie, S. Zhang, Y. Ni, G. Shi, J. Li, X. Fu, X. Chen, M. Yuan, M. Wang, *Adv. Energy Sustainability Res.* **2021**, 2, 2100037.

[70] H. Gu, L. Zhong, G. Shi, J. Li, K. Yu, J. Li, S. Zhang, C. Zhu, S. Chen, C. Yang, Y. Kong, C. Chen, S. Li, J. Zhang, L. Zhang, *J. Am. Chem. Soc.* **2021**, 143, 8679.

[71] G. Li, Y. Li, H. Liu, Y. Guo, Y. Li, D. Zhu, *Chem. Commun.* **2010**, 46, 3256.

[72] H. H. Wong, M. Sun, B. Huang, *2D Mater.* **2021**, 8, 044009.

[73] S. Yu, J. Chen, C. Chen, M. Zhou, L. Shen, B. Li, H. Lin, *Coord. Chem. Rev.* **2023**, 482, 215082.

[74] Y. Jiao, A. Du, S. C. Smith, Z. Zhu, S. Z. Qiao, *J. Mater. Chem. A* **2015**, 3, 6767.

[75] T. Lu, X. Hu, J. He, R. Li, J. Gao, Q. Lv, Z. Yang, S. Cui, C. Huang, *Nano Energy* **2021**, 85, 106024.

[76] Q. Lv, W. Si, Z. Yang, N. Wang, Z. Tu, Y. Yi, C. Huang, L. Jiang, M. Zhang, J. He, Y. Long, *ACS Appl. Mater. Interfaces* **2017**, 9, 29744.

[77] G. Wang, W. Cai, T. Fan, Y. Ji, *Appl. Surf. Sci.* **2021**, 570, 151109.

[78] T. Liu, X. Hao, J. Liu, P. Zhang, J. Chang, H. Shang, X. Liu, *Int. J. Mol. Sci.* **2023**, 24, 16813.

[79] S. Zhang, H. Du, J. He, C. Huang, H. Liu, G. Cui, Y. Li, *ACS Appl. Mater. Interfaces* **2016**, 8, 8467.

[80] Z. Feng, Y. Ma, Y. Li, R. Li, J. Liu, H. Li, Y. Tang, X. Dai, *Phys. E: Low-Dimens. Syst. Nanostructures* **2019**, 114, 113590.

[81] C. Xing, Y. Xue, B. Huang, H. Yu, L. Hui, Y. Fang, Y. Liu, Y. Zhao, Z. Li, Y. Li, *Angew. Chem. Int. Ed.* **2019**, 58, 13897.

[82] H. Du, Z. Zhang, J. He, Z. Cui, J. Chai, J. Ma, Z. Yang, C. Huang, G. Cui, *Small* **2017**, 13, 1702277.

[83] Z. Yang, W. Cui, K. Wang, Y. Song, F. Zhao, N. Wang, Y. Long, H. Wang, C. Huang, *Chem. - Eur. J.* **2019**, 25, 5643.

[84] F. Kong, Y. Yue, Q. Li, S. Ren, *Nanomaterials* **2021**, 11, 1161.

[85] M. Dehkhodaei, A. Reisi-Vanani, *Surf. Interfaces* **2022**, 31, 102031.

[86] J. Qi, Q. Ge, Z. Wang, J. Wu, Y. Wang, T. Gao, *Inorg. Chem.* **2024**, 63, 766.

[87] J. Gu, S. Magagula, J. Zhao, Z. Chen, *Small Methods* **2019**, 3, 1800550.

[88] Y. Zhao, N. Yang, H. Yao, D. Liu, L. Song, J. Zhu, S. Li, L. Gu, K. Lin, D. Wang, *J. Am. Chem. Soc.* **2019**, 141, 7240.

[89] B. K. Das, D. Sen, K. K. Chattopadhyay, *Phys. Chem. Chem. Phys.* **2016**, 18, 2949.

[90] N. Wang, X. Li, Z. Tu, F. Zhao, J. He, Z. Guan, C. Huang, Y. Yi, Y. Li, *Angew. Chem. Int. Ed.* **2018**, 57, 3968.

[91] C. Fu, Y. Li, H. Wei, *Phys. Chem. Chem. Phys.* **2021**, 23, 17683.

[92] C. Fu, Y. Li, H. Wei, *Phys. Chem. Chem. Phys.* **2022**, 24, 19817.

[93] Z. Feng, Y. Ma, Y. Li, R. Li, Y. Tang, X. Dai, *Phys. Chem. Chem. Phys.* **2020**, 22, 1493.

[94] J. Zhao, Z. Chen, J. Zhao, *J. Mater. Chem. A* **2019**, 7, 4026.

[95] F. Xu, D. Wu, Z. Wang, A. Ma, F. Wu, H. Xu, G. Fan, *Appl. Surf. Sci.* **2023**, 631, 157505.

[96] B. Li, S. Yu, M. Zhou, C. Chen, C. Lai, M. Zhang, H. Lin, *J. Mater. Chem. A* **2022**, 10, 3905.

[97] Y. Xue, B. Huang, Y. Yi, Y. Guo, Z. Zuo, Y. Li, Z. Jia, H. Liu, Y. Li, *Nat. Commun.* **2018**, 9, 1460.

[98] M. Sun, T. Wu, Y. Xue, A. W. Dougherty, B. Huang, Y. Li, C.-H. Yan, *Nano Energy* **2019**, 62, 754.

[99] J. He, S. Y. Ma, P. Zhou, C. X. Zhang, C. He, L. Z. Sun, *J. Phys. Chem. C* **2012**, 116, 26313.

[100] T. He, S. K. Matta, G. Will, A. Du, *Small Methods* **2019**, 3, 1800419.

[101] X. Zhai, H. Yan, G. Ge, J. Yang, F. Chen, X. Liu, D. Yang, L. Li, J. Zhang, *Appl. Surf. Sci.* **2020**, 506, 144941.

[102] A. H. Mashhadzadeh, A. M. Vahedi, M. Ardjmand, M. G. Ahangari, *Superlattices Microstruct.* **2016**, 100, 1094.

[103] Z. Lu, S. Li, P. Lv, C. He, D. Ma, Z. Yang, *Appl. Surf. Sci.* **2016**, 360, 1.

[104] L. Li, K. Yuan, Y. Chen, *Acc. Mater. Res.* **2022**, 3, 584.

[105] H. Jeong, S. Shin, H. Lee, *ACS Nano* **2020**, 14, 14355.

[106] H. H. Wong, M. Sun, B. Huang, *Chem. Res. Chin. Univ.* **2021**, 37, 1242.

[107] Y. Ren, C. Yu, X. Tan, Q. Wei, Z. Wang, L. Ni, L. Wang, J. Qiu, *Energy Environ. Sci.* **2022**, 15, 2776.

[108] L.-L. Shi, M. Li, B. You, R.-Z. Liao, *Inorg. Chem.* **2022**, 61, 16549.

[109] C. Hu, Y. Xiao, Y. Zou, L. Dai, *Electrochem. Energy Rev.* **2018**, 1, 84.

[110] X. Liu, L. Dai, *Nat. Rev. Mater.* **2016**, 1, 16064.

[111] D. M. Fernandes, A. F. Peixoto, C. Freire, *Dalton Trans.* **2019**, 48, 13508.

[112] H. Kiuchi, R. Shibuya, T. Kondo, J. Nakamura, H. Niwa, J. Miyawaki, M. Kawai, M. Oshima, Y. Harada, *Nanoscale Res. Lett.* **2016**, 11, 127.

[113] J. Wu, R. M. Yadav, M. Liu, P. P. Sharma, C. S. Tiwary, L. Ma, X. Zou, X.-D. Zhou, B. I. Yakobson, J. Lou, P. M. Ajayan, *ACS Nano* **2015**, 9, 5364.

[114] P. P. Sharma, J. Wu, R. M. Yadav, M. Liu, C. J. Wright, C. S. Tiwary, B. I. Yakobson, J. Lou, P. M. Ajayan, X.-D. Zhou, *Angew. Chem. Int. Ed.* **2015**, 54, 13701.

[115] J. Wu, S. Ma, J. Sun, J. I. Gold, C. Tiwary, B. Kim, L. Zhu, N. Chopra, I. N. Odeh, R. Vajtai, A. Z. Yu, R. Luo, J. Lou, G. Ding, P. J. A. Kenis, P. M. Ajayan, *Nat. Commun.* **2016**, 7, 13869.

[116] B. Li, X. Sun, D. Su, *Phys. Chem. Chem. Phys.* **2015**, 17, 6691.

[117] T. Kondo, S. Casolo, T. Suzuki, T. Shikano, M. Sakurai, Y. Harada, M. Saito, M. Oshima, M. I. Trioni, G. F. Tantardini, J. Nakamura, *Phys. Rev. B* **2012**, 86, 035436.

[118] J. C. Meyer, S. Kurasch, H. J. Park, V. Skakalova, D. Künzel, A. Groß, A. Chuvilin, G. Algara-Siller, S. Roth, T. Iwasaki, U. Starke, J. H. Smet, U. Kaiser, *Nat. Mater.* **2011**, 10, 209.

[119] S.-S. Yu, W.-T. Zheng, *Nanoscale* **2010**, 2, 1069.

[120] H. B. Yang, S.-F. Hung, S. Liu, K. Yuan, S. Miao, L. Zhang, X. Huang, H.-Y. Wang, W. Cai, R. Chen, J. Gao, X. Yang, W. Chen, Y. Huang, H. M. Chen, C. M. Li, T. Zhang, B. Liu, *Nat. Energy* **2018**, 3, 140.

[121] L. Li, Y. Huang, Y. Li, *EnergyChem* **2020**, 2, 100024.

[122] S. Back, J. Lim, N.-Y. Kim, Y.-H. Kim, Y. Jung, *Chem. Sci.* **2017**, 8, 1090.

[123] T. Liu, G. Wang, X. Bao, *J. Phys. Chem. C* **2021**, 125, 26013.

[124] Q. Zhou, Z. Fu, Y. Tang, H. Zhang, C. Wang, *Phys. E: Low-Dimens. Syst. Nanostructures* **2014**, 60, 133.

[125] U. I. Kramm, I. Herrmann-Geppert, J. Behrends, K. Lips, S. Fiechter, P. Bogdanoff, *J. Am. Chem. Soc.* **2016**, 138, 635.

[126] H. Fei, J. Dong, Y. Feng, C. S. Allen, C. Wan, B. Volosskiy, M. Li, Z. Zhao, Y. Wang, H. Sun, P. An, W. Chen, Z. Guo, C. Lee, D. Chen, I. Shakir, M. Liu, T. Hu, Y. Li, A. I. Kirkland, X. Duan, Y. Huang, *Nat. Catal.* **2018**, 1, 63.

[127] M. Sun, B. Huang, *Nano Energy* **2022**, 99, 107398.

[128] M. Born, R. Oppenheimer, *Ann. Phys.* **1927**, 389, 457.

[129] P. Hohenberg, W. Kohn, *Phys. Rev.* **1964**, 136, B864.

[130] L. H. Thomas, *Math. Proc. Cambridge Philos. Soc.* **1927**, 23, 542.

[131] E. Fermi, *Rend. Accad. Naz. Lincei* **1927**, 6, 32.

[132] W. Kohn, L. J. Sham, *Phys. Rev.* **1965**, 140, A1133.

[133] B.-T. Teng, X.-D. Wen, M. Fan, F.-M. Wu, Y. Zhang, *Phys. Chem. Chem. Phys.* **2014**, 16, 18563.

[134] P. Borlido, T. Aull, A. W. Huran, F. Tran, M. A. L. Marques, S. Botti, *J. Chem. Theory Comput.* **2019**, 15, 5069.

[135] M. A. L. Marques, M. J. T. Oliveira, T. Burnus, *Comput. Phys. Commun.* **2012**, 183, 2272.

[136] D. M. Ceperley, B. J. Alder, *Phys. Rev. Lett.* **1980**, 45, 566.

[137] J. P. Perdew, K. Burke, M. Ernzerhof, *Phys. Rev. Lett.* **1996**, 77, 3865.

[138] J. P. Perdew, J. A. Chevary, S. H. Vosko, K. A. Jackson, M. R. Pederson, D. J. Singh, C. Fiolhais, *Phys. Rev. B* **1992**, 46, 6671.

[139] L. A. Curtiss, P. C. Redfern, K. Raghavachari, *J. Chem. Phys.* **2005**, 123, 124107.

[140] J. P. Perdew, A. Ruzsinszky, G. I. Csonka, O. A. Vydrov, G. E. Scuseria, L. A. Constantin, X. Zhou, K. Burke, *Phys. Rev. Lett.* **2008**, 100, 136406.

[141] S. Śmiga, L. A. Constantin, *J. Phys. Chem. A* **2020**, 124, 5606.

[142] J. P. Perdew, M. Ernzerhof, K. Burke, *J. Chem. Phys.* **1996**, 105, 9982.

[143] P. J. Stephens, F. J. Devlin, C. F. Chabalowski, M. J. Frisch, *J. Phys. Chem.* **1994**, 98, 11623.

[144] J. Paier, M. Marsman, G. Kresse, *J. Chem. Phys.* **2007**, 127, 024103.

[145] W. Gao, T. A. Abtew, T. Cai, Y.-Y. Sun, S. Zhang, P. Zhang, *Solid State Commun.* **2016**, 234-235, 10.

[146] Y. Hori, S. Suzuki, *Bull. Chem. Soc. Jpn.* **1982**, 55, 660.

[147] Y. Hori, A. Murata, R. Takahashi, *J. Chem. Soc., Faraday Trans.* **1989**, 85, 2309.

[148] A. Murata, Y. Hori, *Bull. Chem. Soc. Jpn.* **1991**, 64, 123.

[149] M. R. Singh, Y. Kwon, Y. Lum, J. W. Ager, III, A. T. Bell, *J. Am. Chem. Soc.* **2016**, 138, 13006.

[150] J. N. Mills, I. T. McCrum, M. J. Janik, *Phys. Chem. Chem. Phys.* **2014**, 16, 13699.

[151] D. Gao, I. T. McCrum, S. Deo, Y.-W. Choi, F. Scholten, W. Wan, J. G. Chen, M. J. Janik, B. Roldan Cuenya, *ACS Catal.* **2018**, 8, 10012.

[152] L. D. Chen, M. Urushihara, K. Chan, J. K. Nørskov, *ACS Catal.* **2016**, 6,

7133.

[153] J. Resasco, L. D. Chen, E. Clark, C. Tsai, C. Hahn, T. F. Jaramillo, K. Chan, A. T. Bell, *J. Am. Chem. Soc.* **2017**, 139, 11277.

[154] S. Ringe, E. L. Clark, J. Resasco, A. Walton, B. Seger, A. T. Bell, K. Chan, *Energy Environ. Sci.* **2019**, 12, 3001.

[155] X. Qin, H. A. Hansen, K. Honkala, M. M. Melander, *Nat. Commun.* **2023**, 14, 7607.

[156] M. D. Segall, J. D. L. Philip, M. J. Probert, C. J. Pickard, P. J. Hasnip, S. J. Clark, M. C. Payne, *J. Phys.: Condens. Matter* **2002**, 14, 2717.

[157] J. D. Head, M. C. Zerner, *Chem. Phys. Lett.* **1985**, 122, 264.

[158] D. Vanderbilt, *Phys. Rev. B* **1990**, 41, 7892.

[159] K. M. Gameel, I. M. Sharafeldin, A. U. Abourayya, A. H. Biby, N. K. Allam, *Phys. Chem. Chem. Phys.* **2018**, 20, 25892.

[160] S. Yamagishi, T. Fujimoto, Y. Inada, H. Orita, *J. Phys. Chem. B* **2005**, 109, 8899.

[161] D. Schröder, C. Heinemann, H. Schwarz, J. N. Harvey, S. Dua, S. J. Blanksby, J. H. Bowie, *Chem. - Eur. J.* **1998**, 4, 2550.

[162] A. R. Dixon, T. Xue, A. Sanov, *Angew. Chem. Int. Ed.* **2015**, 54, 8764.

[163] F. Calle-Vallejo, M. T. M. Koper, *Angew. Chem. Int. Ed.* **2013**, 52, 7282.

[164] A. J. Garza, A. T. Bell, M. Head-Gordon, *ACS Catal.* **2018**, 8, 1490.

[165] J. Hussain, H. Jónsson, E. Skúlason, *ACS Catal.* **2018**, 8, 5240.

[166] M. Umeda, Y. Niitsuma, T. Horikawa, S. Matsuda, M. Osawa, *ACS Appl. Energy Mater.* **2020**, 3, 1119.

[167] Y. Qin, C. Xia, T. Wu, J. Zhang, G. Gao, B. Y. Xia, M. L. Coote, S. Ding,

Y. Su, *J. Am. Chem. Soc.* **2024**, 146, 32539.

[168] M. M. Sartin, Z. Yu, W. Chen, F. He, Z. Sun, Y.-X. Chen, W. Huang, *J. Phys. Chem. C* **2018**, 122, 26489.

[169] H. H. Kristoffersen, K. Chan, *J. Catal.* **2021**, 396, 251.

[170] J. Mato, D. Poole, M. S. Gordon, *The Journal of Physical Chemistry A* **2020**, 124, 8209.

[171] S. Hedström, E. C. dos Santos, C. Liu, K. Chan, F. Abild-Pedersen, L. G. M. Pettersson, *J. Phys. Chem. C* **2018**, 122, 12251.

[172] B. Hammer, J. K. Nørskov, *Surf. Sci.* **1995**, 343, 211.

[173] A. Ruban, B. Hammer, P. Stoltze, H. L. Skriver, J. K. Nørskov, *J. Mol. Catal. A: Chem.* **1997**, 115, 421.

[174] J. K. Nørskov, F. Abild-Pedersen, F. Studt, T. Bligaard, *Proc. Natl. Acad. Sci. U.S.A.* **2011**, 108, 937.

[175] M. Ünlü, D. Abbott, N. Ramaswamy, X. Ren, S. Mukerjee, P. A. Kohl, *J. Electrochem. Soc.* **2011**, 158, B1423.

[176] L. Jiao, E. Liu, S. Mukerjee, Q. Jia, *ACS Catal.* **2020**, 10, 11099.

[177] J.-i. Aihara, *J. Phys. Chem. A* **1999**, 103, 7487.

[178] A. L. Arokiyanathan, S. Lakshmipathi, *Theor. Chem. Acc.* **2021**, 140, 36.

[179] A. A. Peterson, F. Abild-Pedersen, F. Studt, J. Rossmeisl, J. K. Nørskov, *Energy Environ. Sci.* **2010**, 3, 1311.

[180] K. P. Kuhl, E. R. Cave, D. N. Abram, T. F. Jaramillo, *Energy Environ. Sci.* **2012**, 5, 7050.

[181] K. Yao, J. Li, H. Wang, R. Lu, X. Yang, M. Luo, N. Wang, Z. Wang, C. Liu, T. Jing, S. Chen, E. Cortés, S. A. Maier, S. Zhang, T. Li, Y. Yu, Y. Liu, X. Kang,

H. Liang, *J. Am. Chem. Soc.* **2022**, 144, 14005.

[182] X. Liu, P. Schlexer, J. Xiao, Y. Ji, L. Wang, R. B. Sandberg, M. Tang, K. S. Brown, H. Peng, S. Ringe, C. Hahn, T. F. Jaramillo, J. K. Nørskov, K. Chan, *Nat. Commun.* **2019**, 10, 32.

[183] J. D. Goodpaster, A. T. Bell, M. Head-Gordon, *J. Phys. Chem. Lett.* **2016**, 7, 1471.

[184] K. Nagita, K. Kamiya, S. Nakanishi, Y. Hamamoto, Y. Morikawa, *ECS Meeting Abstracts* **2024**, MA2024-02, 3726.

[185] E. Pérez-Gallent, G. Marcandalli, M. C. Figueiredo, F. Calle-Vallejo, M. T. M. Koper, *J. Am. Chem. Soc.* **2017**, 139, 16412.

[186] E. Sargeant, P. Rodriguez, F. Calle-Vallejo, *ACS Catal.* **2024**, 14, 8814.

[187] L. Ou, W. Long, Y. Chen, J. Jin, *RSC Adv.* **2015**, 5, 96281.

[188] J. Santatiwongchai, K. Faungnawakij, P. Hirunsit, *ACS Catal.* **2021**, 11, 9688.

[189] T. Luo, K. Liu, J. Fu, S. Chen, H. Li, H. Pan, M. Liu, *Adv. Energy Sustainability Res.* **2023**, 4, 2200148.

[190] G. Shi, T. Lu, L. Zhang, *Natl. Sci. Rev.* **2024**, 11, nwae241.

[191] L. Jiang, C. Zhou, J. Cai, K. Li, H. Wang, *Cell Rep. Phys. Sci.* **2024**, 5, 102246.

[192] Y. Yuan, J. Li, Y. Zhu, Y. Qiao, Z. Kang, Z. Wang, X. Tian, H. Huang, W. Lai, *Angew. Chem. Int. Ed.* **2025**, 64, e202425590.

[193] J. Mähler, I. Persson, *Inorg. Chem.* **2012**, 51, 425.

[194] J.-B. Le, A. Chen, Y. Kuang, J. Cheng, *Natl. Sci. Rev.* **2023**, 10.

[195] C. Wang, Z. Wang, H. Sun, S. Yao, Z. Liu, M. Lv, F. Li, Z. Lv, X. Hu, W.

Zhou, J. Fan, H. Wang, L. Liu, *Appl. Catal. B: Environ.* **2025**, 366, 125006.

[196] Y. Wang, J. Zhang, J. Zhao, Y. Wei, S. Chen, H. Zhao, Y. Su, S. Ding, C. Xiao, *ACS Catal.* **2024**, 14, 3457.

[197] Y. Wei, J. Zhang, B. Li, F. Yu, M. Li, Y. Wang, T. He, J. Zhu, S. Chen, Y. Su, S. Ding, C. Xiao, B. Y. Xia, *Adv. Mater.* **2025**, 2504515.

[198] J. Li, X. Li, C. M. Gunathunge, M. M. Waegele, *Proc. Natl. Acad. Sci. U.S.A.* **2019**, 116, 9220.

[199] S. Yu, H. Yamauchi, S. Wang, A. Aggarwal, J. Kim, K. Gordiz, B. Huang, H. Xu, D. J. Zheng, X. Wang, H. Iriawan, D. Menga, Y. Shao-Horn, *Nat. Catal.* **2024**, 7, 1000.

[200] J. Zhou, B. He, P. Huang, D. Wang, Z. Zhuang, J. Xu, C. Pan, Y. Dong, D. Wang, Y. Wang, H. Huang, J. Zhang, Y. Zhu, *Angew. Chem. Int. Ed.* **2025**, 64, e202418459.

[201] J.-M. McGregor, J. T. Bender, A. S. Petersen, L. Cañada, J. Rossmeisl, J. F. Brennecke, J. Resasco, *Nat. Catal.* **2025**, 8, 79.

[202] H. D. B. Jenkins, M. S. F. Pritchett, *J. Chem. Soc., Faraday Trans.* **1984**, 80, 721.

[203] Y. Marcus, *J. Chem. Soc., Faraday Trans.* **1991**, 87, 2995.

[204] H. Sun, *J. Phys. Chem. B* **1998**, 102, 7338.

[205] X. Li, J. Sun, X. Wei, L. Li, H. Jin, L. Guo, *J. Supercrit. Fluids* **2023**, 202, 106053.

[206] B. Delley, *J. Chem. Phys.* **1990**, 92, 508.

[207] B. Delley, *J. Chem. Phys.* **2000**, 113, 7756.

[208] W. J. Hehre, *Acc. Chem. Res.* **1976**, 9, 399.

[209] S. Grimme, J. Antony, S. Ehrlich, H. Krieg, *J. Chem. Phys.* **2010**, 132, 154104.

[210] F. Zhang, J. D. Gale, B. P. Uberuaga, C. R. Stanek, N. A. Marks, *Phys. Rev. B* **2013**, 88, 054112.

[211] A. Klamt, G. Schüürmann, *J. Chem. Soc., Perkin Trans. 2* **1993**, 799.

[212] C. Caleman, J. S. Hub, P. J. van Maaren, D. van der Spoel, *Proc. Natl. Acad. Sci. U.S.A.* **2011**, 108, 6838.